Multimodal multiscale analysis reveals flexible DNA contacts of bacterial nucleoprotein filaments

Beth A. Shen[1], Christine M. Hustmyer[1], Daniel Roston[1,2], Michael B. Wolfe[1], Erik D. Jessen[1], and Robert Landick[1,3]

[1]Department of Biochemistry, University of Wisconsin–Madison, Madison, WI 53706
[2]Current address: Department of Chemistry and Biochemistry, University of California San Diego, La Jolla, CA 92093
[3]Department of Bacteriology, University of Wisconsin–Madison, Madison, WI 53706

*To whom correspondence should be addressed; Email: rlandick@wisc.edu

Keywords:

bacterial chromatin; H-NS; ChIP-seq; FeBABE; MD simulation; nucleoprotein; gene regulation

Select Abbreviations:

ChIP-seq, chromatin immunoprecipitation followed by high-throughput sequencing; DBD, DNA binding domain; DBP, DNA binding protein; FeBABE, Fe(III) (S)-1-(p-Bromoacetamidobenzyl)ethylenediaminetetraacetate; Fe·EDTA–H-NS, H-NS derivatized with an Fe^{2+}·EDTA nuclease; gDNA, genomic DNA; MD, molecular dynamics; NTD, N-terminal domain; •OH, hydroxyl radical; RNAP, RNA polymerase

ABSTRACT

Gene silencing in bacteria is mediated by chromatin proteins, of which *Escherichia coli* H-NS is a paradigmatic example. H-NS forms nucleoprotein filaments with either one or two DNA duplexes. However, the overall structures, arrangements of DNA-binding domains (DBDs), positions of DBD–DNA contacts, and determinants of genomic distribution for these linear and bridged filaments are uncertain. To connect H-NS structures that silence genes *in vivo* with features elucidated *in vitro*, we developed a multimodal, multiscale analysis that combines a new method for chromatin reconstitution and mapping (Nitro-seq), ChIP-seq, tethered-nuclease mapping of DBD–DNA contacts (TEN-map), ·OH footprinting, molecular dynamics, and bioinformatics. We find that DNA sequence principally governs H-NS-filament location with indistinguishable sequence specificity in bridged or linear forms with or without the H-NS modifiers StpA and Hha, and that DBD–DNA contacts vary in orientation and position with ~10-bp average spacing. Our results support a hemi-sequestration model of linear-to-bridged filament switching.

15 **INTRODUCTION**

16 Extensive study of nucleosome-based chromatin structure has provided broad insight into
17 mechanisms of chromatin-mediated gene regulation in eukaryotes (Cook and Marenduzzo, 2018;
18 Luger et al., 1997; Talbert et al., 2019). For bacteria, however, an analogous structural
19 understanding remains elusive in part due to the diverse and complex DNA-binding properties of
20 the multiple DNA-binding proteins (DBPs) that generate bacterial chromatin (Dame et al., 2020;
21 Grainger, 2016; Shen and Landick, 2019). The γ-proteobacterial histone-like nucleoid structuring
22 protein (H-NS; 15 kDa monomer) provides a representative example of this complexity. H-NS,
23 which contains two oligomerization sites in its N-terminal domain (NTD) and a C-terminal DNA
24 binding domain (DBD), forms gene-silencing, oligomeric filaments on AT-rich DNA, notably on
25 pathogenicity operons (e.g. SPI-1 in *Salmonella*), surface-antigen operons (e.g. LPS biosynthesis
26 in *Escherichia coli*, and horizontally acquired genes (e.g. *bgl* operon in *E. coli*) (Gawade et al.,
27 2020; Grainger et al., 2006; Kahramanoglou et al., 2011; Lucchini et al., 2006; Navarre et al.,
28 2006; Sankar et al., 2009).

29 H-NS oligomerizes on DNA through head–head and tail–tail NTD contacts into filaments
30 that adopt either linear or bridged conformations in which H-NS interacts with one or two
31 segments of duplex DNA, respectively (Arold et al., 2010; Gordon et al., 2011; Kotlajich et al.,
32 2015; Liu et al., 2010; Ulissi et al., 2014) (***Figure 1A***). The DBD forms an AT-hook that binds
33 the narrow minor groove of AT-rich DNA (Gordon et al., 2011). A flexible linker connecting the
34 DBD and NTD enables DBD–DNA contacts. However, in some conditions, a subset of DBDs
35 are proposed to interact with the NTD rather than DNA yielding a hemi-sequestered, linear
36 conformation of H-NS–DNA filaments (Gao et al., 2017; Gulvady et al., 2018; van der Valk et
37 al., 2017) (***Figure 1A***). Both linear and bridged filaments inhibit transcription initiation by RNA
38 polymerase (RNAP) by occluding promoters but only bridged filaments inhibit transcript
39 elongation by RNAP, which occurs via a topological trapping mechanism (Boudreau et al., 2018;
40 Kotlajich et al., 2015; Lim et al., 2012) (***Figure S1–1A***).

41 The extent to which DNA sequence alone *versus* competition from transcription and
42 other DBPs controls the locations of the ~0.2-20 kb H-NS filaments that cover ~15% of the *E.*

43 *coli* K-12 genome is unclear (Kahramanoglou et al., 2011; Noom et al., 2007). Various DNA
44 sequences, including a 10-bp high-affinity motif (TCGATAAATT), A-tracts, AT-content, and
45 TA dinucleotide steps, have been proposed to define H-NS binding sites (Bouffartigues et al.,
46 2007; Gordon et al., 2011; Gulvady et al., 2018; Japaridze et al., 2017; Lang et al., 2007; Owen-
47 Hughes et al., 1992; Riccardi et al., 2019; Yamada et al., 1991). However, both active
48 transcription and other DBPs are known to affect H-NS binding patterns. Although H-NS
49 can inhibit RNAP (Dole et al., 2004; Kotlajich et al., 2015; Lim et al., 2012; Singh et al., 2014),
50 RNAP also can displace H-NS at some loci (Chandraprakash and Seshasayee, 2014; Rangarajan
51 and Schnetz, 2018). Additionally, DBPs can regulate gene expression either by promoting
52 or displacing H-NS binding, for instance in anti-silencing mechanisms (Will et al., 2015).

53 The properties of H-NS nucleoprotein filaments also are modulated by the H-NS paralog,
54 StpA, by small Hha/YmoA-family regulators (e.g. Hha), by Mg^{2+}, and by solutes (Dame et al.,
55 2020). StpA forms heterodimers with H-NS whereas Hha binds to the NTD of H-NS, but not to
56 DNA (Ali et al., 2013; Leonard et al., 2009). Both StpA and Hha stimulate bridging by H-NS
57 (Boudreau et al., 2018; van der Valk et al., 2017; Wang et al., 2014); both also enhance silencing
58 at subsets of H-NS regulated genes, but the extent of overlap between these subsets is unknown
59 (Banos et al., 2009; Lucchini et al., 2009; Muller et al., 2006; Nieto et al., 2000; Srinivasan et al.,
60 2013; Uyar et al., 2009). However, ChIP-seq results suggest that H-NS, StpA, and Hha bind to
61 the same locations in the genome (Srinivasan et al., 2013; Ueda et al., 2013; Uyar et al., 2009);
62 thus, their apparently differential effects on gene regulation remain to be explained.

63 It also is unclear how DBDs are arranged within H-NS filaments and if they change
64 arrangement in the switch from linear to bridged conformations. DNase and ·OH footprinting
65 experiments reveal nucleation at high-affinity sites and H-NS oligomerization with an apparent
66 periodicity of DBD contacts every ~10 bp (Bouffartigues et al., 2007; Ulissi et al., 2014; Will et
67 al., 2015). However, ~20- and ~30-bp periodicities of DBD footprints also are reported. A
68 prevalent model for H-NS filament organization based on an NTD crystal structure suggests
69 ~30-bp spacing of DBDs (Arold et al., 2010; Dame et al., 2006). Given the flexible linker
70 connecting the DBD, a key question is whether DBDs necessarily exhibit a regular arrangement

71 of contacts to DNA within H-NS filaments. New approaches are needed to determine how DNA
72 sequence governs DBD location and the arrangement of DBDs in an H-NS filament.

73 To gain insight into the determinants of H-NS filament formation and DBD locations in
74 filaments, we developed and applied a multimodal, multiscale approach that combines a new
75 method to reconstitute and map bacterial chromatin using HT-sequencing (Nitro-seq), a novel
76 DBD-mapping method using a tethered chemical nuclease (TEN-map), hydroxyl radical (·OH)
77 footprinting, ChIP-seq, computational molecular dynamic (MD) simulations, and rigorous
78 statistical analysis and modeling. Our results reveal that DNA sequence, rather than transcription
79 or other DBPs, principally guide the pattern of gene silencing *in vivo* and that DBDs contact
80 DNA irregularly in an H-NS filament in patterns unaffected by bridging *versus* linear
81 conformations.

82 **RESULTS**

83 **H-NS filament locations are not principally determined by transcription**

84 Although actively elongating RNAP can rearrange H-NS filaments near transcription–H-NS
85 junctions (Rangarajan and Schnetz, 2018) and can more extensively alter H-NS binding genome-
86 wide when ρ-dependent termination is inhibited (Chandraprakash and Seshasayee, 2014), the
87 extent to which transcription governs H-NS filament formation across the genome is unclear. To
88 address this question, we first used ChIP-seq to determine RNAP and H-NS locations in the
89 presence or absence of the transcription inhibitor rifampicin (Rif). Rif prevents extension of
90 initial RNA transcripts past 3 nt, causing RNAP to relocate *in vivo* to promoters or promoter-like
91 sequences (Campbell et al., 2001; Herring et al., 2005). We hypothesized that if transcribing
92 RNAPs strongly contribute to H-NS filament patterns in cells, then trapping all RNAP at
93 promoters with Rif would alter H-NS locations detected by ChIP-seq (***Figure 1B***). We treated
94 wild-type *E. coli* K-12 cells with Rif and then generated ChIP-seq samples from treated and
95 untreated cells using antibodies specific for RNAP or H-NS. Comparison of the RNAP ChIP
96 patterns in the presence or absence of Rif revealed the expected Rif-induced redistribution of
97 RNAP to promoters or cryptic promoters throughout the genome (***Figure 1C***; ***Figure S1–1***)
98 (Herring et al., 2005; Kim et al., 2012; Thomason et al., 2015). The majority (72%) of
99 identifiable RNAP peaks in Rif-treated cells were within 30 bp of a known promoter based on a
100 genome-scale, transcription-start-site (TSS) analysis (Thomason et al., 2015), with a mean
101 distance of ~10 bp vs. ~140 bp for a randomized control ($p < 10^{-4}$; ***Figure S1–2***). In contrast, the
102 H-NS binding pattern exhibited only minimal changes upon Rif treatment despite the elimination
103 of elongating RNAPs.

104 To characterize the small number of filaments that did change, we used MOSAiCS to assess
105 the extent of change in filaments present at the same genomic location in untreated and Rif-
106 treated cells (Kuan et al., 2011). MOSAiCS is well-suited to map transcribed regions and H-NS
107 filaments because it can identify broad regions of enrichment relative to the input DNA prior to
108 immunoprecipitation in addition to the symmetrical Gaussian-like peaks typical for single-site
109 DNA-binding proteins. To analyze changes in H-NS filaments upon Rif treatment, we defined

110 four classes of filaments: (1) unchanged by Rif treatment; (2) filaments with boundaries that
111 expanded (2a) or receded (2b) by more than 200 bp (~10% of the ~2 kb average filament length);
112 (3) filaments that appeared only after Rif treatment; and (4) filaments that dissociated upon Rif
113 treatment. Most filaments were unchanged; class 1 included ~85% of all filaments present in
114 untreated cells (266 of 301 filaments) (***Figure 1D***). Even when transcription was directly
115 adjacent to an H-NS filament, such as *cysHIJ* adjacent to the H-NS-bound *cas* operon, H-NS
116 filaments were not dramatically altered upon Rif treatment (***Figure 1C***). Class 1 unchanged
117 filaments included H-NS silenced genes with internal antisense transcription units, such as the β-
118 glucoside utilization (*bgl*) operon (***Figure S1–3***) (Dole et al., 2004). However, Rif treatment did
119 affect the lengths or existence of ~14% of the H-NS filaments (***Figure 1D***), causing changes at
120 one or both ends of some filaments (class 2; *n*=30), appearance of a few filaments (class 3; *n*=3),
121 and disappearance of other filaments (class 4; *n*=12) (Table S5).

122 We next investigated whether changes in RNAP binding to promoter or promoter-like
123 sequences explained the minimal changes in H-NS filaments upon Rif treatment. We
124 hypothesized that Rif-induced relocation of RNAP to promoters could either disrupt an existing
125 H-NS filament at sites of relocation or allow H-NS binding in previously transcribed regions.
126 Most (75%) of the few filaments that disappeared in Rif-treated cells (class 4; n=12) overlapped
127 a Rif-induced RNAP-binding site (e.g. at the H-NS-regulated *dps* promoter; ***Figure 1D***)
128 (Grainger et al., 2008) and two of the three Rif-induced filaments overlapped a location vacated
129 by RNAP (Table S5). In nearly all cases (89%), the locations at which filaments receded (class
130 2b; n=18) corresponded to locations of Rif-induced RNAP binding (Table S5). Conversely, 55%
131 of sites at which filaments grew (class 2a; n =12) were associated Rif-induced loss of bound
132 RNAP. Together, our results indicate that active transcription elongation plays a minimal role in
133 determining locations of H-NS binding in *E. coli*, although the few sites at which transcription
134 does affect H-NS binding could play important roles in gene regulation.

135 **H-NS nucleoprotein filaments can be reconstituted using genomic DNA *in vitro***

136 Even though active transcription does not principally determine H-NS filament locations, it
137 remained possible that other DBPs could play dominant roles in guiding H-NS filament

138 formation *in vivo*, either by exclusion or via cooperative interactions. To test this possibility, we
139 sought to reconstitute H-NS filaments *in vitro* using purified proteins and chromosomal DNA to
140 compare to the H-NS binding locations *in vivo*. A similar approach to eukaryotic chromatin
141 reconstitution has been achieved recently and has proven informative (Krietenstein et al., 2016).
142 We predicted that any strong effects of DBPs on H-NS filament locations *in vivo* would be
143 evident as differences between the *in vitro* reconstituted filaments and *in vivo* ChIP-seq profiles.
144 To study H-NS filament *in vitro*, we reconstituted them on fragmented and purified genomic
145 DNA (gDNA), captured the reconstituted filaments by binding to nitrocellulose filters, and then
146 mapped filament locations by HT-sequencing of DNA recovered from the filters (***Figure 2A***;
147 ***Figure S2-1,2***; see Methods). We call this method Nitro-seq.

148 To verify that Nitro-seq captures specific protein-DNA interactions, we compared retention
149 on filters of purified and protein-free gDNA to retention of H-NS-bound gDNA. The purified
150 gDNA gave a uniform distribution of sequence reads prior to nitrocellulose filter-binding and
151 much lower amounts of retained DNA compared to H-NS-bound samples (~1.5% of gDNA
152 retained without H-NS; ***Figure S2–3***). Reconstitution with H-NS caused nitrocellulose retention
153 of 4-12% of the gDNA (***Figure S2–1B***), with reproducible and distinct patterns of enrichment
154 (peaks) across the genome (***Figure 2B***; ***Figure S2–4***). This fraction of gDNA filter-retention by
155 H-NS was similar to the ~15% of the *E. coli* K-12 genome bound by H-NS *in vivo* (Grainger et
156 al., 2006), suggesting that our Nitro-seq method captured specific H-NS binding events.
157 MOSAiCS analysis identified 407 H-NS binding regions (~1.4 kb on average) in the Nitro-seq
158 results (***Table 1***).

159 Importantly, the Nitro-seq H-NS-binding pattern differed from the DNA-binding pattern
160 generated by another abundant, AT-preferring DBP in *E. coli*, Fis, in a control Nitro-seq
161 experiment. Fis also bound AT-rich DNA but exhibited a different pattern than H-NS consistent
162 with its distribution on chromosomal DNA *in vivo* (Cho et al., 2008; Kahramanoglou et al.,
163 2011); ***Figure S2–4***; ***Figure S3–1A***). We quantified the difference in the H-NS and Fis Nitro-seq
164 patterns by calculating the Jaccard index (0.2 for H-NS versus Fis; the Jaccard index measures
165 overlap of enriched regions and scales from 0–1 no overlap–complete overlap; see Methods).

166 These results verify that Nitro-seq identifies specific patterns of protein-DNA interactions and is
167 suitable for tracking *in vitro* reconstitution of bacterial chromatin.

168 **The *in vivo* pattern of H-NS filaments is primarily determined by DNA sequence**

169 To determine whether DNA sequence-specific binding by H-NS primarily explains the
170 distribution of H-NS *in vivo*, we compared the binding pattern of H-NS in our *in vitro* Nitro-seq
171 assay to *in vivo* ChIP-seq results (***Figure 3A***). Overall, the *in vivo* (ChiP-seq) and *in vitro* (Nitro-
172 seq) H-NS binding patterns were highly similar (Jaccard index = 0.6; ***Figure 2B***, ***Figure 3B***).
173 However, the Nitro-seq sites fell into two classes: (1) sites that overlapped with ChIP-seq sites
174 and were similar in length (n = 297; Jaccard index = 0.71, covering 89% of the bp bound by H-
175 NS *in vivo*) and (2) sites observed only by Nitro-seq and were on average shorter than the *in vivo*
176 H-NS filaments (n = 112, or 35% of the bp bound by H-NS *in vitro*; ***Figure 3B***, ***Figure S3–2A-***
177 ***C***). Among class-1 overlapping filaments, most (255) overlapped for ≥90% of bp *in vivo* and *in*
178 *vitro* (***Figure 3B***, black dots). For example, the *in vivo* and *in vitro* H-NS binding patterns at the
179 *bgl* operon were nearly identical (***Figure S3–2B***). We conclude that H-NS binds DNA in similar
180 patterns *in vitro* and *in vivo*, with some additional sites available *in vitro*.

181 We hypothesized that many of the Nitro-seq-specific filaments could be explained by
182 competition for H-NS binding *in vivo* by other DBPs. To test this idea, we compared the Nitro-
183 seq-specific regions to known transcription factor (TF) binding sites from RegulonDB (Santos-
184 Zavaleta et al., 2019) and to protein-occupied regions of the genome called extended protein
185 occupancy domains or EPODs (Vora et al., 2009) (***Figure S3–2***; ePODS can be either silenced
186 regions called *ts*EPODS or highly expressed regions called *he*EPODS). If Nitro-seq-specific
187 regions are explained by binding to unmasked sites normally protected by other DBPs *in vivo*,
188 then they should correlate with the TF-binding sites. Alternatively if these regions are explained
189 by exclusion of H-NS by active transcription *in vivo* (i.e., they are normally bound by RNAP),
190 then they should correlate with *he*EPODS (regions of high RNAP occupancy *in vivo*). We found
191 that the Nitro-seq-specific filaments were enriched in RegulonDB TF-binding sites with 62 of
192 112 (55%) overlapping known TF-binding sites (***Figure S3–2D***). Given that TF-binding sites are
193 incompletely mapped, the observation of 55% overlap is consistent with a majority of the class-

194 2, Nitro-seq-specific filaments being explained by TF exclusion of H-NS *in vivo*. TFs known to
195 compete with H-NS, such as IHF, FNR, and Fis, bind about 29 of the class-2 sites (***Figure S3–***
196 ***2A*****;** Table S6), further supporting this explanation (Stoebel et al., 2008; Will et al., 2015). In
197 contrast, Nitro-seq-specific filaments did not overlap significantly with *he*EPODS, also
198 consistent with exclusion of H-NS *in vivo* by DBPs and not by transcription. As expected, class-
199 1 filaments were highly similar to tsEPODs ($p<0.001$). Consistent with our H-NS ChIP results
200 (***Figure 1***), we conclude that the Nitro-seq-specific regions reflect sites at which H-NS is
201 excluded by other DBPs *in vivo* and that active transcription minimally affects H-NS filament
202 locations. Together, our results indicate that most H-NS filament locations in *E. coli* cells are
203 determined by DNA sequence alone with a minority of potential locations blocked by other
204 DBPs *in vivo*, notably by anti-silencing TFs (Will et al., 2015).

205 **H-NS and StpA exhibit indistinguishable DNA binding specificities**

206 Both the H-NS paralog StpA and the H-NS modulator Hha promote bridging by H-NS filaments
207 and help silence subsets of H-NS-silenced genes with unknown overlap (Boudreau et al., 2018;
208 Srinivasan et al., 2013; Uyar et al., 2009; van der Valk et al., 2017). Their effects on DNA-
209 sequence specificity are unknown but ChIP patterns largely indistinguishable from H-NS are
210 reported for both, leaving their roles in silencing unexplained (Banos et al., 2009; Fukui et al.,
211 2016; Nieto et al., 2000; Uyar et al., 2009). To determine whether StpA and Hha-bound H-NS
212 filaments differ in sequence specificity from H-NS-only filaments, we applied the Nitro-seq
213 assay to StpA and Hha–H-NS filaments. Using optimized binding conditions and MOSAiCS
214 analysis (see Methods), we found that H-NS, StpA, and Hha–H-NS produced virtually
215 indistinguishable binding patterns on gDNA (***Figure 2B*****;** ***Figure S2–4*****;** ***Figure 3*****;** ***Figure S3–***
216 ***1A*****;** ***Table 1***). For StpA vs. H-NS, the average densities of Nitro-seq reads were highly correlated
217 (Spearman $\rho = 0.984$) and the MOSAiCS-predicted filaments overlapped extensively (Jaccard
218 index = 0.73). StpA generated more filaments than H-NS (589 vs 407), possibly due to tighter
219 binding by StpA (Sonnenfield et al., 2001); removing the StpA-only filaments increased the
220 overlap to a Jaccard index of 0.86 (***Figure 3C***). We observed a similarly high degree of overlap
221 between the H-NS and Hha–H-NS datasets (Spearman ρ of average read densities = 0.993;

222 Jaccard index of MOSAiCS-predicted filaments = 0.86; ***Figure 3D; Figure S3–1A***). We
223 conclude that StpA, Hha–H-NS and H-NS exhibit essentially indistinguishable sequence
224 specificities in our *in vitro* conditions (see Discussion).

225 **Tethered-nuclease mapping (TEN-map) reveals H-NS DBD locations in H-NS filaments**
226 Having established that *in vitro* reconstituted H-NS filaments recapitulate their key ability to
227 target subsets of genes *in vivo*, we next sought to determine the spacing, orientations, and
228 regularity of H-NS DBDs in a representative filament able to form both bridged and linear
229 configurations. To move from the genome-wide to the bp scale, we thus chose the well-
230 characterized *bgl* operon downstream regulatory element (DRE). H-NS filaments formed on the
231 DRE are known to: (1) be determined by DNA sequence (***Figure S1–3***; ***Figure S3–2***);
232 (2) switch from bridged to linear *in vitro* when H-NS is present above ~200 monomers/kb DNA;
233 (3) be modulated by Mg^{2+}; and (4) silence the *bgl* operon by inhibiting both transcript elongation
234 by RNAP and, via bridging to an upstream regulatory element (URE), binding of RNAP to the
235 *bgl* promoter (Boudreau et al., 2018; Kotlajich et al., 2015; Nagarajavel et al., 2007; Schnetz,
236 1995) (***Figure S4–1A***).

237 To enable precise assignment of DBD locations in the DRE filament, we developed a
238 tethered nuclease mapping (TEN-map) assay in which an artificial chemical nuclease
239 (Fe^{2+}·EDTA) is covalently tethered near but not within the DBD–DNA interface by reaction of
240 FeBABE (Fe(III) (*S*)-1-(*p*-Bromoacetamidobenzyl)ethylenediaminetetraacetate) with Cys
241 substituted for Glu-102 (***Figure 4A-B***). Upon activation, the tethered Fe^{2+}·EDTA generates
242 hydroxyl radicals (·OH) that cleave the DNA backbone within ~12 Å of the chelated Fe^{2+} (Cheal
243 et al., 2009). The resulting DNA cleavage pattern thus defines the location and orientation of the
244 H-NS DBD within the nucleoprotein filament. This tethered cleavage pattern differs from a
245 conventional ·OH footprinting pattern generated by Fe^{2+}·EDTA free in solution, which
246 principally defines just solute exclusion from the DNA surface by the bound DBD.

247 To validate use of the derivatized H-NS for TEN-map, we compared it to similarly treated
248 C21S H-NS lacking the tethered nuclease and to wild-type H-NS in DNA-binding and
249 transcription experiments. Both conjugated and control H-NS bound *bgl* DRE DNA similarly to

250 wild-type H-NS in a gel-shift assay (***Figure S4–2***). The somewhat higher concentration
251 requirements may reflect a known propensity of H-NS to lose activity during biochemical
252 manipulation (R.T. Dame, personal communication, July 2020). Of note, high concentrations of
253 conjugated H-NS did not generate the increased mobility complex thought to reflect linear
254 filament formation (Kotlajich et al., 2015). Conjugated H-NS slowed transcript elongation and
255 stimulated backtrack pausing by RNAP on a *bgl* DRE template as expected for bridged H-NS
256 filaments. However, at ≥200 monomer/kb both conjugated H-NS and control C21S H-NS treated
257 with FeBABE (i.e., treated but unconjugated H-NS) continued to inhibit RNAP elongation
258 indicative of constitutive H-NS bridging (***Figure S4–3D***), whereas at ≥200 monomer/kb wild-
259 type H-NS and untreated C21S or C21S–E102C H-NS allow faster RNAP elongation indicative
260 of switching to linear H-NS filaments (***Figure S4–3A-C***) (Boudreau et al., 2018; Kotlajich et al.,
261 2015). This observation suggests that the conjugated H-NS may be unable to form linear
262 filaments, either due to partial inactivation by FeBABE treatment making it impossible to reach
263 ≥200 active monomer/kb or due to constitutive bridging by conjugated H-NS as observed for
264 StpA (Boudreau et al., 2018; see Discussion). We concluded that conjugated H-NS was suitable
265 for TEN-map analysis of DBD positions in bridged but not linear *bgl* DRE filaments.

266 To probe the locations of H-NS DBDs on DNA by TEN-map, we used a 146-bp *bgl* DRE
267 fragment that could accommodate 10–15 H-NS monomers (assuming an H-NS binding site size
268 of 10–15 bp; (Amit et al., 2003; Ulissi et al., 2014). The 146-bp fragment enabled single-nt
269 resolution by denaturing PAGE of multiple DBDs on either the template (T) or non-template
270 (NT) strand, depending on the location of a ^{32}P-end-label (***Figure 4C, Figure S4–1B***). After
271 formation of filaments, phosphodiester backbone cleavage *via* hydrogen abstraction from DNA
272 sugars was triggered by addition of H_2O_2 and ascorbic acid to generate ·OH by the Fenton
273 reaction (Balasubramanian et al., 1998). We observed robust cleavage patterns on both the T and
274 NT strands indicated DBD locations on the *bgl* DRE fragment (***Figure 4D, Figure S4–4A***).
275 Cleavage was dependent on the presence of ascorbic acid, H_2O_2, and Fe·EDTA tethered to H-
276 NS, indicating that it resulted from H-NS binding and not from ·OH formed by untethered
277 Fe·EDTA (***Figure 4D***, top panel).

278 Peaks of cleavage were spaced irregularly at intervals of 6–21 nt on the T strand and 9–14 nt
279 on the NT strand (***Figure 4E and F***; NT, red arrows; T, blue arrows) and remained unchanged in
280 location up to 5 μM Fe·EDTA–H-NS. We quantified the H-NS concentration-dependence of
281 cleavage using linear approximations of the change in normalized peak areas (***Figure S4–4 and***
282 ***5***). Large, positive slopes indicating robust H-NS-dependent cleavage were spaced ~10–15 bp.
283 This spacing is consistent with previous H-NS footprint analyses using untethered probes on
284 different DNA fragments in which regions of protected DNA occurred with 10–20 bp periodicity
285 (Bouffartigues et al., 2007; Dame et al., 2006; Ulissi et al., 2014; Will et al., 2018).

286 To verify that TEN-map patterns reflected tethered nuclease cleavage, we compared them to
287 untethered ·OH cleavage of DNA alone or of DNA bound to wild-type H-NS (***Figure S4–6***). As
288 expected if conjugated and unconjugated H-NS DBDs protect the same sites, the TEN-map
289 patterns had features in common with untethered ·OH H-NS footprints, reflecting DNA
290 protected by bound DBD, but were clearly different, reflecting localized TEN-map cleavages.
291 Both tethered and untethered ·OH cleavage were also easily distinguishable from background
292 ·OH cleavage of DNA alone. These results confirmed that TEN-map yields valuable information
293 that can be used to locate DNA contacts of the H-NS DBDs and that ·OH footprints provide an
294 independent source of information to map DBD–DNA contacts.

295 To test whether H-NS binding patterns are affected by flanking sequence or DNA end
296 positions, we first compared cleavage of the 146-bp *bgl*-DRE fragment to that of a 151-bp
297 fragment with identical internal sequence and 5 bp added to the downstream end (***Figure S4–***
298 ***7A***). The identical cleavage patterns of these fragments established that the DBD locations
299 reported by TEN-map depended on the underlying sequence rather than being phased from a
300 nearby DNA end (***Figure S4–7B***), as expected from prior results (Bouffartigues et al., 2007). To
301 test whether the patterns seen on a short *bgl*-DRE change in longer filaments, we compared
302 results on the 146-bp fragment to TEN-map analysis of a 549-bp *bgl* DRE-containing fragment
303 that was extended toward P_{bgl} but retained the same downstream ^{32}P-labeled end (***Figure S4–***
304 ***7C***). The tethered-cleavage patterns were nearly identical for both DNA fragments (***Figure S4–***
305 ***7D***), except for a new peak at position ~645 on the longer fragment that likely resulted from

306 stabilization of the upstream H-NS filament. We conclude TEN-map reports DBD locations
307 based only on the underlying DNA sequence and that these locations on the *bgl* DRE are spaced
308 irregularly at intervals of roughly 5–20 bp.

309 **H-NS DBD locations are unchanged in obligately bridged filaments or by Mg^{2+}**

310 We next sought to confirm that TEN-map reported H-NS DBD locations in bridged filaments by
311 forming obligately bridged filaments using a previously developed bridging pull-down assay
312 (van der Valk et al., 2017) (***Figure 5A; Figure S5–1A***). In this assay, H-NS–DNA filaments are
313 captured from solution by DNA-coated magnetic beads. Capture requires H-NS bridging
314 between the bead-bound and unbound DNAs. We incubated streptavidin beads pre-loaded with a
315 685-bp, biotinated bait DNA with a mixture of Fe·EDTA-H-NS, unmodified H-NS, and the 549-
316 bp *bgl* DRE-containing fragment (***Figure 5A***; the *bgl* DRE fragment lacked biotin and was 5′-
317 ^{32}P-end-labeled on the T strand). Bridged filaments, whose formation was unaffected by the
318 presence of conjugated H-NS, were magnetically separated from unattached filaments and TEN-
319 map cleavage was activated. These obligately bridged cleavage patterns were indistinguishable
320 from those observed without bead-based capture (compare ***Figure S4–7D*** to ***Figure 5A; Figure***
321 ***S5–2***), confirming that the TEN-map assay reports the locations of bridged H-NS DBDs. As an
322 additional test, we asked how elevated Mg^{2+}, which stimulates bridging at concentrations >5 mM
323 (Liu et al., 2010), would affect the TEN-map assigned DBD locations. We found that DBD
324 locations were unaffected by elevated Mg^{2+} (8 mM vs. ~0.3 μM) (***Figure 5B, Figure S5–3***). Our
325 results are consistent with constitutive bridging by conjugated H-NS in the TEN-map assay and
326 also are consistent with a previous conclusion that changing Mg^{2+} concentration does not alter
327 DBD locations (Will et al., 2018).

328 **DBD ·OH footprints on DNA are unchanged during bridged-to-linear switching**

329 Although TEN-map reveals the location of DBDs in bridged filaments, we wanted to compare
330 these locations on bridged and linear filaments. To enable this comparison, we examined
331 untethered ·OH footprints of wild-type H-NS on the *bgl* DRE encompassing previously validated
332 bridged-to-linear switching by increasing H-NS/DNA ratios (Kotlajich et al., 2015) (***Figure 6A***).
333 We normalized ·OH cleavage as a function of H-NS concentration to the unprotected cleavage

334 pattern to correct for intrinsic DNA reactivity (Burkhoff and Tullis, 1988) (***Figure 6B–D, Figure***
335 ***S6–1***). Strikingly, the H-NS footprint patterns did not change as H-NS concentration was
336 increased from a range that favors bridging to well above the concentration known to switch
337 filaments to the linear conformation. This unchanging ·OH footprint pattern indicates that H-NS
338 DBD locations on DNA are the same in bridged and linear filaments. The unchanging pattern of
339 H-NS also enabled us to analyze protection of DNA from ·OH as a function of H-NS
340 concentration by calculating linear slopes and thus assign a magnitude of protection to each
341 position in the *bgl* DRE (***Figure S6–1D,F***; ***Figure S6–2***). This analysis revealed that sites of
342 maximal DBD protection were irregularly spaced at intervals of 5–24 nt in both bridged and
343 linear filaments, similar to the spacing observed in bridged filaments by TEN-map (see bars at
344 the bottoms of graphs, ***Figure 6C-D***). These results can be explained if H-NS DBDs occupy the
345 same irregularly spaced locations on DNA in bridged and linear H-NS nucleoprotein filaments.

346 **MD simulation of TEN-map and independent footprint cleavage patterns allows DBD**
347 **positioning**

348 To determine locations and orientations of the H-NS DBD on the *bgl* DRE in molecular terms,
349 we needed a way to predict the expected TEN-map and footprint cleavage patterns for a given
350 DBD location and orientation. To generate these predictions, we used molecular dynamics (MD)
351 simulations. For TEN-map analysis, we first predicted the position of the conjugated Fe·EDTA
352 — and thus the position of the catalytic Fe^{2+}— with respect to DNA and calculated solvent
353 accessible areas (***Figure 7***). The simulations generated a probability distribution of distances
354 between the Fe^{2+} and each nt in the two duplex DNA strands to which H-NS is bound (the two
355 strands were arbitrarily designated A and B for modeling). We assumed that the cleavage
356 propensity at each nt is directly proportional to the local concentration of ·OH at that nt, which
357 we estimated by a diffusion model for ·OH centered at the Fe^{2+} (Cheal et al., 2009). Because
358 some nucleotides are shielded from the solvent by the bound DBD, we scaled the concentration
359 of radicals according to the solvent-accessible surface area of the putative cleavage site (***Figure***
360 ***S7–2***) (Balasubramanian et al., 1998). Modeling based on these assumptions yielded an estimate
361 of the relative cleavage propensity at each nt in the duplex DNA bound by the DBD (***Figure 7A***).

362 When displayed on B-form DNA, foci of cleavage were evident on each DNA strand offset from
363 the location of the DBD in the minor groove (***Figure 7B***). The maximum peak of cleavage was
364 predicted to occur at nt +10 of strand A and was flanked by two smaller predicted cleavage peaks
365 in strand B. Adjacent to these sites of high predicted cleavage were sites of particularly low
366 predicted cleavage, which resulted from shielding by the bound DBD.

367 To identify specific DBD positions in the *bgl*-DRE filament, we developed a statistical
368 method to compare the experimentally measured TEN-map pattern (***Figure S4–5A***) to the MD-
369 predicted cleavage pattern for each possible DBD position and orientation (***Figure 7B***). For each
370 comparison, the Manhattan distance between the simulated pattern and the experimentally-
371 determined cleavage pattern was calculated; the Manhattan distance is the sum of absolute
372 differences in all dimensions between of sets of points with a lower score indicating a closer
373 match (see Methods). This analysis predicted seven unique binding sites with match scores lower
374 than 95% of all match scores from 1000 different sets of shuffled data, which we interpreted to
375 be statistically significant (***Figure 7C***). Given the noise in both the predictions and experimental
376 data, we interpreted predicted binding sites separated by ≤3 bp as one binding site (e.g. n663F
377 and n664R were assigned as one binding site; n indicates assignment is from tethered nuclease
378 data; F or R indicate forward or reverse orientation of the DBD relative to the coding direction of
379 the *bgl* operon; ***Figure 7B***). To visualize this arrangement of DBDs, we placed the center of the
380 DBD (black triangle in ***Figure 7B***) on B-form DNA at the locations with a statistically
381 significant match score in the appropriate orientation (***Figure S7–1***). This model of the H-NS
382 DBDs confirmed that occupation of these seven binding sites on one duplex DNA is sterically
383 feasible. Overall, our TEN-map analysis, which applies to bridged H-NS filaments, predicted
384 four DBDs bound in the forward orientation (n642F, n676F, n695F, and n711F), two bound in
385 the reverse orientation (n685R and n706R), and one (n663F/n664R) bound either in alternating
386 orientations or in an indeterminate orientation. An alternating orientation could result from the
387 DBD changing orientation dynamically or being bound in opposite orientations on different
388 DNA molecules; noise in our experimental data and MD predictions precludes definitive
389 assignment of the n663F/n664R DBD.

390 As an independent way to predict DBD locations for both linear and bridged filaments, we
391 applied a statistical method similar to that used for TEN-map to the untethered ·OH footprints of
392 wild-type H-NS on the *bgl* DRE using calculated Manhattan distances for solvent accessibility-
393 based predictions (***Figure S6–2***; ***Figure S7–2A-B***; see Methods). Because the solvent
394 accessibility pattern was asymmetrical, we matched the footprint data to predictions for both
395 DBD orientations. This analysis predicted four unique binding sites, which we modeled onto B-
396 form DNA (***Figure S7–2C***). Two footprint-predicted DBDs were in the forward orientation
397 (p694F and p711F) and two were either bound in alternating orientations or bound in
398 indeterminate orientation (p665F/p668R and p685F/p688R).

399 The footprint-based and TEN-map predictions of DBD positions on the *bgl* DRE coincided,
400 which allowed us to assign seven unique DBD binding sites with high confidence (***Figure 7D***).
401 Three features of this DBD arrangement stood out. First, we observed variation in the intervals
402 between the location of DBDs on DNA (5–20 bp). Second, both forward and reverse DBD
403 orientations were observed. Third, some DBDs (e.g. at 663-669) exhibited either indeterminate
404 or alternating orientations. Together, these results reveal that DBDs in both bridged and linear H-
405 NS filaments do not contact DNA with rigidly fixed spacing and orientation but rather assume
406 positions and orientations within a window of possible locations based on the highest affinity to
407 local DNA sequence features (see Discussion).

408 **H-NS DBD positioning is associated with sequence-determined DNA structure**

409 Having established from independent ·OH footprint and TEN-map analyses that DBD location
410 and orientation appears to be set by features of DNA sequence within both bridged and linear
411 filaments and that DNA sequence is the principal determinant of the genome-scale distribution of
412 H-NS, we next sought to identify sequence-based parameters that best explain the H-NS
413 distribution genome-wide (i.e., we sought to use bp-scale information to predict genome-scale H-
414 NS locations). Previous work suggests that H-NS DBDs exhibit variable preference for AT-rich
415 4mer sequences (AAAA, AAAT, AATT, ATTT, TTTT, ATAA, ATAT, ATTA, AATA, TAAA,
416 TAAT, TATA, TATT, TTAA, TTAT, or TTTA) with TA-step-containing 4mers being most
417 favored, as well as having increased affinity when the 4mers are located in regions of high A/T

418 content (Gordon et al., 2011). These sequence motifs (meaning a sequence pattern, not a position
419 weight matrix, PWM) were postulated to favor DBD binding because they form a narrow minor
420 groove width (MGW), which H-NS has been shown to bind (Gordon et al., 2011). In addition to
421 sequence motifs per se, it also is possible to predict DNA structural features on a genome-scale
422 such as MGW, propeller twist (ProT), and electrostatic potential in the minor groove (EP) (Chiu
423 et al., 2017; Chiu et al., 2016; Zhou et al., 2013).

424 To determine which sequence motifs and sequence-defined structural features best predict
425 H-NS binding, we first asked which best explained the H-NS DBD arrangement in the *bgl* DRE
426 (***Figure 8A***). We found that our high-confidence DBD locations corresponded most closely to
427 TA-step and A-tract sequences with a narrow MGW, negative propeller twist, and highly
428 negative electrostatic potential. Using this set of sequence motifs and structural features that best
429 explained DBD locations in the *bgl* DRE as a guide, we next sought to predict the genome-wide
430 distribution of H-NS filaments. We performed this analysis by comparing the H-NS bound status
431 of 1000 bp windows staggered every 250 bp across the *E. coli* genome to the sequence and
432 structural features associated with those windows. We used least absolute shrinkage and
433 selection (LASSO) logistic regression trained on H-NS ChIP-seq data to predict the binding
434 pattern of H-NS, StpA, and Hha–H-NS (see Methods). LASSO regression yielded a minimal set
435 of DNA features that best explained the distribution of H-NS (***Figure 8B***). We found that a
436 simple model with only TA-step abundance, A/T content, and A-tract abundance was able to
437 predict H-NS ChIP-seq regions with high precision and recall (***Figure 8C***). Strikingly, these
438 sequence features, which also best matched DBD locations in an H-NS filament (***Figure 8A***), did
439 not gain significant predictive power when structural features were incorporated into the model.
440 Thus, both DBD locations and H-NS genomic distribution are best predicted by the combination
441 of three sequence features among which TA-step abundance is the most informative.

442 To test this model trained on H-NS ChIP-seq data, we next asked if it also predicted
443 genome-scale H-NS binding locations in the presence of Rif and in the *in vitro* Nitro-seq
444 experiments using chromatin reconstituted with H-NS, with StpA, or with H-NS:Hha. We found
445 this same sequence-motif-only model worked well to explain genome-scale binding distributions

446 in these different experiments (***Figure 8C***). As expected, the same model did a poor job of
447 predicting Fis binding sites *in vitro*, confirming its discriminatory power to differentiate H-NS
448 peaks from Fis peaks despite the similarity in A/T preference of these two proteins. Validating
449 our prediction approach overall, however, a similar model trained instead on the Fis Nitro-seq
450 data identified the RegulonDB Fis PWM as the most important feature for predicting the Fis
451 Nitro-seq distribution (***Figure S8-1A***). Although it is notable that LASSO selected only DNA
452 sequence motifs and not structural features for the final H-NS model, it is possible that the
453 relevant structural information is fully captured by the sequence motifs. Indeed, models trained
454 on H-NS Nitro-seq rather than ChIP-seq data selected the same three variables and performed
455 with similar high precision and recall (***Figure S8-1B***). We conclude that genome-scale H-NS,
456 StpA, and H-NS:Hha distributions can be predicted by DNA sequence motifs related to those
457 that explain DBD locations on the bp scale.
458

459 **DISCUSSION**

460 The biological function of H-NS depends on its complex structural properties, which includes
461 alternating head–head, tail–tail oligomerization of its NTD, flexibly connected DBDs,
462 paralogous subunits (e.g. StpA), and small-protein modulators (e.g. Hha) that combine to form
463 as-yet unresolved filament structures with DNA. This complexity enables formation of multiple
464 filament types, notably (*i*) bridged nucleoprotein filaments that inhibit both transcription
465 initiation and elongation and (*ii*) linear filaments that principally inhibit only initiation. Our
466 multimodal–multiscale approach, which combined new genome-scale reconstitution and
467 sequencing methods (Nitro-seq), conventional footprinting, direct detection of DBD locations
468 (TEN-map), molecular dynamics, and bioinformatics yielded three principal insights: (*i*) the
469 genome-wide locations of H-NS binding *in vivo* are determined principally by DNA sequence-
470 binding preferences, which are unchanged by the paralog StpA or modulator Hha; (*ii*) the DBDs
471 in an H-NS filament do not contact DNA with precisely fixed spacing but rather adjust both
472 contact point and orientation along adjacent minor groove positions; and (*iii*) HNS DBD
473 locations do not change in the switch from linear to bridged filaments, supporting a model of
474 DBD hemi-sequestration in linear filaments. We discuss each insight in the context of an overall
475 model of H-NS binding in which DNA sequence dictates both the location of H-NS filaments
476 genome-wide and the arrangement of DBDs within the filaments (***Figure 8***).

477 **H-NS genomic distribution is primarily determined by DNA sequence**

478 Multiple contributions to H-NS genomic distribution have been described, including AT-rich-
479 sequence-specific binding (Grainger et al., 2006; Kahramanoglou et al., 2011; Lang et al., 2007;
480 Lucchini et al., 2006; Navarre et al., 2006), competition with transcription (Chandraprakash and
481 Seshasayee, 2014; Rangarajan and Schnetz, 2018), and competition with other DBPs (e.g. in
482 anti-silencing gene regulation) (Will et al., 2015). However, the extent to which each of these
483 factors contributes to H-NS genomic distribution is currently uncertain. We predicted that if
484 transcription or DBPs played a dominant role in determining genome-scale H-NS filament
485 patterns, then *in vitro* reconstitution of H-NS filaments on genomic DNA would yield different
486 H-NS binding patterns than observed *in vivo* by ChIP-seq. In fact, we found only minor

487 differences between *in vitro* and *in vivo* H-NS binding patterns. Differences were attributable to
488 limited instances of transcription competing with H-NS binding and primarily to DBPs that
489 displace H-NS *in vivo* such as anti-silencing TFs (***Figures 1-3***). Further confirming the dominant
490 role of DNA sequence in determining H-NS locations *in vivo*, a statistical model based on only
491 three DNA sequence features (A/T richness, TA steps, and A tracts) could robustly predict H-NS
492 binding genome-wide (***Figure 8***). These findings do not contradict the reported roles of active
493 transcription or of anti-silencing by TFs in H-NS binding (Rangarajan and Schnetz, 2018; Will et
494 al., 2015). Rather, our findings suggest that active transcription and DPBs affect H-NS
495 distribution in limited ways at discrete sites with important regulatory consequences (e.g. TF-
496 rearrangement of H-NS at promoters during anti-silencing) but that the overall genomic
497 distribution of H-NS is determined by DNA sequence rather than by other proteins bound to
498 DNA (***Figure 8E***).

499 Our findings that StpA and Hha do not affect the sequence-specificity of H-NS filament
500 formation have important implications for how StpA and Hha confer greater regulation on
501 subsets of genes bound by H-NS (Banos et al., 2009; Lucchini et al., 2009; Muller et al, 2006).
502 Nitro-seq established that StpA and Hha–H-NS bind the same subset of DNA sequences as
503 bound by H-NS-only filaments (***Figure 2B; Figure S2–1***; ***Figure 3***; ***Figure S3–1A***; ***Table 1***).
504 These results agree with previous ChIP results showing extensive overlap between H-NS, StpA,
505 and Hha throughout the genome (Ueda et al., 2013; Uyar et al., 2009), but raise an obvious
506 question. If StpA and Hha do not alter the sequence-specificity of H-NS binding, then how do
507 they accomplish preferential regulation of subsets of H-NS bound genes?

508 One possibility is that different sequences have different affinities for H-NS binding. If
509 StpA or Hha increase binding affinity of H-NS filaments for DNA, as is consistent both with our
510 *in vitro* reconstitution data (***Figure 2***) and with other reports (van der Valk et al., 2017;
511 Srinivasan et al., 2013), then expression of genes whose sequences exhibit high affinity for H-NS
512 alone may not be changed by StpA or Hha. However, expression of genes whose sequences
513 confer weaker affinity for H-NS could be affected by StpA or Hha because these modulators
514 increase the affinity for these genes even though they do not alter sequence specificity, especially

515 at higher temperatures where H-NS affinity may be reduced (Bouffartigues et al., 2007; Shahul
516 Hameed et al., 2019). A second possibility is that the differential effects on gene expression
517 could reflect differential ability of certain sequences to promote bridging (see below), since both
518 StpA and Hha confer constitutive bridging on H-NS filaments (Boudreau et al., 2018; van der
519 Valk et al., 2017), and thus could have greater effects on sequences that favor linear H-NS-only
520 filament formation.

521 Our characterization of H-NS sequence preferences may also aid prediction of H-NS
522 binding locations in other bacteria. Previous attempts at predicting H-NS binding locations relied
523 on similarity to the high-affinity consensus sequence TCGATAAATT (Lang et al., 2007). We
524 found sequence characteristics of A/T richness, TA steps, and A tracts were sufficient to explain
525 the genome-scale distribution of filaments *in vivo* and of H-NS-only, H-NS–StpA, and H-NS–
526 Hha filaments *in vitro* (***Figure 8B***). The PWM based on the high-affinity consensus sequence as
527 well as DNA structure parameters added negligible predictive value, making this prediction
528 relatively simple to apply. Application of the algorithm to other enterobacterial species that rely
529 on H-NS will predict binding locations that can be validated by H-NS ChIP-seq.

530 **DBD position and orientation within H-NS filaments is flexible and set by DNA sequence**
531 Our finding that both H-NS DBD position and orientation are flexible within H-NS filaments is
532 consistent with reported binding patterns of H-NS on DNA (Badaut et al., 2002; Bouffartigues et
533 al., 2007; Tupper et al., 1994; Ulissi et al., 2014; Will et al., 2018). These previous footprinting
534 experiments typically revealed semi-regular spacing of ~10 bp between H-NS protected sites, but
535 also variation in spacing over a 5–30 bp range between a subset of sites. When bridged H-NS
536 filaments are pulled apart by ~22 pN force on beads attached to the two bridged DNAs, H-NS
537 contacts are lost in steps of multiples of ~11 bp (~1 helical turn of B-form DNA) (Dame et al.,
538 2006). However, many ~11-bp steps give no force signature yielding a mean step size closer to
539 two helical repeats. Possibly some contacts are too weak to give a force signature; alternatively,
540 some DBDs could remain bound to the NTD yielding an ~22 bp spacing. Further, deviations in
541 apparent DBD–DNA contact positions by ± ~2 bp are frequent. In agreement with this single-
542 molecule view of variation in contacts, we observed a correlation between the exact DBD

543 contact positions and the DNA sequence that suggests DNA sequence may dictate a lowest free
544 energy arrangement of DBDs within the constraints imposed by their flexible tethers to the H-NS
545 oligomer. Specifically, DBDs were located on the *bgl* DRE fragment at sequence and shape
546 features that confer high-affinity for H-NS (e.g. TA steps, A-tracts leading to narrow minor
547 groove width and negative EP), but were not observed at lower-affinity sites lacking these
548 features (Gordon et al., 2011) (***Figure 8A***). Thus, the precise position and orientation DBDs on
549 the minor groove as it aligns with the H-NS filament in every helical repeat is likely dictated by
550 the best minor groove complement in shape and charge to the DBD within reach of the linker.
551 The larger spacings of two or more helical repeats in contacts may reflect the absence of suitable
552 binding features near a given tail-tail junction in the H-NS oligomer so both DBDs at a given
553 junction remain associated with the NTD. Of note, we cannot exclude the possibility that both
554 DBDs at a junction contact one DNA duplex adjacent to each other, which could explain the
555 706R and 711F DBDs in our *bgl* DRE model (***Figure 7D***).

556 What can this flexibility in DBD arrangement tell us about the structure of H-NS filaments?
557 Our results do not define a specific conformation for the H-NS head–head, tail–tail oligomer.
558 However, the DBD locations we find are inconsistent with the oligomer structure observed in an
559 H-NS crystal that places the tail–tail junction to which the DBDs are tethered at ~30 bp intervals
560 relative to B-form DNA (Arold et al., 2010). If DBDs contact B-form DNA every ~10.5 bp in a
561 bridged filament in which one of the two DBDs at each junction binds one DNA duplex and the
562 other DBD binds the other duplex, then the H-NS NTD must adopt a conformation in which the
563 tail-tail junctions are ~10.5 bp or 33 Å apart. The crystal structure of the NTD oligomer places
564 these junctions ~95 Å apart, nearly three times the 10.5-bp distance on B-form DNA. Although
565 H-NS binding may distort DNA, it is unlikely to increase the helical pitch by a factor of 3.
566 Consistent with a shorter distance between tail–tail junctions, other conformations of the NTD
567 have been observed by MD simulation (Shahul Hameed et al., 2019; van der Valk et al., 2017);
568 these alternatives could enable explain the variable but on average ~11 bp spacing we and others
569 observe between neighboring DBDs. Future studies, possibly by cryo-EM, of a complete H-NS–
570 DNA filament are needed to resolve how H-NS monomers assemble to enable the semi-regular
571 but flexible orientations we observed for the H-NS DBDs.

572 **H-NS DBD contacts to DNA do not change in the switch from bridged to linear**
573 **conformations**
574 One of the most intriguing features of H-NS-based gene regulation is the capacity of H-NS
575 filaments to switch from binding one DNA duplex as a linear filament to binding two DNA
576 duplexes in a bridged conformation. The extent of DNA bridging *in vivo* and whether it varies
577 among genes or conditions remains unknown. However, the fact that H-NS can block transcript
578 elongation only in the bridged conformation where it creates topological traps to elongating
579 RNAP (Kotlajich et al., 2015; Boudreau et al., 2018) and the clear evidence that H-NS modulates
580 transcription elongation *in vivo* by stimulating ρ-dependent termination (Chandraprakash and
581 Seshasayee, 2014; Peters et al., 2012; Saxena and Gowrishankar, 2011) provides strong evidence
582 that bridging occurs to some extent *in vivo*. A structural basis for switching of H-NS between
583 linear and bridged filaments remains to be established.

584 The Dame and Arold groups have proposed a hemi-sequestration model of H-NS DBD
585 location that can explain linear-to-bridged switching (van der Valk et al., 2017; Shahul Hameed
586 et al., 2018). In the hemi-sequestration model, one of the two DBDs present at each tail–tail
587 dimerization interface in an H-NS filament binds to DNA and the second DBD is sequestered
588 through interactions with the N-terminal dimerization domain, possibly aided by buckling of the
589 α-helix connecting the two dimerization interfaces. Thus, the hemi-sequestered or closed
590 conformation enables only linear filament formation whereas the open conformation, which is
591 favored by binding of Mg^{2+} or Hha and possibly constitutive in StpA (Boudreau et al., 2018),
592 releases the sequestered set of DBDs so they can bridge to a second DNA duplex (***Figure 1A***;
593 ***Figure 8D***).

594 Our results validate the hemi-sequestration model because we observe no changes in the
595 locations of DBDs on the DNA between filaments that are obligately bridged (***Figure 5A***) and
596 filaments formed in conditions known to favor linear filament formation (high wild-type H-
597 NS/DNA ratio ***Figure 6***) (Kotlajich et al., 2015). Even though the precise *bgl*-DRE contacts and
598 orientation of the DBDs appear to be set by local sequence features and are sometimes weak or
599 absent at the typical ~10.5 bp intervals, these patterns show no evident change in conditions

600 favoring linear conformations where twice as many DBDs could be available for DNA contacts
601 (***Figure 6***). This same observation of no change in footprints at different H-NS/DNA ratios or at
602 high versus low Mg^{2+} concentration thought to govern linear–bridged preference has been
603 reported by several other groups (Badaut et al., 2002; Bouffartigues et al., 2007; Tupper et al.,
604 1994; Ulissi et al., 2014; Will et al., 2018). Taken together, these data strongly favor the hemi-
605 sequestration model of H-NS linear-to-bridged filament switching.

606 **Conclusion**

607 Our multimodal–multiscale approach to understanding the genome-scale basis of H-NS filament
608 formation and the rules governing H-NS DBD contact to DNA has clarified how linear and
609 bridged H-NS filaments are organized on DNA. The challenges now are to translate this
610 understanding to molecular resolution structures of these filament conformations and to develop
611 approaches that can distinguish locations of linear *versus* bridged filaments in living cells.
612

613 **MATERIALS AND METHODS**

614 **Materials**

615 Reagents were obtained from ThermoFisher (Waltham, MA, USA) or Sigma-Aldrich (St. Louis,
616 MO, USA), unless otherwise specified. Oligonucleotides (Table S2) were obtained from IDT
617 (Coralville, IA); ribonucleotide triphosphates (rNTPs), from Promega (Madison, WI); [α-^{32}P]GTP
618 and [γ-^{32}P]ATP, from Perkin Elmer (Waltham, MA); polyethyleneimine (PEI, avg. MW =
619 60,000), from Acros Organics;
620 (S)-1-(p-Bromoacetamidobenzyl)ethylenediaminetetraacetate (BABE), from Santa Cruz
621 Biotechnology; and DNA-modifying enzymes, from New England Biolabs (NEB; Ipswich, MA).

622 **Plasmid preparation**

623 An expression plasmid for wild type H-NS (pWTHNS) was constructed by Gibson assembly
624 using NEB HiFi reagents (Table S1). The *hns* coding sequence was amplified from MG1655
625 genomic DNA using primers #11779 and #11780 (Table S2) and the pET21d backbone was
626 amplified from pHNS using primers #11781 and #11782 before assembly. To introduce point
627 mutations in pWTHNS or pHisHNS (Table S1), single primer site-directed mutagenesis was
628 performed with Q5 DNA polymerase (NEB) and primer #8964 to change the Cys21 codon
629 (TGT) to a Ser (AGT) in pHNSC21S. To create pHNSC21SE102C, primer #8964 was used to
630 mutate the Cys21 codon and #8963 was used to change the Gln102 codon (GAA) to Cys (TGT).
631 Sequences of all plasmids described here were confirmed in key regions by Sanger sequencing.

632 **Protein Purification**

633 Native StpA and Hha were purified as described previously (Boudreau et al., 2018). C-terminally
634 His_{6x}-tagged H-NS was purified as described previously (Kotlajich et al., 2015).
635 *H-NS C21S purification*
636 H-NS C21S was purified as described for non-tagged H-NS in (Boudreau et al., 2018) with the
637 following modifications. Briefly, BL21 λDE3 cells transformed with pHNSC21S and pHiC were
638 grown in 2 L of LB supplemented with ampicillin (100 µg/mL) + gentamycin (10 µg/mL) to
639 OD600 ~0.6 before inducing expression of H-NS C21S with 0.5 mM isopropyl β-D-1-

640 thiogalactopyranoside (IPTG) for 2 h at 37 °C. Pelleted cells were lysed by sonication. H-NS
641 C21S was precipitated with addition of 0.6% (w/v) PEI and eluted with PEI elution buffer
642 containing 0.8 M NaCl followed by ammonium sulfate precipitation. Precipitated H-NS was
643 dissolved in nickel binding buffer and applied to a HisTrap Ni^{2+} column (GE Healthcare).
644 Fractions containing H-NS were mixed with TEV protease to remove the N-terminus His_{6x}-tag.
645 H-NS C21S was reapplied to the nickel column. Non-tagged protein was collected in the flow
646 through and dialyzed against Heparin Buffer (20 mM Tris-HCl pH 7.5, 130 mM NaCl, 100 µM
647 EDTA, 5% glycerol, 1 mM dithiothreitol (DTT)). H-NS C21S was then applied to a HiTrap Hep
648 column (GE Healthcare) and eluted with Heparin Buffer containing 1 M NaCl. Fractions
649 containing H-NS C21S were pooled and dialyzed against Binding Buffer (20 mM Tris-HCl pH
650 7.2, 10% glycerol, 1 mM DTT) supplemented with 130 mM NaCl. To concentrate H-NS, the
651 protein was applied to a Resource Q column (GE Healthcare). The column was washed with a
652 130–200 mM NaCl gradient in Binding Buffer over 7 column volumes. H-NS C21S was eluted
653 in 3 mL Binding Buffer with 500 mM NaCl. Fractions containing H-NS were dialyzed against
654 H-NS Storage Buffer (20 mM Tris-HCl pH 7.5, 0.3 M potassium acetate, 10% glycerol) before
655 storing at -80 °C. Protein purity (~90%) and yield (~5 mg) were determined by SDS-PAGE and
656 Qubit, respectively.
657 *Native WT and C21S E102C H-NS purification*
658 BL21 λDE3 cells were transformed with pWTHNS or pHNSC21SE102C before deleting *hns* by
659 P1 transduction using a lysate from the Δ*hns*::*kan* Keio strain (Coli Genetic Stock Center #9111;
660 (Baba et al., 2006). After confirming the *hns* deletion by PCR, 2 L of cells were grown
661 aerobically in Luria Broth–0.5% NaCl supplemented with 100 µg ampicillin/mL at 37 °C to
662 apparent OD_{600} 0.5 before inducing H-NS expression by addition of IPTG to 1 mM and
663 carbenicillin to 250 µg/mL followed by shaking at 16 h at 25 °C. Cells were pelleted at 3,000 × *g*
664 for 15 min at 4 °C and resuspended in 40 mL of lysis buffer (20 mM Tris-HCl, pH 7.2, 130 mM
665 NaCl, 10% glycerol, 1 mM DTT, 1 mM β-mercaptoethanol supplemented with
666 phenylmethylsulfonyl fluoride (PMSF) and protease inhibitor cocktail (PIC; 31.2 mg
667 benzamide/mL, 0.5 mg chymostatin/mL, 0.5 m leupeptin/mL, 0.1 mg pepstatin/mL, 1 mg
668 aprotonin/mL, 1 mg antipain/mL). Cells were lysed by sonication and the lysate was cleared by

669 centrifugation at 27,000 × *g* for 45 min at 4 °C. H-NS containing cell lysate was directly applied
670 to a HiTrap Heparin HP column (GE Healthcare) equilibrated with Binding Buffer with 130 mM
671 NaCl. H-NS was eluted at ~600 mM NaCl using a gradient elution from 130 mM–1 M NaCl
672 over 20 column volumes. Fractions containing H-NS were pooled and dialyzed against binding
673 buffer+130 mM NaCl. H-NS was applied to a 1-mL Resource Q column equilibrated with
674 Binding Buffer+130 mM NaCl. Remaining impurities were eluted over a gradient of 130–200
675 mM NaCl in 10 mL of Binding Buffer. H-NS was eluted with 3 mL of Binding Buffer+500 mM
676 NaCl. Fractions containing H-NS were dialyzed against H-NS Storage Buffer supplemented with
677 5 mM TCEP. Purity (~90%) and amount of protein (~4 mg) was determined by SDS-PAGE and
678 Qubit analysis, respectively. For tethered cleavage or ·OH cleavage assays, wild-type H-NS was
679 exchanged into a 3x stock of Filament Buffer (3x concentrations: 120 mM HEPES-KOH, pH
680 8.0, 300 mM potassium glutamate, and 15% glycerol).

681 **ChIP-seq sample preparation**

682 RL3000 cells (MG1655 F-, λ-, *ilv*G468+, *rfb*-50, *rph*+, *ybhJ*(L54->I), *yebN*(G25xxx->D),
683 *ycfK*::97bp Δ*InsB*-5 Δ*InsA*-5 Δ*InsAB*-5; (Ghosh and Landick, 2016) were grown in 50 mL MOPS
684 defined minimal medium with 0.2% glucose (GMM) (Neidhardt et al., 1974) at 37 °C with
685 vigorous shaking to an apparent OD_{600} of ~0.4 at which point either 100 µL of 50 mg Rif/mL in
686 methanol (100 µg Rif/mL final) or 100 µL of methanol as control and incubation at 37 °C with
687 shaking was continued for 30 min. Cell preparation, crosslinking, and immunoprecipitation was
688 completed as described previously (Mooney et al., 2009; Myers et al., 2013) with the following
689 modifications. After formaldehyde crosslinking, cells were resuspended in 250 µL IP buffer (100
690 mM Tris, pH 8.0, 300 mM NaCl, 1% TritonX-100, 1 mM PMSF), sonicated with the Misonix
691 Ultrasonic Liquid Processor (Model No. S-4000) for 1 hour at 60% power, 10 sec on and 10 sec
692 off, and treated with 2 ng RNaseA/µL (final concentration). To generate the input DNA control,
693 1/10th of the resulting lysate was removed and incubated with a Sepharose bead slurry (50-50
694 slurry of Sepharose Protein A and Protein G) overnight. The remaining lysate was pre-cleared
695 before adding the antibody by incubating the lysate with the Sepharose bead slurry at 4°C for 3
696 h. Beads were pelleted, and the cleared lysate was removed. Next, either 10 µL of polyclonal H-

697 NS antibody (Harlan Bioproducts) or 2 μL Beta antibody (Neoclone #WP0022; (Peters et al.,
698 2012) were incubated with the lysate overnight. The next day, DNA/protein/antibody complexes
699 were recovered with the Sepharose bead slurry and washed extensively before incubating at
700 65 °C for 30 min to reverse the crosslinks. Eluted DNA and input DNA (described above) were
701 purified with Qiagen QIAquick PCR purification kit and eluted in 58 μL of EB. DNA was
702 quantified with Qubit dsDNA HS assay reagents (ThermoFisher).

703 To prepare sequencing libraries for CHIP-seq, the DNA samples were first end-repaired by
704 incubating 30 μL of purified DNA from the IP with 0.4 mM dNTPs (Fisher Scientific), 3 U T4
705 DNA polymerase, 1 U Klenow Enzyme, and 10 U T4 PNK in 1x T4 DNA ligase buffer (NEB) in
706 a 50 μL reaction for 30 min at 20 °C. DNA was then purified using Qiagen QIAquick PCR
707 purification reagents. An A-overhang was added by incubating purified DNA with 1 mM 2′-
708 dATP and 5 U Klenow Exo 3′, 5′ minus (NEB #M0212) in 1x NEBuffer 2 (#B7002) in a 50 μL
709 reaction for 30 min at 37 °C. DNA was purified by using Qiagen MinElute PCR purification
710 reagents and eluted in 10 μL EB. Adapter and index oligo mixtures were made by incubating 30
711 μM universal adapter oligo and 30 μM index primer in a 10 μL reaction for 5 min at 100 °C and
712 slowly cooling back to room temp. Annealed oligos were ligated onto DNA fragments in a 30 μL
713 reaction containing 10 μL of purified DNA, 1 μL annealed oligo mixture, 12 U T4 DNA Ligase
714 (NEB), 1x DNA ligase buffer supplemented with 10 mM ATP for 15 min at 20 °C. DNA was
715 purified using Qiagen MinElute PCR purification reagents and resolved on a 2% E-gel
716 (ThermoFisher). Fragments ~270 bp long were excised from the gel and purified by the
717 QIAquick gel extraction kit (Qiagen). 20 μL DNA fragments were PCR amplified with 2 nM
718 primers 1, 2, and the respective index primer using 2x Phusion High-fidelity PCR master mix
719 with HF buffer (NEB: M0531) (Table S2). Final PCR fragments were purified with QIAquick
720 PCR purification reagents. Quality and quantity of the finished libraries were assessed using an
721 Agilent DNA1000 chip and Qubit dsDNA HS Assay reagents, respectively. Libraries were
722 standardized to 2 nM. Cluster generation was performed using the Illumina cBot. Paired-end, 50-
723 bp sequencing was performed using standard sequencing by synthesis (SBS) chemistry on an
724 Illumina HiSeq2500 sequencer. Images were analyzed using the standard Illumina Pipeline,
725 version 1.8.2.

726 **Nitrocellulose-seq assay**

727 Genomic DNA (gDNA) was isolated from stationary phase *E. coli* MG1655 cells using a
728 previously described CTAB isolation protocol (Wilson, 2001). Briefly, cells from an overnight
729 culture were diluted with TE (10 mM Tris-HCl pH 8.0, 1 mM EDTA) to an apparent OD_{600} of 1
730 and final volume of 5 mL and then lysed by addition of 133 µL 100 mg lysozyme/mL at room
731 temperature for 5 min. Proteins were removed from gDNA by incubating the solution with 267
732 µL 10% SDS and 5.3 µL 10 mg proteinase K/mL for 1 hour at 37 °C. Polysaccharides were
733 removed from gDNA by adding 667 µL 5 M NaCl and 667 µL 10% CTAB and incubating for 10
734 min at 65 ˚C. Remaining contaminants in the gDNA solution were removed by performing three
735 consecutive phenol:chloroform extractions where 3.3 mL of phenol:chloroform was added to the
736 6.7 mL gDNA solution. DNA was then precipitated by addition of 0.6 volumes of chilled
737 isopropanol and pelleted. Precipitated DNA was resuspended in 100 µL TE with 20 µg
738 RNaseA/mL and stored at -20 ˚C. Purity and concentration were determined with Nanodrop.
739 gDNA was sheared to fragments ~200-700 bp using the Misonix sonicator for 30 min at 60 watts
740 and 50% duty cycle.

741 To identify an optimal H-NS–DNA ratio for Nitro-seq that preferentially captured AT-rich DNA,
742 we tested different H-NS–gDNA ratios spiked with ^{32}P-labeled AT-rich PCR fragments from the
743 *bgl* operon and ^{32}P-labeled GC-rich PCR fragments from pBR322. The sheared gDNA had an
744 average size of ~880 bp) and the different H-NS–gDNA ratios were achieved by varying H-NS
745 concentration from 50 to 4000 nM with ~3.7 µM bp·mL^{-1} (equivalent to ~500 µg·mL^{-1}) gDNA.
746 Radiolabeled DNA was prepared using OneTaq Polymerase (NEB), 250 nM of the indicated
747 primers (Table S3), either genomic DNA, pMK110, or pBR322 as appropriate, and 2.5 µCi of
748 [α–^{32}P]dCTP per 50 µL reaction. Excess label was removed using ProbeQuant G50 micro
749 columns (GE Healthcare #28-9034-08). Nitro-seq reactions were performed in 250 µL of
750 Filament Buffer (40 mM HEPES•KOH, pH 8.0, 100 mM potassium glutamate, 5% glycerol)
751 supplemented with 8 mM magnesium aspartate containing gDNA (500 ng), 1 µL of each PCR
752 product (~50 ng DNA or ~8 nCi) and C-term His_6-tagged H-NS at 50-4000 nM. Complexes were
753 formed for 20 min at 20 °C before passing the mixture through a 0.45 µm nitrocellulose filter
754 (Millipore CAS# HAWP02400) at room temperature using Hoefer 10-well filtration apparatus

755 (FH224V). Filters were washed twice with Filament Buffer containing 8 mM magnesium
756 aspartate to remove non-specifically bound complexes. Bound DNA was eluted from the filters
757 by incubating filters with 400 µL of filter elution buffer (20 mM Tris-HCl pH 7.8, 0.2% sodium
758 dodecyl sulfate, 0.3M sodium acetate) for 2 hours at 30 ˚C as previously described (Papoulas,
759 1996). Then, DNA was ethanol precipitated, separated by 6% urea-PAGE, and visualized with
760 the Typhoon (GE Healthcare) (***Figure S2–1,2***). Total ^{32}P applied to, retained by, and passed
761 though the filter was determined by counting Cerenkov radiation. DNA eluted from the filters
762 with ~70% efficiency (***Figure S2–1A***). We found that 100 nM and 200 nM H-NS (31 and 64 H-
763 NS/kb gDNA, respectively) retained AT-rich fragments, but not GC-rich fragments (***Figure S2–***
764 ***1***). These H-NS–DNA ratios are similar to found previously to favor formation of bridged H-
765 NS–DNA filaments (Kotlajich et al., 2015). The optimization test also verified that short (<1 kb)
766 DNA fragments, which are suitable for direct HT-sequence library preparation, were retained on
767 the filter, indicating that they support H-NS–DNA filament formation. We found that longer
768 fragments (≥959 bp) were preferentially retained on filters at lower H-NS concentrations (e.g. 50
769 nM H-NS; 15 H-NS/kb) than shorter (≤630 bp) filaments (***Figure S2–1***). We chose 100 nM and
770 200 nM H-NS (31 and 64 H-NS/kb DNA) for subsequent experiments because these conditions
771 gave selective retention of AT-rich fragments short enough for use in HT-sequencing reactions.

772 A similar optimization was performed for StpA and for Fis. For StpA, 50 or 100 nM StpA
773 retained AT-rich but not GC-rich PCR fragments with selectivity similar to 100 nM H-NS. For
774 Fis, we used different radiolabeled PCR fragments containing known Fis-binding sites
775 (Kahramanoglou et al., 2011) (Table S3). We found that 5 and 12 nM Fis retained Fis-specific
776 PCR fragments on the nitrocellulose filter (***Figure S2–2***). No optimization was performed for
777 Hha–H-NS filaments because they are known to form at 1:1 Hha:H-NS ratio (Ali et al., 2013).
778 Thus, we added equimolar Hha to an H-NS concentration known to retain AT-rich fragments
779 (100 nM).

780 For Nitro-seq experiments, H-NS, StpA, or Fis were mixed with 500 ng sheared gDNA at
781 concentrations that selected AT-rich DNA fragments, but not GC-rich fragments (100 and 200
782 nM H-NS; 50 and 100 nM StpA; 5 and 12 nM Fis; ***Figure 2A***; ***Figure S2–1,2***) as described

783 above. Protein-DNA complexes were isolated as described above for the optimization
784 experiments except DNA was resuspended in water. Total gDNA applied to, retained by, and
785 passed though the filters was determined using Qubit dsDNA HS Assay reagents (***Figure S2–1***).
786 The percentage of gDNA retained by H-NS in our Nitro-seq experiments (~10%) was similar to
787 the percentage of the *E. coli* K-12 genome bound by H-NS *in vivo* (15%) (Grainger et al., 2006;
788 Kahramanoglou et al., 2011; Myers et al., 2013; Navarre et al., 2006), which further supports our
789 Nitro-seq conditions as being appropriate to determine the DNA sequence specificities of
790 bacterial chromatin proteins. DNA sequencing libraries were prepared for each sample using
791 NEBNext Ultra II DNA library reagents (NEB #E7103). The quality and quantity of libraries and
792 sequencing was performed like the ChIP-seq experiment described above except cluster
793 generation was not performed.

794 **ChIP-seq and Nitrocellulose-seq sequence processing and alignment**

795 Sequencing adapter reads and reads shorter than 30 nt were removed with Trimmomatic (version
796 0.) (Bolger et al., 2014) and the quality of remaining read were confirmed by FastQC (Andrews,
797 2010). Remaining paired-end reads were aligned to the MG1655 genome (Accession:
798 NC_000913.3) using Bowtie2 (version 2.3.4.2) with the parameters (-q --end-to-end -I 100 -X
799 800 --fr -t) (Langmead and Salzberg, 2012). Correctly paired reads were retained and duplicate
800 reads were removed with Samtools (version 1.9)(Li et al., 2009) and bedgraph files for
801 visualization were created with BEDtools (version 2.8) (Quinlan and Hall, 2010). More than
802 95% of reads mapped properly to the genome for ChIP-seq (Table S4) and Nitro-seq experiments
803 (Table S7) and were of high quality.

804 **ChIP-seq and Nitro-seq data analysis**

805 ChIP- or Nitro-seq patterns, read coverage in each condition was scaled for sequencing depth by
806 reads per million. To correct ChIP-seq patterns for variations in amounts of input DNA and in
807 sequencing, the $\log_2$ of control reads from input DNA was subtracted from the $\log_2$ of IP reads to
808 give a corrected read coverage. The RNAP baseline was set to the ChIP signal level in regions
809 known to be transcriptionally silenced (Mooney et al., 2009) and the H-NS baseline was set at
810 the average IP/input values from at least 5 regions with little signal. A similar analysis was

811 performed for Nitro-seq samples by correcting the nitrocellulose retained reads using input reads.
812 When compared, $\log_2$(ChIP/input) or $\log_2$(Nitro/input) samples were first quantile normalized
813 together using R. To compare Nitro-seq patterns, the genome was divided into 200 bp bins and
814 the average $\log_2$(Nitro/input) was calculated for each bin using a custom script. The density of
815 read coverage in each bin was compared between samples used to calculate Spearman
816 correlation coefficients (***Figure S3–1***).

817 To determine the enriched DNA segments more rigorously, we used MOSAiCS (Model-
818 based one and two Sample Analysis and Inference for ChIP-Seq Data) (Kuan et al., 2011),
819 specifically the two-sample analysis and MOSAiCS with a hidden Markov Model (MOSAiCS-
820 HMM) (Chung et al., 2014). This approach allowed determination of enriched regions for an IP
821 or nitrocellulose-retained sample compared to a matched input sample. For H-NS and RNAP
822 ChIP, 200-bp bins were used and duplicate reads were capped at 5 before fitting to a robust
823 background model using MOSAiCS-HMM. Using the viterbi algorithm, enriched regions were
824 determined using a false discovery rate (FDR) ≤ 0.05. Enriched region boundaries were adjusted,
825 and false positive peaks were filtered out using default settings in the MOSAiCS package.
826 Enriched regions present in both H-NS ChIP replicates were determined using BEDtools
827 "intersect" using default parameters to assign the enriched regions for cells with or without Rif-
828 treated cells (Quinlan and Hall, 2010). The H-NS binding patterns in the untreated cells was
829 similar to those reported using ChIP-chip in strain MG1655 also grown in GMM (Myers et al.,
830 2013) and to the ChIP-seq patterns reported for flag-tagged H-NS in MG1655 grown in broth
831 (LB 0.5% NaCl; ***Figure S1–1C***; (Kahramanoglou et al., 2011), confirming our analysis of H-NS
832 filaments *in vivo*. For the RNAP ChIP in Rif-treated cells, settings similar to untreated RNAP
833 ChIP were used find enriched regions, but using a non-HMM MOSAiCS fit for background and
834 mosaicsPeak parameters of FDR=0.05, maxgap=200, minsize=50, and thres=10. For Nitro-seq,
835 MOSAiCS analysis was performed as described for H-NS ChIP-seq except that bins were
836 created without removing duplicates and enriched regions were identified using the posterior
837 decoding algorithm. Nitro-seq enriched regions were defined as those identified in at least two of
838 the three replicates. The features of MOSAiCS-defined regions for each dataset are summarized
839 in ***Table 1***.

840 To compare MOSAiCS-identified regions between conditions, we used BEDtools (Quinlan
841 and Hall, 2010). First, we identified regions that overlapped between conditions using the
842 BEDtools "intersect" with options set to report the original regions (-wa -wb). A scatterplot of
843 the lengths of these regions was generated using Excel. The complete regions or fractions of
844 regions bound in only one condition were determined using BEDtools "subtract" with default
845 parameters. The similarity between two conditions was calculated as the Jaccard index using the
846 BEDtools "jaccard" command, which calculates the percentage of the length of filaments that
847 overlap out of the total length of filaments that do not overlap (Favorov et al., 2012). Thus,
848 completely dissimilar, non-overlapping data sets have a Jaccard index of 0% is whereas a
849 Jaccard index of 100% indicates that two datasets completely overlap.

850 To assign regions differentially bound by H-NS, the average ChIP signal from both
851 replicates in each condition was calculated using a custom script. The difference in the $\log_2$ ratio
852 of untreated H-NS signal and Rif-treatment H-NS signal ≥0.15 was used to assign regions of H-
853 NS depletion upon Rif treatment whereas a ratio ≤-0.15 was used to assign regions of H-NS
854 enrichment upon in Rif treatment (Table S5). Similar cutoffs were used for RNAP ChIP to
855 determine differences in RNAP occupancy in H-NS differentially bound regions. A correlation
856 between an H-NS differentially bound region and a change in RNAP binding was confirmed if
857 either MOSAiCS or average ChIP signal showed a change in RNAP binding at that H-NS
858 differentially bound region.

859 To compare H-NS filaments found only *in vitro* (Nitro-seq specific) to known TF binding
860 sites, we calculated the overlap between H-NS filaments and regions of TF-binding described in
861 RegulonDB (Santos-Zavaleta et al., 2019) with Bedtools "intersect". The overlap between Nitro-
862 seq specific regions with tsEPODs and heEPODs (Vora et al., 2009) also was calculated with
863 Bedtools "intersect". To calculate the *p*-value for these overlaps, the overlap between known
864 protein binding sites and 112 randomized sites of the same length as the 112 Nitro-seq specific
865 sites was determined 1000 times.

866 **FeBABE Conjugation**

867 H-NS C21S and H-NS C21S E102C were exchanged into Conjugation Buffer (10 mM MOPS,
868 pH 8.0, 0.5 mM EDTA, 200 mM NaCl, 5% glycerol) using PD SpinTrap G-25 columns (GE
869 Healthcare #28-9180-04) pre-equilibrated with conjugation buffer. FeBABE was charged by
870 incubating (S)-1-(p-Bromoacetamidobenzyl)ethylenediaminetetraacetate (BABE; Santa Cruz
871 Biotechnology) with $FeCl_3 \bullet 6H_2O$ as previously described (Greiner et al., 1997). H-NS variants
872 (50 μM) were incubated with 10-fold molar excess FeBABE for 2 h at room temperature to
873 conjugate FeBABE to H-NS. After conjugation, 7.6 μmol of conjugated H-NS was combined
874 with 20-fold-molar excess mPEG24 (ThermoFisher # 22713) for an additional 2 h at room
875 temperature. Samples were visualized on 10% Bis-tris gel (ThermoFisher) to determine the
876 percent conjugated (~50% for H-NS C21S E102C). Excess FeBABE was removed by applying
877 conjugated H-NS to a clean PD SpinTrap G-25 column equilibrated with a 3X stock of Filament
878 Buffer. Conjugation was also confirmed by the appearance of a second, slower migrating band
879 on 20% PhastGel (GE Healthcare). Fe·EDTA–H-NS was stored in aliquots at -80°C and
880 remained stable under these storage conditions for up to 1 year. The DNA-binding activity of the
881 conjugated protein was confirmed by electrophoretic mobility shift assay and by *in vitro*
882 transcription assays described previously (***Figure S4-2,3)*** (Boudreau et al., 2018; Kotlajich et al.,
883 2015).

884 **Tethered-nuclease mapping (TEN-map) Assay**

885 The 146-bp DRE DNA for the TEN-map assay was generated by PCR from a plasmid
886 pMK110 using primers #7486 and #12638 (Tables S1 and S2). To enable visualization by
887 phosphorimaging, one primer was 5′-end-labeled with [γ-^{32}P]ATP prior to the PCR reaction. The
888 PCR product was separated on 5% non-denaturing PAG, eluted from the gel overnight at 4 ˚C in
889 20 mM Tris-HCl pH 7.5, 1 mM EDTA, and 200 mM NaCl, and concentrated using QIAquick gel
890 extraction kit. Increasing concentrations of Fe·EDTA–H-NS (from 50 to 5000 nM) were
891 incubated with ~18 nM *bgl* DRE DNA for 20 min at 20 °C in 7.5 μL of 1X Filament Buffer
892 supplemented with 8 mM magnesium aspartate. Hydroxyl radical cleavage was initiated by
893 addition of 1 μL 2 mM H_2O_2 and 1 μL 2 mM ascorbic acid. Cleavage proceeded for 2 min at 20

894 °C after which 8 μL of the cleavage reaction was added to 100 μL TE-saturated phenol, pH 7.9
895 and 92 μL cleavage stop solution (20 mM EDTA, 20 μg glycogen) were added and samples were
896 vortexed for 10 sec. Samples were centrifuged to separate layers and 90 μL of the aqueous layer
897 was added to 280 μL of 100 μL ethanol to precipitate DNA. Samples were washed twice with
898 500 μL of 70% ethanol and resuspended in 4 μL of formamide stop dye (95% formamide, 20
899 mM EDTA, 0.02% xylene cyanol, 0.02% bromophenol blue). The samples were electrophoresed
900 through a 7% urea polyacrylamide gel (40.4 x 45.7 cm) in 0.5X TBE and alongside a Maxam-
901 Gilbert A+G ladder for alignment (Maxam and Gilbert, 1977) and MspI-digested, ^{32}P-end-
902 labeled pBR322 for size reference. The cleaved DNA was quantified using semi-automated
903 footprinting analysis (SAFA) (Das et al., 2005). The resulting peak areas were first normalized to
904 total signal in each sample as determined by ImageQuant (version 5.2; GE Lifesciences) analysis
905 of an unsaturated phosphorimage scan of gel and then adjusted to values above and below the
906 average peak area in each sample.

907 For the offset DNA experiment (***Figure S4–7***), the TEN-map assay was performed as
908 described above except using a 151-bp *bgl* DRE DNA amplified from pMK110 using 5′ ^{32}P-end-
909 labeled primer #14374 and unlabeled primer #12386. For the TEN-map assay on the 549-bp *bgl*
910 DRE fragment (***Figure 5***), DNA was amplified from pMK110 using 5′ ^{32}P-end-labeled primer
911 #7486 and unlabeled primer #7491. A mixture of Fe·EDTA–H-NS and wild-type H-NS at 4:6
912 ratio and concentration indicated in the figure legend was added to ~18 nM DNA in a 20 μL
913 reaction in Filament Buffer supplemented with 0.02% NP-40 and 100 μg acetylated BSA/mL
914 (supplemented Filament Buffer) to compare to the bridged filament cleavage described below.
915 Cleavage was initiated by addition of 1 μL 50 mM ascorbic acid and 4 μL 12.5 mM H_2O_2.
916 Cleavage continued for 2 min at RT before stopping the reaction with 25 μL 22.4 mM thiourea
917 and 20 μL TE. The cleavage products were recovered by phenol extraction and ethanol
918 precipitation, and then resuspended in 4 μL formamide stop dye. The cleavage products were
919 visualized and quantified as described above for the 146-bp *bgl* DRE DNA. To test the effect of
920 Mg^{2+} on the H-NS DBD location and orientation (***Figure 5B***), the TEN-map assay was
921 performed on the 549 bp DNA fragment as described except the amount of magnesium aspartate
922 was varied as specified in the figure legend.

923 **Hydroxyl radical footprinting**

924 H-NS filaments were formed on the same 146-bp *bgl* DRE DNA template used in the TEN-map
925 assay. Concentrations of unmodified H-NS from 50 nM to 4 μM (17–1360 H-NS/kb) were
926 incubated to ~20 nM 5′ ^{32}P-end-labeled *bgl* DRE DNA in 50 μL reactions in Filament Buffer
927 without glycerol. Filaments were allowed to form at 20 °C for 20 min prior to ·OH cleavage.
928 Cleavage was initiated by addition of 0.6 μL 100 mM ascorbic acid, 4 μL 0.15% H_2O_2, and 6 μL
929 fresh 50 mM Fe^{2+}-EDTA (50 mM $(NH_4)_2Fe(SO_4)_2$, 100 mM EDTA) and incubated for 2 min at
930 20 °C. The no-cleavage control was treated identically except 10.6 μL water was added in place
931 of cleavage reagents. ·OH was then quenched by addition of 80 μL 20 mM thiourea and 60 μL
932 of 0.3 M NaCl, 1 mM EDTA. Cleavage products were recovered by phenol extraction and
933 ethanol precipitation, and then resuspended in 4 μL formamide stop dye. Samples visualized as
934 described for TEN-map assay and quantified using SAFA (Das et al., 2005).

935 **Bridged H-NS cleavage assay**

936 Bridged H-NS filaments were formed using the previously published bridging pull-down assay
937 (van der Valk et al., 2018; van der Valk et al., 2017), with the following modifications. The 5'
938 32P-end-labeled, 549-bp *bgl* DRE DNA (see above) was used as the prey DNA. To form bridged
939 filaments, 5 nM biotinylated 685-bp DNA fragment (68% AT; Table S2) coupled to 3 μL M280
940 streptavidin dynabeads (ThermoFisher) was incubated with 5 nM prey DNA and H-NS in
941 supplemented Filament Buffer at 5–8 μM 6:4 WT H-NS: Fe·EDTA–H-NS as indicated in the
942 legend to ***Figure 5***. High levels of H-NS (>5 μM) are required to form bridged filaments in the
943 bridging/pull-down assay, possibly because DNA sequestration on the positively charged
944 streptavidin beads inhibits H-NS binding (***Figure S5–2B***; (van der Valk et al., 2017). Bridged
945 filaments were formed for 20 min at 20 °C with shaking at 1000 rpm in an Eppendorf
946 Thermomixer and then separated from unbound protein and DNA using a magnetic rack. Bead-
947 immobilized bridged filaments were then resuspended in 20 μL supplemented Filament Buffer
948 followed by addition of 1 μL 50 mM ascorbic acid and 4 μL 12.5 mM H_2O_2. Cleavage was
949 allowed to proceed for 2 min at RT before addition of 25 μL 22.4 mM thiourea and 20 μL TE.
950 DNA recovered and resuspended in formamide stop dye as described above. The amount of ^{32}P

951 retained on the beads was measured by counting Cerenkov radiation and compared to amounts
952 retained using only unmodified H-NS and prey DNA. Bridging efficiency was calculated as a
953 fraction of total prey DNA ^{32}P that was retained on the beads. Apparent bridging efficiency was
954 likely decreased by some DNA lost during sample processing. Cleavage products were then
955 visualized and quantified by gel electrophoresis and phosphorimaging as described above for the
956 TEN-map assay.

957 **MD simulation of FeBABE-H-NS bound to DNA**

958 Molecular dynamics simulations were run using the program OpenMM (Eastman et al., 2017)
959 with the Charmm36 force field (Best et al., 2012; Hart et al., 2012). Initial setup and post-
960 processing analyses were conducted using the program CHARMM (Brooks et al., 2009). We
961 obtained an initial starting model of H-NS bound to a 12-bp strand of duplex DNA from Vreede
962 and coworkers (Riccardi et al., 2019). We "mutated" the side-chain of Cys102 in that model to
963 an FeBABE moiety and generated force field parameters for the organic component of FeBABE
964 by analogy to existing functional groups in the Charmm36 force field. We modeled the Fe^{2+}
965 using a cationic dummy-atom model (Liao et al., 2017). We dissolved the H-NS/FeBABE/DNA
966 system in a cubic box of water with 70 Å edges and added Na^+ and Cl^- ions to reach an ionic
967 strength corresponding to 150 mM with neutral overall charge. The complete system contained
968 31,518 atoms. Following a short geometry optimization, the system was heated from 48 K to
969 298 K during 1 ns and equilibrated at 298 K and 1 atm for an additional 4 ns prior to production
970 simulations. The simulations employed the NPT ensemble using the Andersen thermostat and
971 MC barostat. Non-bonded interactions were cutoff above a distance of 12 Å with a switching
972 function from 10 Å to 12 Å and the integration time step was 1 fs. We placed a harmonic
973 restraint with force constant of 1 kcal/mol•A^2 on DNA backbone atoms to prevent unraveling at
974 the ends of the duplex, which we observed in initial tests. Under these conditions, we simulated
975 the system for 500 ns, taking snapshots every 10 ps.

976 In each frame, we calculated the distance from the Fe^{2+} to every C5′, because FeBABE-
977 induced cleavage is thought to occur by ·OH radical reacting with C5′-H (Balasubramanian et
978 al., 1998). We modeled the concentration of ·OH radicals at C5′ based on a diffusion model

979 where the concentration of radicals around the Fe^{2+} decays according to a Gaussian distribution
980 (Cheal et al., 2009). To account for cleavage sites that are shielded from solvent by the bound
981 protein, the average concentration of ·OH at each site was scaled linearly by the average solvent
982 accessible surface area of the corresponding C5′ methylene group (***Figure S7–2A***). The scaled
983 concentration at each site yields the cleavage propensities displayed in ***Figure 7A***. The
984 simulations used a relatively short 12-bp duplex in order to achieve reasonable computational
985 efficiency and to run simulations long enough to adequately sample the conformational
986 flexibility of the FeBABE. To model cleavage propensities for bp at greater distances from the
987 H-NS binding site, we assumed that long-range interactions with DNA do not influence the
988 overall behavior of FeBABE and thus estimated those cleavage propensities by adding additional
989 DNA to the saved trajectories after the simulation was complete.

990 **Modeling of DBDs in H-NS filaments**

991 The ·OH footprinting data for each H-NS concentration tested (0–4 μM titration), each strand,
992 and each independent replicate was normalized by dividing the signal in each lane by the average
993 signal within a lane. The resulting ratio was $\log_2$ transformed to center the data at zero. The $\log_2$-
994 normalized deviance from the average signal from each strand was separately fit to a Bayesian
995 multi-level model of the following form:
996

997 $$y_i \sim \text{Student's } t(\mu_i, \sigma, \nu)$$
998 $$\mu_i = \alpha_{\text{bp}[i]} + \beta_{\text{bp}[i]}[\text{HNS}]$$
999 $$\begin{bmatrix} \alpha_{\text{bp}} \\ \beta_{\text{bp}} \end{bmatrix} = \text{MVNormal}\left(\begin{bmatrix} \alpha \\ \beta \end{bmatrix}, \boldsymbol{S}\right)$$
1000 $$\boldsymbol{S} = \begin{pmatrix} \sigma_\alpha & 0 \\ 0 & \sigma_\beta \end{pmatrix} \boldsymbol{R} \begin{pmatrix} \sigma_\alpha & 0 \\ 0 & \sigma_\beta \end{pmatrix}$$
1001 $$\boldsymbol{R} = \begin{pmatrix} 1 & \rho \\ \rho & 1 \end{pmatrix}$$

1002 With the following weakly regularizing priors:

1003 $$\alpha \sim \text{Normal}(0, 10)$$
1004 $$\beta \sim \text{Normal}(0, 10)$$
1005 $$\sigma \sim \text{HalfCauchy}(0, 1)$$
1006 $$\sigma_\alpha \sim \text{HalfCauchy}(0, 1)$$

1007 $$\sigma_\beta \sim \text{HalfCauchy}(0, 1)$$

1008 $$\boldsymbol{R} \sim \text{LKJcorr}(2)$$

1009 The models were fit using the R package brms (version 2.10.0) (Bürkner, 2017) and default
1010 priors were used for any parameter for which a prior is not specified above.

1011 Similarly, the tethered-cleavage data for each concentration (0–3 μM titration) was
1012 normalized by first dividing each lane by a constant factor resulting from quantification of a
1013 short scan of the entire lane. The data was then centered by subtracting the average signal within
1014 each lane. The centered and normalized signal for each strand separately was then fit to a
1015 Bayesian multilevel, of the form described above, with the following priors:

1016 $$\alpha \sim \text{Normal}(0, 0.1)$$

1017 $$\beta \sim \text{Normal}(0, 0.1)$$

1018 Default priors were used for every parameter not specified above. Notably, the 4 μM and 5 μM
1019 concentrations were not included in the tethered cleavage fits due to their substantial deviance
1020 from linearity. Point estimates for each slope at each bp in the models above were estimated
1021 from the average of the posterior distribution for that slope. These estimates can be interpreted as
1022 the H-NS concentration-dependent change in signal at each bp with data-driven shrinkage
1023 towards the grand mean of slopes for every bp.

1024 To match the MD simulations with the *in vitro* data, the slope estimates for each strand in
1025 each data type were Robust-Z normalized using the following formula:

1026 $$y_{\text{scaled}} = \frac{y - \text{median}(y)}{1.4826 \times \text{MAD}(y)}$$

1027 where MAD is the median absolute deviation and 1.4826 is a scaling factor to convert the MAD
1028 to an estimate for the standard deviation (Hampel, 1974; Rousseeuw and Croux, 1993).
1029 Similarly, the expected 15-bp cleavage pattern of a single H-NS DBD (***Figure 7A***) was also
1030 scaled to a standard Normal using the formula above. Using a sliding window, the Manhattan
1031 distance between the scaled, tethered-cleavage estimates and the scaled, 15-bp expected cleavage
1032 pattern was calculated for each base centered on the sixth bp of the cleavage pattern (triangle in
1033 ***Figure 7B***). Due to the asymmetry of the expected cleavage pattern, we performed this
1034 calculation in both directions along the DNA corresponding to two different possible orientations

1035 of the H-NS DNA binding domain. Since this score is a distance, lower values indicate a closer
1036 match between the expected cleavage pattern and the tethered cleavage data.

1037 To assess the statistical significance of the MD match scores, we performed this same
1038 procedure on 1000 different random shuffles of the tethered-cleavage data for each direction of
1039 the H-NS DBD. We considered MD match scores below the 5th percentile of the random MD
1040 match scores to signify a statistically significant match between the expected cleavage pattern
1041 and the tethered cleavage data.

1042 To determine possible localizations of the H-NS DBD in the ·OH footprinting data, we
1043 performed the same procedure described above using the solvent accessibility of the 5′ carbon of
1044 the DNA duplex as the expected pattern of protection imparted by the H-NS DBD (***Figure S7–***
1045 ***2A***) and matched that pattern to the ·OH footprinting data (***Figure S6–3***).

1046 **Predicting H-NS binding patterns genome-wide**

1047 To generate a dataset for genome-wide prediction of the locations of H-NS filaments, the *E. coli*
1048 genome (accession U00096.3) was divided into a tiling array of 1000-bp windows staggered
1049 every 250 bp. A window was considered to be within a peak if over 50% of the window was
1050 covered by a called peak for that dataset. Any window that did not meet this criterium was
1051 considered as part of the unbound negative set. For each window the following sequence features
1052 were generated: a count of the As and Ts (A/T content), a count of 4mers matching the criteria
1053 for an AT tract, a count of 4mers matching the criteria for a TA step, a count of motif matches to
1054 the Lang et al. H-NS PWM (Lang et al., 2007), and a count of motif matches to the RegulonDB
1055 (Santos-Zavaleta et al., 2019) Fis motif. Motif matches were generated by running FIMO
1056 (version 5.05) (Grant et al., 2011) over the entire *E. coli* genome with a third-order Markov
1057 background model, searching on both strands, and using a *p*-value cutoff of 0.001 with no FDR
1058 correction. Each of these counts was then normalized by the length of the window. DNA
1059 structure features were generated using the DNAshapeR package (Chiu et al., 2016) run over the
1060 entire *E. coli* genome. The MGW, ProT, and EP bp level features were then Robust-Z
1061 normalized using data from the entire genome and the number of bases below a –2 cutoff on the
1062 Robust-Z scale for each feature was determined and normalized by the length of the window.

1063 To predict genome-wide locations of H-NS filaments, a LASSO logistic regression model
1064 was trained on the H-NS ChIP data using glmnet version 2.0-16 (Friedman et al., 2010). All
1065 features were centered and scaled before training. The LASSO model reveals the minimal set of
1066 DNA features needed for the prediction of a given dataset by only including non-zero
1067 coefficients for a feature if that feature provides independent information from other non-zero
1068 coefficients already present in the model. Since all input data was centered and scaled before
1069 training the model, the relative magnitude of each coefficient can be interpreted as the
1070 importance for that feature in predicting the outcome, with positive values indicating an increase
1071 in the probability of a region being bound by a protein when the associated feature is a higher
1072 value. Models were trained using 10-fold cross-validation with stratified sampling and the
1073 penalty parameter, λ, set as one standard error away from the minimum binomial deviance. λ
1074 was determined individually for each subsampled dataset using 10-fold cross-validation
1075 internally to test for sensitivity to the exact data used to train the model. Predictive performance
1076 for each ChIP and Nitro-seq dataset was tested by calculating the area under the precision-recall
1077 curve (AUC-PRC) using the method of Davis and Goadrich (2006) with the R package PRROC
1078 version 1.3.1 (Grau et al., 2015). The average, minimum, and maximum AUC-PRC was
1079 determined using the fitted models for each subsampled dataset to predict the binding locations
1080 for each ChIP and Nitro-seq dataset.

1081 **Data availability**

1082 Raw sequencing data, processed bedgraph, and bed files from the MOSAiCS output have been
1083 deposited in the Gene Expression Omnibus with accession number GSE157512. Custom scripts
1084 for ChIP-seq and Nitro-seq analysis are available at https://github.com/jmvera255/bio-script-
1085 library/tree/master/perl.

1086 **ACKNOWLEDGEMENTS**

1087 We thank Jocelyne Vreede (University of Amsterdam) for sharing coordinates for an H-NS
1088 DBD–DNA structure and for modeling FeBABE into the structure; Wilma Ross for providing
1089 purified Fis, advice on footprinting experiments, and equipment for Nitro-seq experiments;
1090 Jessica Vera for sharing scripts to analyze ChIP-seq and Nitro-seq data; Peter Freddolino for

suggestions of training sets for DBPs that bind a large fraction of the genome; and members of the Landick lab for many helpful discussions and comments on this manuscript. This work was supported by NIH grant GM38660 to R.L., Chemical Biology Interface Training grant (NIH T32 GM008505) to C.M.H., and the National Science Foundation Graduate Research Fellowship under grant number DGE-1256259 to B.A.S. and DGE-1747503 to C.M.H. High-throughput sequencing services were provided by the University of Wisconsin Biotechnology Center DNA Sequencing Facility. Computational resources for MD simulations were provided by the Extreme Science and Engineering Discovery Environment (XSEDE; allocation TG-MCB180084 to D.R.), which is supported by National Science Foundation grant number ACI-1548562.

1101 **TABLES**

1102 **Table 1. Enriched ChIP-seq and Nitro-seq regions identified by MOSAiCS**

SAMPLE	METHOD	TOTAL REGIONS	AVERAGE LENGTH	MEDIAN LENGTH	SMALLEST REGION	LARGEST REGION	FDR
Untreated	H-NS ChIP	301	2005	1221	220	15629	0.02
Rif Treated	H-NS ChIP	289	2059	1279	211	15486	0.03
Untreated	Beta ChIP	294	1829	875	94	22190	0.06
Rif Treated	Beta ChIP	1352	601	400	200	3400	0.05
100 nM H-NS	Nitro	407	2066	1436	242	14836	0.05
200 nM H-NS	Nitro	380	1902	1300	176	15281	0.05
50 nM StpA	Nitro	589	1817	1241	176	15281	0.05
100 nM StpA	Nitro	325	2217	1542	117	1600	0.05
Hha:H-NS	Nitro	436	2056	1490.5	122	14881	0.05
12 nM Fis	Nitro	888	917	818	209	4207	0.05

1103

1104

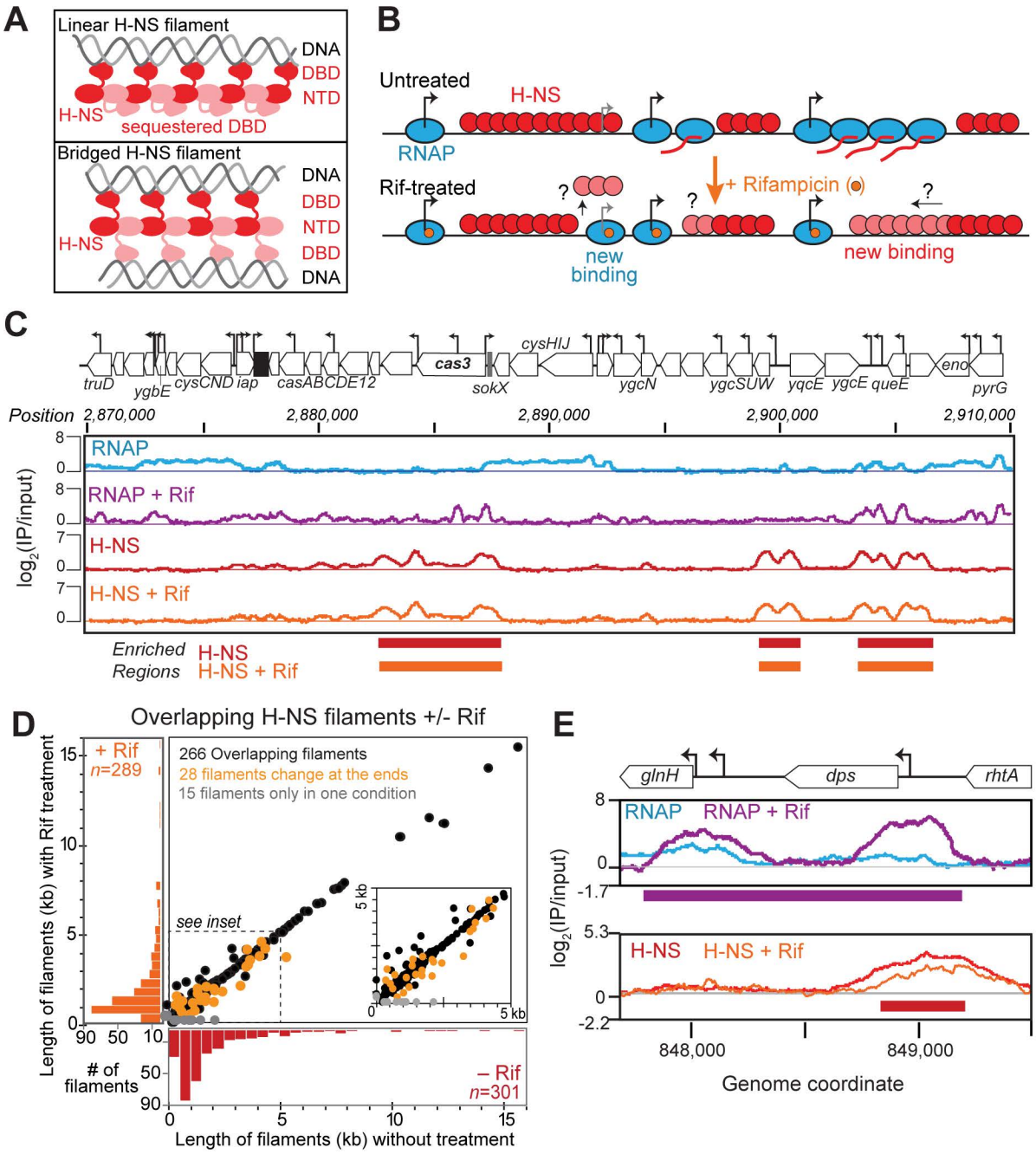

Figure 1. Halting transcription does not dramatically change H-NS distribution *in vivo*. (A) H-NS filament models. H-NS filaments can adopt either a linear or bridged conformation by contacting one or two DNA duplexes, respectively. Alternating monomers in the head–head, tail–tail H-NS oligomer are pink and red. In the proposed hemi-sequestration model of linear–bridged switching, half the DBDs contact one DNA duplex and the other half are sequestered by interaction with the NTD in a linear filament. To switch to a bridged filament, the sequestered DBDs are released and contact the second DNA duplex. (B) Schematic of ChIP-seq experiment. If H-NS (red) filament boundaries are determined principally by actively transcribing RNAP (blue), then treatment with rifampicin (Rif, orange), which traps RNAP at promoters, should change the H-NS binding pattern. (C) ChIP-seq locations of RNAP in the absence (blue) or presence (purple) of Rif and of H-NS in the absence (red) or presence (orange) of Rif. Representative ChIP-seq reads were normalized ratios to the IP input DNA reads and are shown

1118 as log2 ratios (*n=2*) with baselines of signal in transcriptionally silenced DNA (RNAP) or
1119 unoccupied regions (H-NS). H-NS enriched regions (i.e., filaments) identified by MOSAiCS are
1120 shown as boxes below ChIP traces. Genes (white boxes) are shown above the coverage tracks.
1121 TSSs (promoters) are indicated by black arrows (Thomason et al., 2015). (D) Length of H-NS
1122 enriched regions identified by MOSAiCS in Rif-treated (red) or untreated (orange) cells; binned
1123 distributions are shown on each axis. Filaments that changed in H-NS density at the ends are
1124 indicated by light orange dots. Filaments only present in one condition are indicated by gray
1125 dots. Number of filaments (*n*) shown in each graph are indicated. (E) H-NS filament at the *dps*
1126 promoter in untreated cells (red line) is lost after Rif treatment (orange line), likely due to the
1127 appearance of RNAP trapped at the *dps* promoter (purple line). Purple and red bars indicate
1128 enriched regions identified by MOSAiCS.
1129 Associated data: ***Figure S1–1***, ***Figure S1–2***, and ***Figure S1–3***.

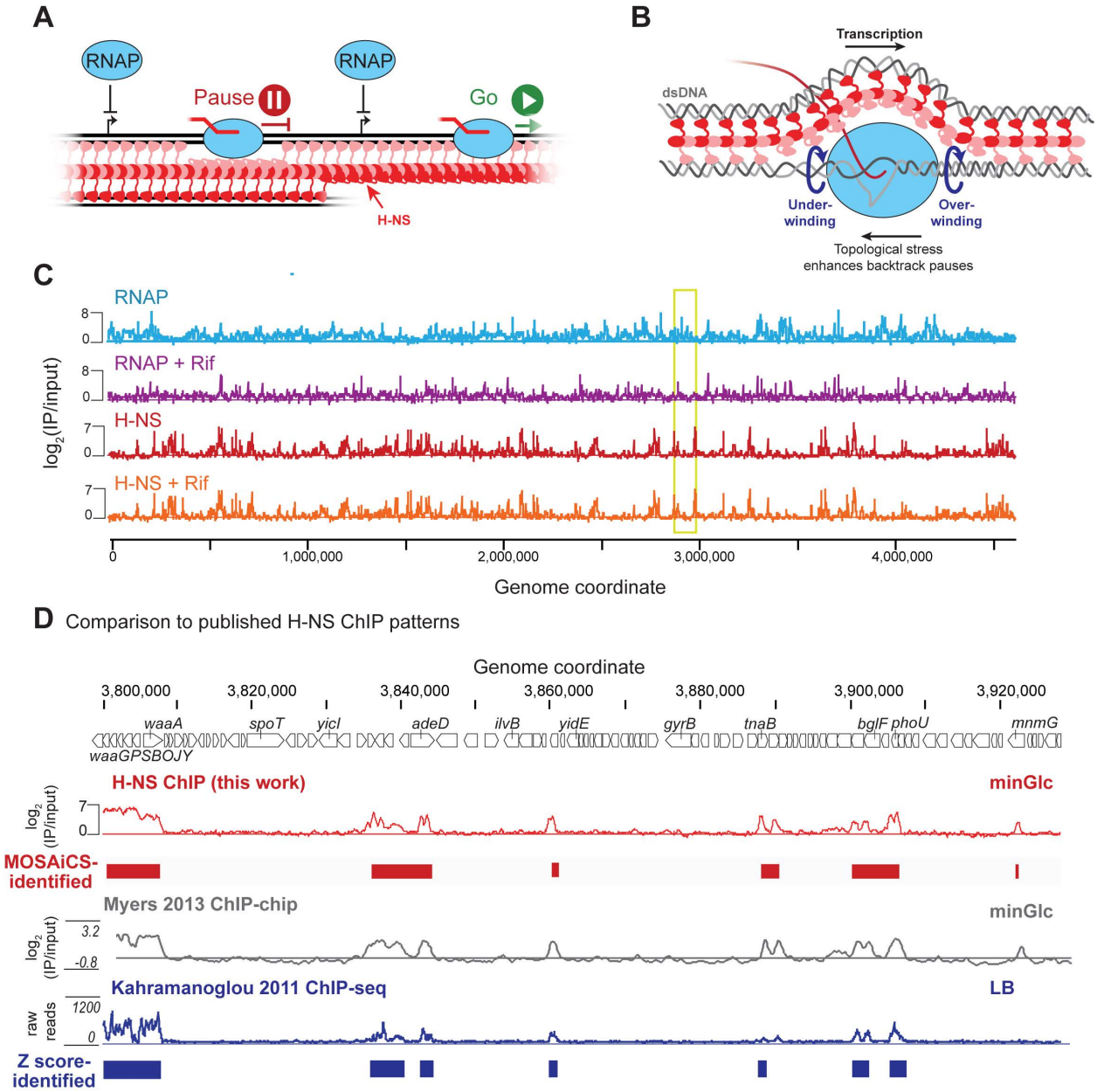

Figure S1-1. H-NS and RNAP ChIP-seq in untreated and Rif-treated cells.

(A) Both bridged and linear H-NS filaments can occlude RNAP from promoters, but only bridged filaments can stimulate pausing by an elongating RNAP. (B) Bridged filaments stimulate pausing by RNAP by creating a closed topological domain in which the DNA is overwound in front of RNAP and underwound behind RNAP. This torsional stress favors backtracking by RNAP and thus enhances backtrack pausing. (C) Normalized read coverage ($\log_2$(IP/input)) of the entire genome for H-NS and RNAP (Beta) IP in the presence (+Rif) or absence of rifampicin. Beta and H-NS ChIP were normalized separately, and the scales are indicated. Yellow box indicates the region shown in Figure 1B. (D) Comparison of H-NS filaments identified in this work by MOSAiCS (***Figure 1***) to the H-NS binding patterns reported by (Myers et al., 2013) using ChIP-chip profiling of *E. coli* K-12 MG1655 grown in minimal glucose medium (gray) and the H-NS filaments identified by (Kahramanoglou et al., 2011) using Z-score analysis of ChIP-seq data from *E. coli* K-12 MG1655 grown in rich medium (Luria broth–0.5% NaCl) (blue). The H-NS binding patterns are nearly identical in all three conditions.

1145

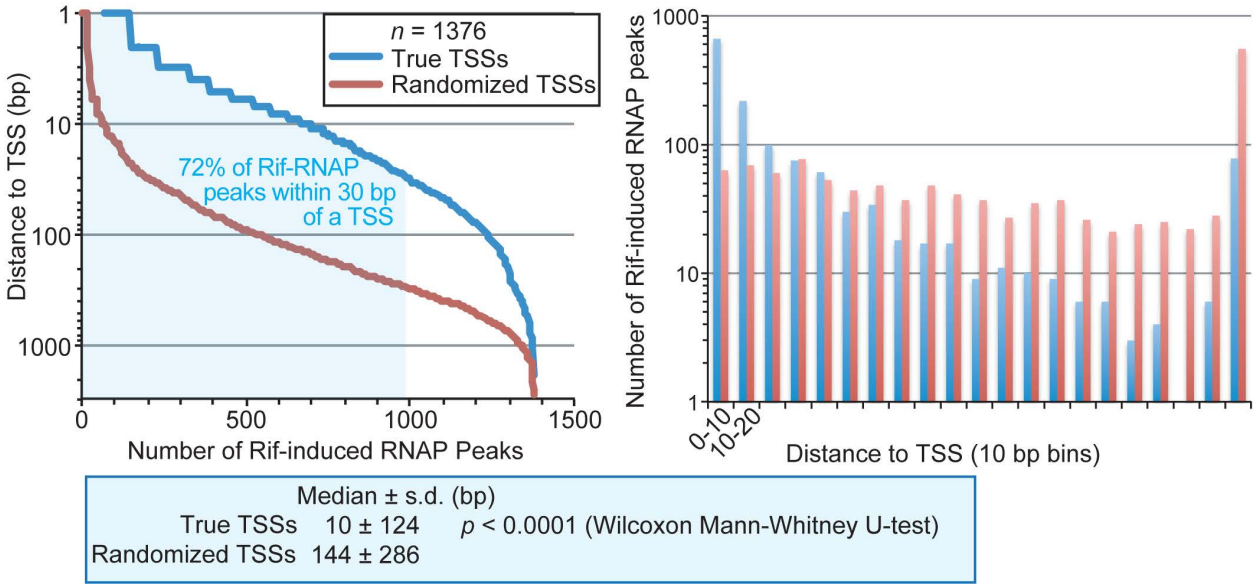

1146

1147 **Figure S1-2. RNAP relocates to known TSS upon Rif treatment.**

1148 Comparison of 1376 Rif-induced RNAP peaks to 11944 TSSs reported by (Thomason et al.,
1149 2015) for *E. coli* K-12 MG1655 growing in exponential phase in M9 glucose minimal medium.
1150 Distances from Rif-induced RNAP peaks to the nearest TSS were compared to the same
1151 calculation for randomized TSSs (*E. coli* genome rotated 90°).
1152

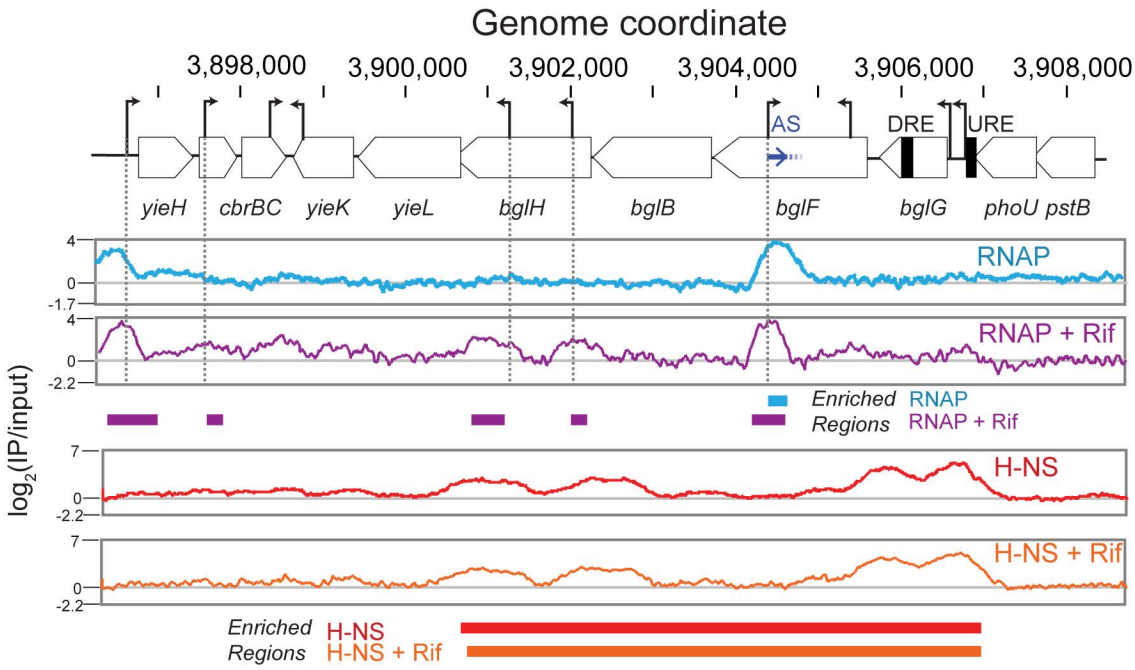

1153

1154 **Figure S1–3. Elimination of transcript elongation in the silenced *bgl* operon by Rif**
1155 **treatment does not change the H-NS binding pattern.**
1156 RNAP and H-NS ChIP-seq maps of the H-NS-silenced *bgl* operon in the presence or absence of
1157 Rif. Traces are representative of two replicates. The high-affinity H-NS binding sequences
1158 (downstream regulatory element, DRE, and upstream regulatory element, URE) are shown as
1159 black boxes. The *bglF* antisense transcription unit is shown as a blue arrow (AS). Enriched
1160 regions identified by MOSAiCs are indicated by solid bars below the plot (note that MOSAiCs
1161 did not identify the full length of the *bglF* antisense transcription unit). Other colors as in ***Figure***
1162 ***1***. Genes (white boxes) are shown above the coverage tracks. TSS identified in (Thomason et al.,
1163 2015) are indicated by black arrows.

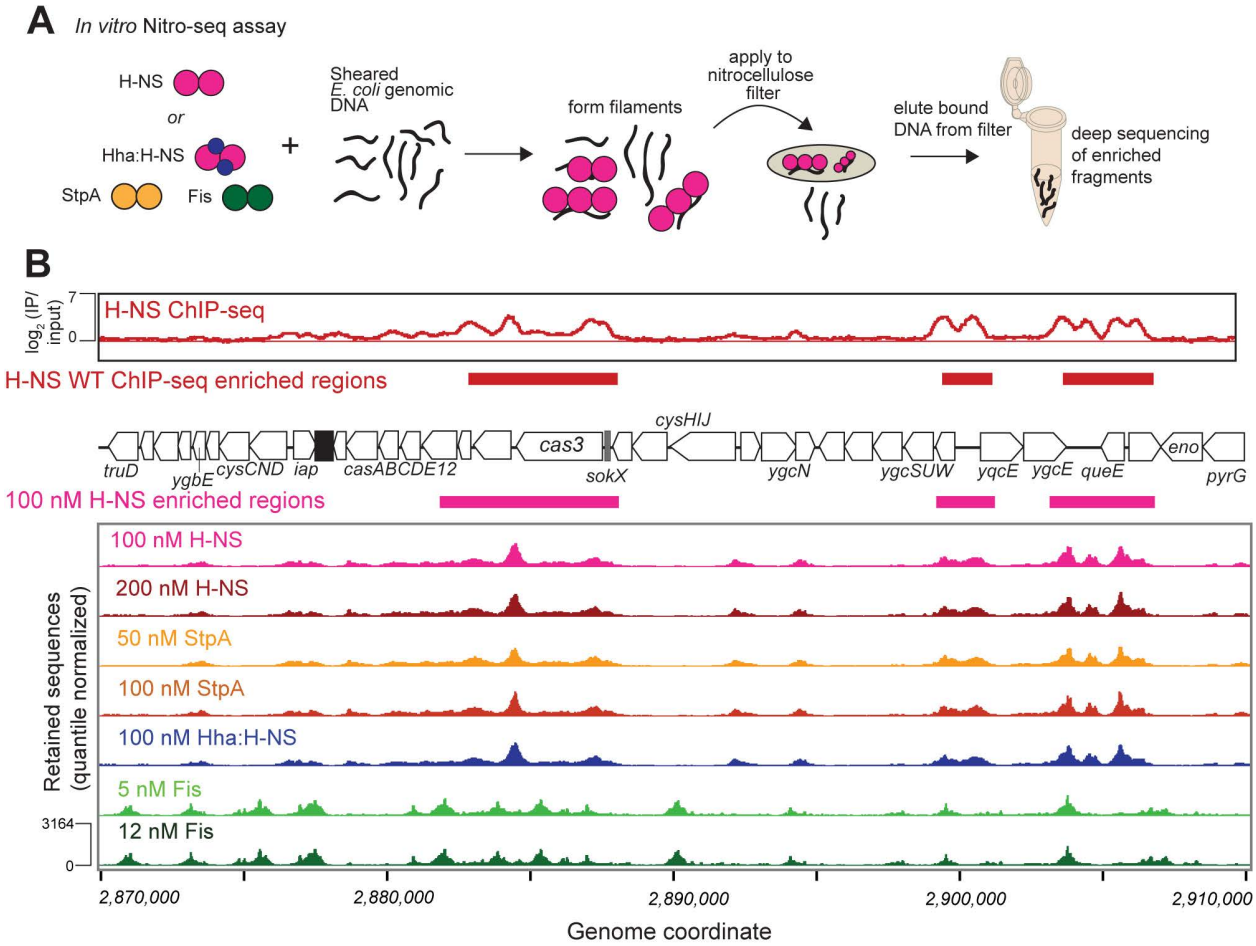

Figure 2. H-NS filaments can be reconstituted *in vitro.*
(A) The Nitro-seq assay to determine sequence binding preferences, illustrated here for H-NS, StpA, Hha:H-NS, or Fis. Proteins are mixed with sheared genomic DNA and then applied to a nitrocellulose filter (***Figure S2-1,2***). Two concentrations of H-NS, StpA, and Fis were compared to ensure features identified were not highly concentration-dependent (see ***Figure S2-1,2***). Retained DNA fragments are eluted and then subjected to HT DNA sequencing (see Methods). (B) Nitro-seq reads in a 40 kb region of the *E. coli* K-12 genome for H-NS (pink and dark red), StpA (yellow and orange), Hha:H-NS (blue) and Fis (light and dark green). Reads were quantile normalized to aid comparison between samples. Traces are representative coverage of three replicates. Normalized H-NS ChIP-seq coverage (***Figure 1***) is shown above the Nitro-seq data for comparison (bright red). Genes in this region are indicated by white boxes. CRISPR repeats are indicated by a black rectangle. The H-NS enriched regions (i.e., filaments) identified by MOSAiCS from the Nitro-seq (100 nM H-NS) and ChIP-seq reads are shown by colored bars. Associated data: ***Figure S2–1***, ***Figure S2–2***, ***Figure S2–3***, and ***Figure S2–4***.

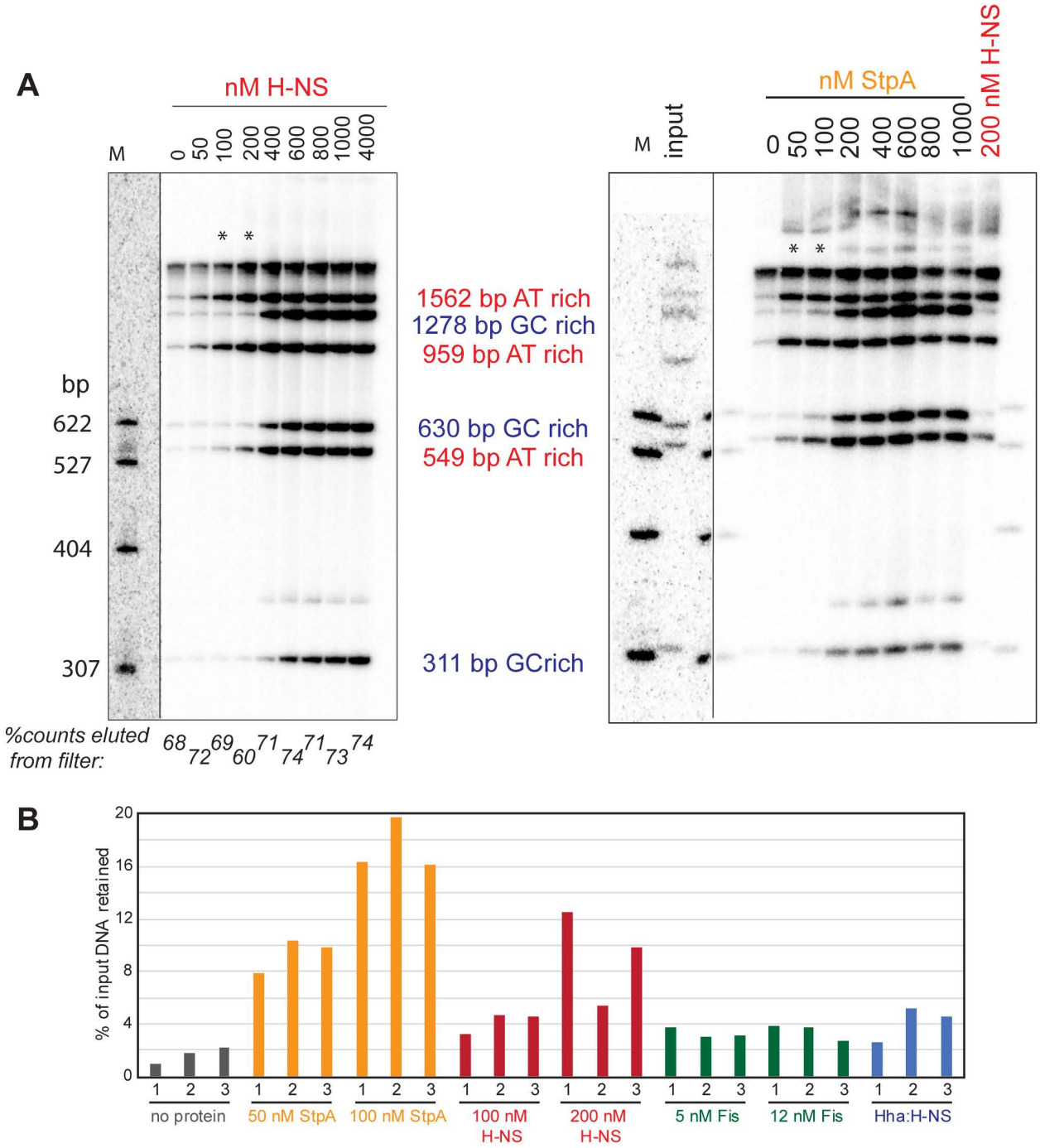

Figure S2–1. Identification of selective conditions for H-NS and StpA Nitro-seq.
(A) ^{32}P-labeled DNA fragments generated by PCR of the AT-rich *bglG* (red labels) or GC-rich DNA from pBR322 (blue labels) were mixed with sheared gDNA and either H-NS or StpA at the indicated concentrations and then incubated at 20 ˚C for 20 min. The samples were applied to nitrocellulose filters, washed, eluted, ethanol precipitated and then separated by 6% denaturing PAGE. PCR fragment sizes are shown between the gel panels colored to indicate GC(blue)- vs AT(red)- richness (Table S3). We predicted that H-NS and StpA would bind to AT-rich, but not GC-rich fragments (Bouffartigues et al., 2007; Dole et al., 2004). Asterisks indicate concentrations selected for Nitro-seq analyses. M indicates ^{32}P-labeled MspI digested pBR322 used as size ladder. The marker and input portions of the gels had lower signals than the samples,

1190 so the signal intensity was increased for clarity in these regions (boxed regions). (B) Fraction of
1191 sheared gDNA retained in each replicate of the nitrocellulose binding experiment. ^{32}P counts
1192 before and after elution were measured by liquid scintillation counting.
1193

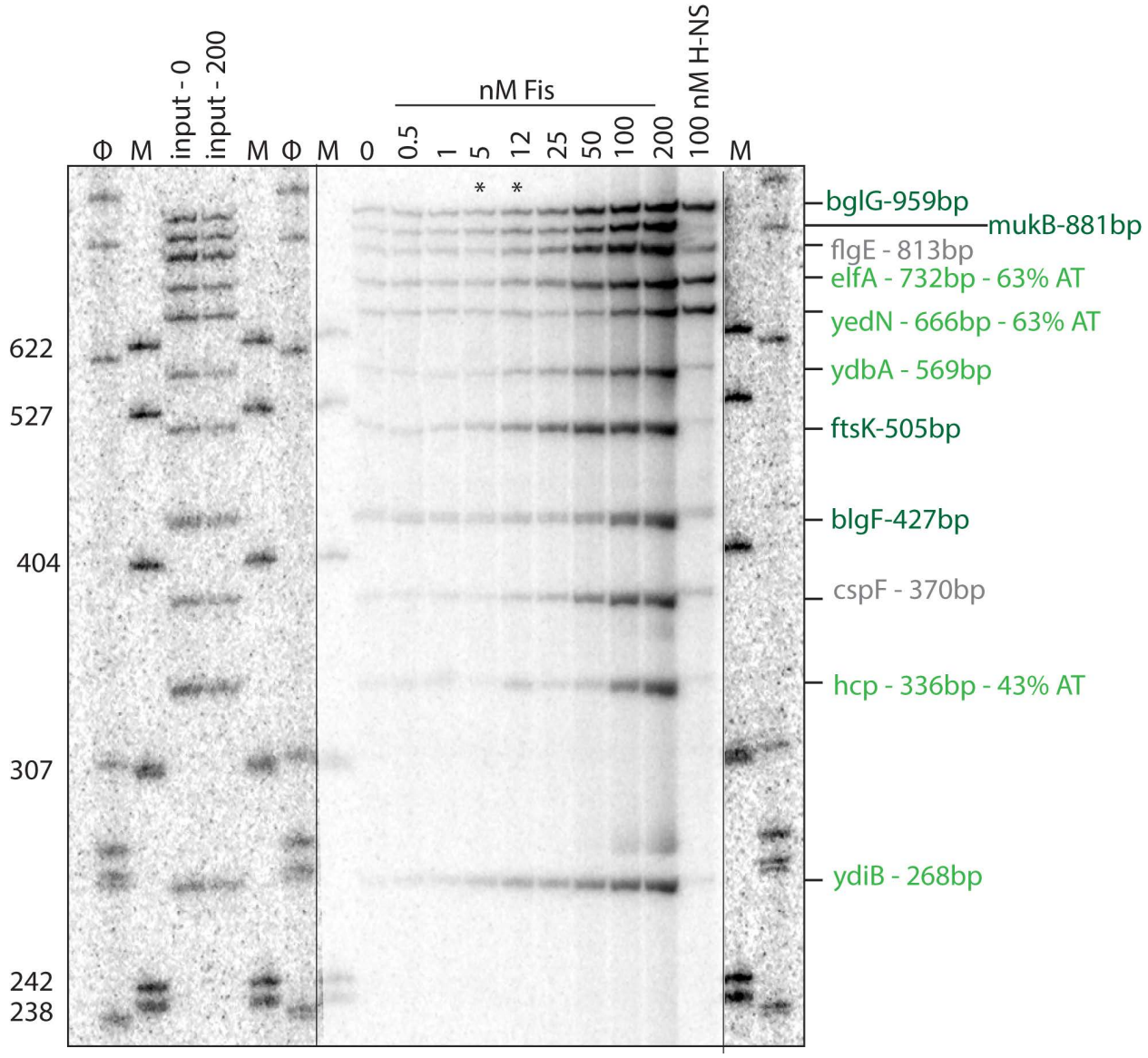

Figure S2–2. Determining selectivity of Fis in nitrocellulose binding assay.
To optimize conditions for Fis binding in the Nitro-seq assay, ^{32}P-labeled DNA fragments prepared by PCR of purified *E. coli* genomic DNA were mixed with sheared, deproteinized gDNA and Fis at the indicated concentrations and then incubated at 20 ˚C for 20 min. Samples were applied to nitrocellulose filters, washed, eluted, ethanol precipitated, and then separated by 6% denaturing PAGE. Fragment sizes are indicated on the right colored to indicate predicted Fis binding (no binding, gray; some Fis binding, light green; and strong Fis binding, dark green) (Table S3). As expected, the *flgE* and *cspF* fragments, which lack predicted Fis sites, were not retained on the filter, whereas other fragments like *ftsK*, which contains predicted Fis sites, were retained. Fis concentrations of 5 and 12 nM (asterisks) were selected for Nitro-seq. M, ^{32}P-labeled MspI digested pBR322. Φ, ^{32}P-labeled HaeIII digest of ΦX174 DNA. The signal intensities for the boxed left and right sides of the gel were relative to the samples for clarity.

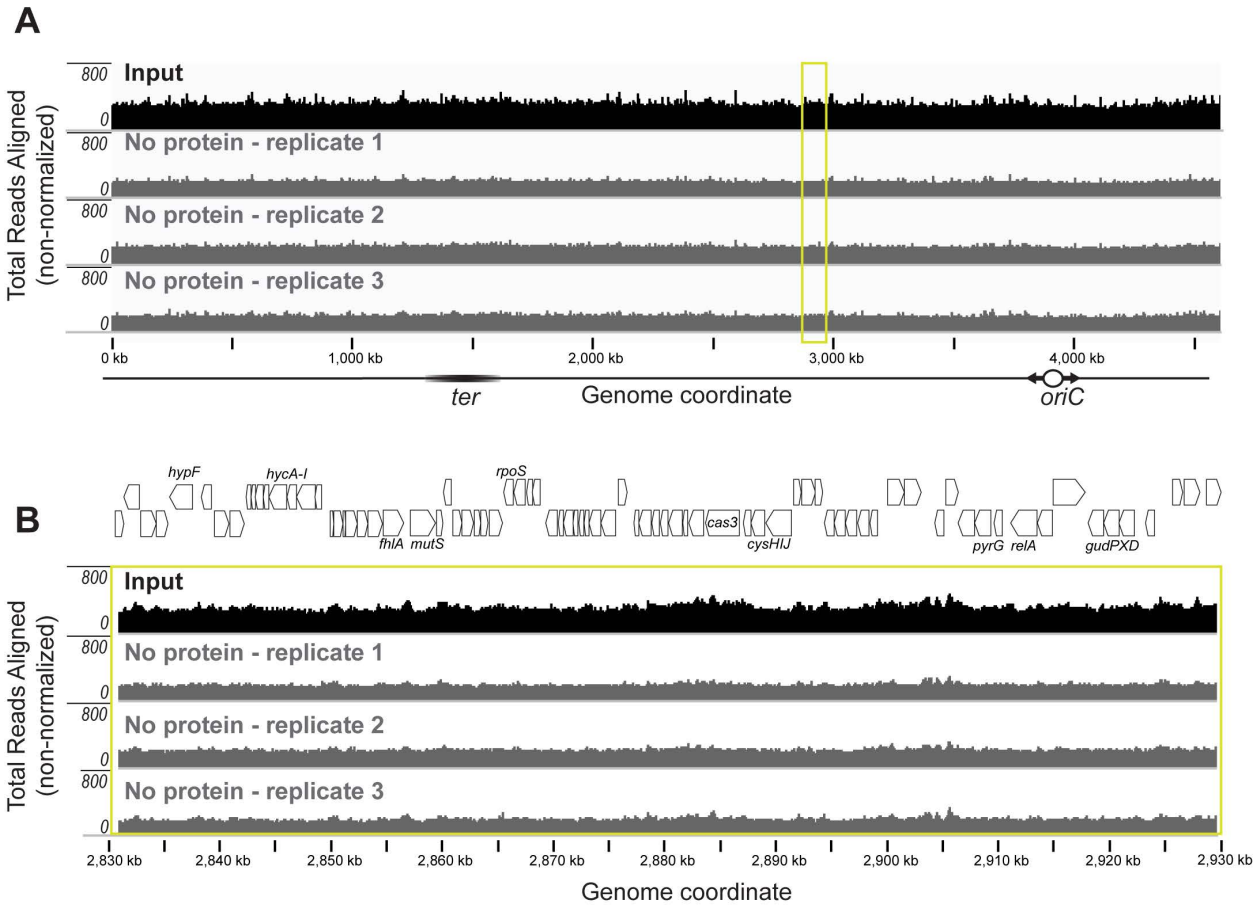

Figure S2–3. gDNA for Nitro-seq was a uniform across genome and free of protein contamination.
(A) DNA-seq read (unnormalized) for the input (black) and no protein samples (replicates 1-3; gray). (B) Expanded view of the yellow box in (A) showing even coverage in each input sample. Genes are shown by white boxes with a subset of names indicated. The no protein samples correspond to gDNA retained on the nitrocellulose filter. If residual protein was present in the sheared gDNA, peaks of enrichment would present in the no protein samples (we observed such peaks when gDNA was incompletely purified).

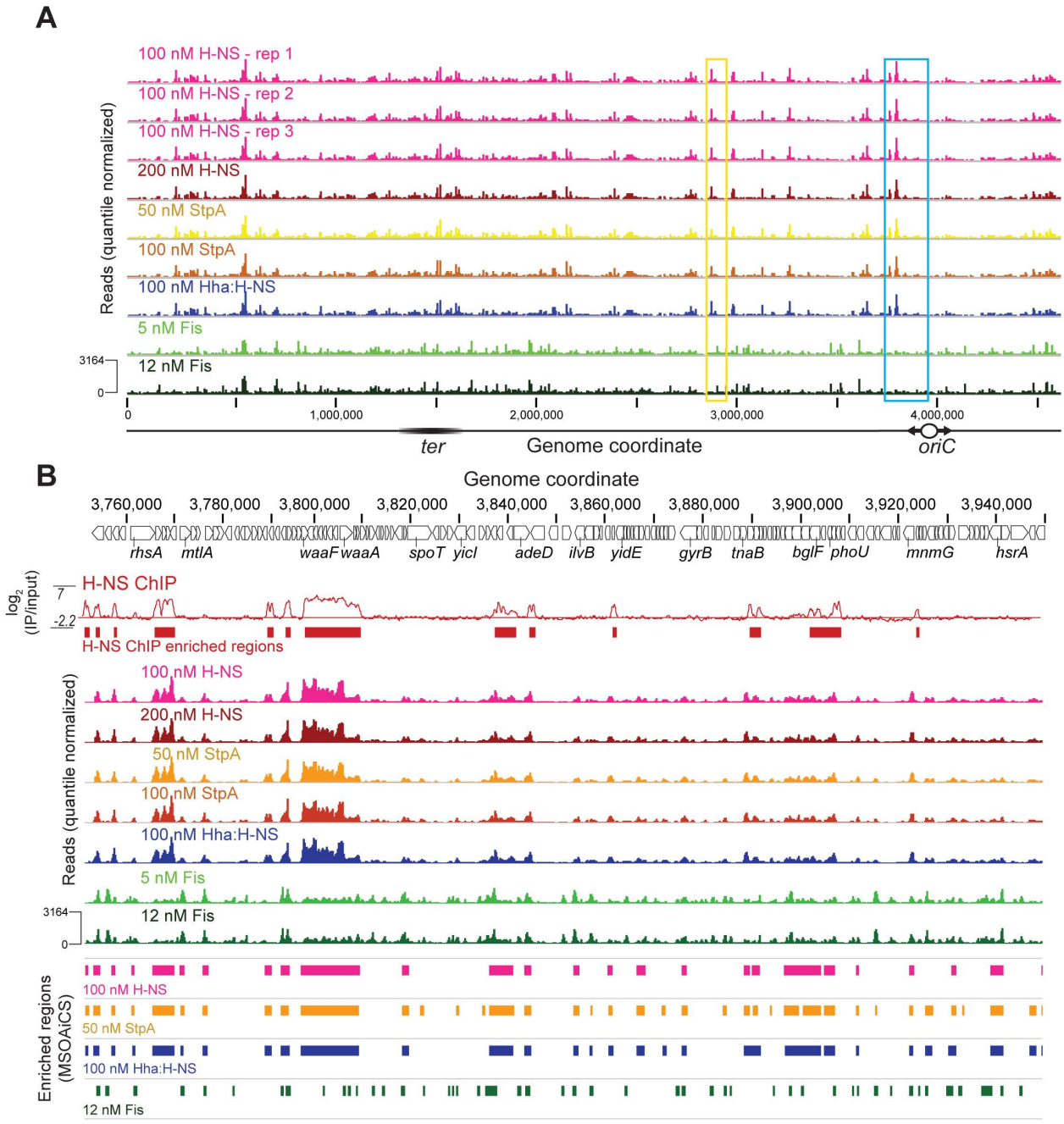

Figure S2-4. Binding of H-NS, StpA, Hha:H-NS, and Fis to genomic DNA in vitro.

(A) Genome-wide views of Nitro-seq results. Reads for Nitro-seq were quantile normalized to each other consistency, but not to ChIP-seq coverage. The yellow box indicates the region shown in ***Figure 2B***. The cyan box indicates the region shown in panel B of this figure. (B) View of Nitro-seq and H-NS ChIP-seq results in a 197 kb region of the genome. Traces are representative of triplicate samples. MOSAiCS enriched regions found in at least 2 of 3 replicates for each condition are shown by colored boxes below coverage plots.

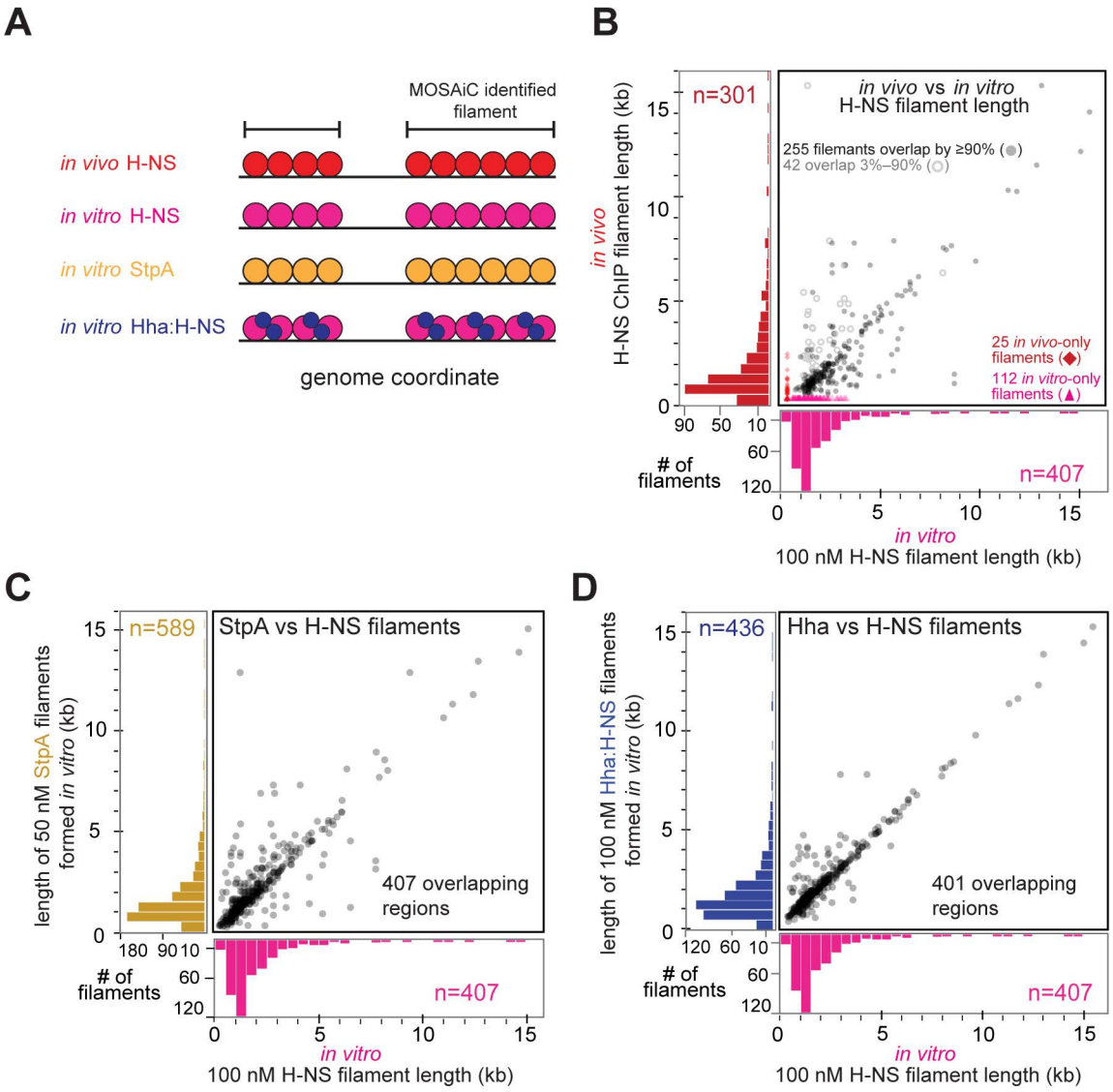

Figure 3. Nitro-seq revealed similar sequence specificity for H-NS *in vivo*, H-NS *in vitro*, StpA *in vitro*, and Hha:H-NS *in vitro*.

(A) Color code for comparisons of the filament lengths determined by MOSAiCs for H-NS, StpA, and H-NS:Hha. (B-D) Scatter plots of the lengths of filaments determined by MOSAiCS. The distributions of filaments lengths are shown as histograms on each axis. Lengths of *in vitro* 100 nM H-NS filaments are on each x-axis and the y-axis shows filament lengths for (B) *in vivo* H-NS, (C) 50 nM StpA, and (D) 100 nM Hha:H-NS filaments. The number of filaments (*n*) is indicated for each sample. The numbers of filaments overlapping with the *in vitro* H-NS filaments by at least 1 bp is indicated in each panel. (B) 297 filaments overlapped between *in vitro* and *in vivo* H-NS. Only 255 overlapped by 90% (i.e., the percent of the length of the Nitro-seq filament that overlaps with the ChIP-seq filament and vice versa) and 42 overlapped by <90% of the total length (gray outlined circles). For the 255 overlapping points, transparent black circles where plotted so that darker colors indicate more points on the graph. Filaments only found *in vitro* (112, pink triangles) or *in vivo* (25, red diamonds) are shown along the axes. (C) For each of the 407 overlapping filaments between *in vitro* StpA and *in vitro* H-NS, transparent black circles were plotted so that darker colors indicate more points on the graph. (D) Same as in C but for the 401 overlapping regions between *in vitro* Hha:H-NS and *in vitro* H-NS. Associated data: ***Figure S3–1*** and ***Figure S3–2***.

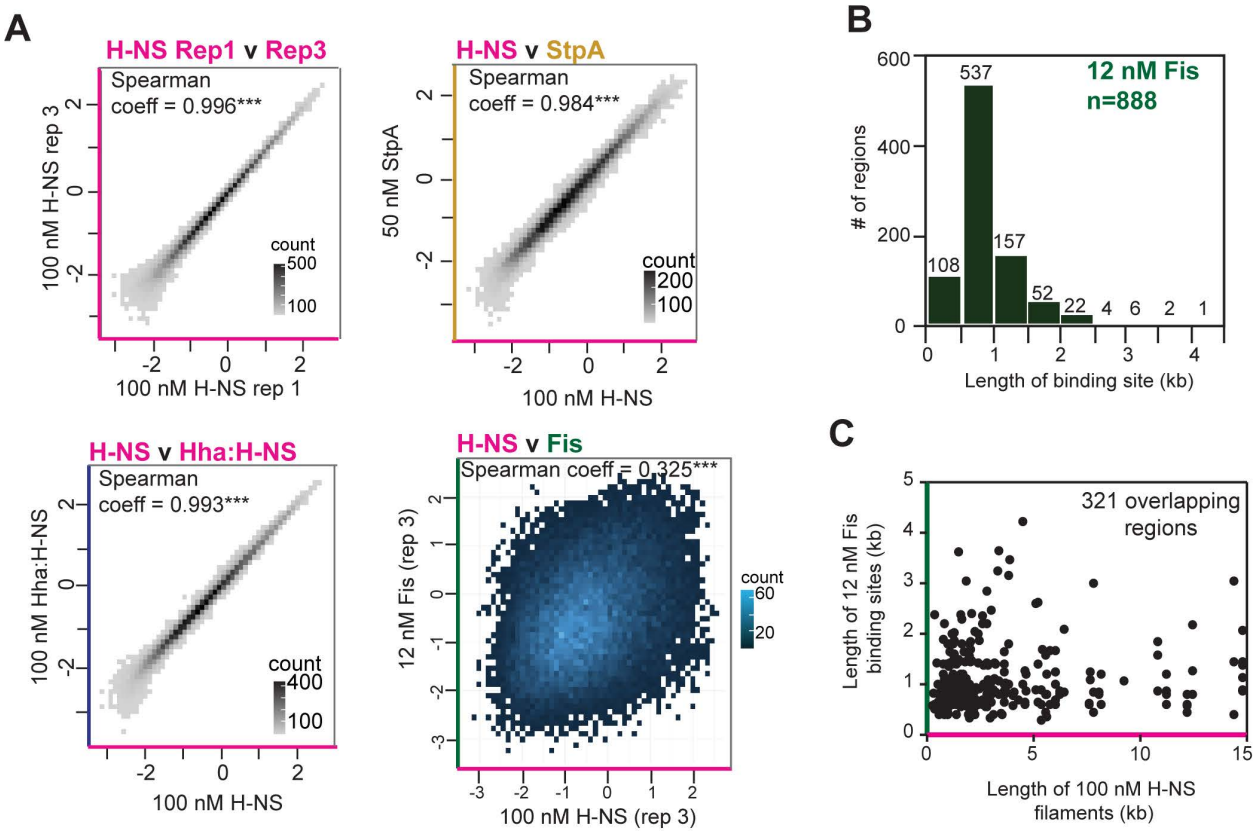

Figure S1-1. DNA binding pattern of H-NS in reconstituted filaments is distinct from Fis, but similar to H-NS in vivo, StpA, and Hha:H-NS.

These panels compare read densities binned into 200 bp intervals rather than the MOSAiCs-identified filaments shown in ***Figure 2*** to enable more direct comparison of the similarities and differences in binding patterns. (A) Binned scatter plot comparing average $\log_2$(Nitro-seq/input) in 200 bp bins across the genome for 100 nM H-NS replicate 1 vs. replicate 2 (pink axis); for 100 nM H-NS vs 50 nM StpA (gold y-axis); for 100 nM H-NS vs 100 nM Hha:H-NS (blue y-axis); and for 100 nM H-NS vs 12 nM Fis (green y-axis). *** indicates p-value $<2.2\times10^{-16}$ for the Spearman coefficient correlation test. (B) Distribution of lengths of Fis (12 nM) binding regions. The number of regions in each bin is indicated. (C) Comparison of lengths of 100 nM H-NS filaments (x-axis) overlapping with 12 nM Fis binding sites (y-axis). The total overlapping binding sites (312) resulted from 251 H-NS filaments overlapping with 321 Fis binding sites, indicating multiple Fis binding sites occur at the same genome coordinate as a single H-NS filament.

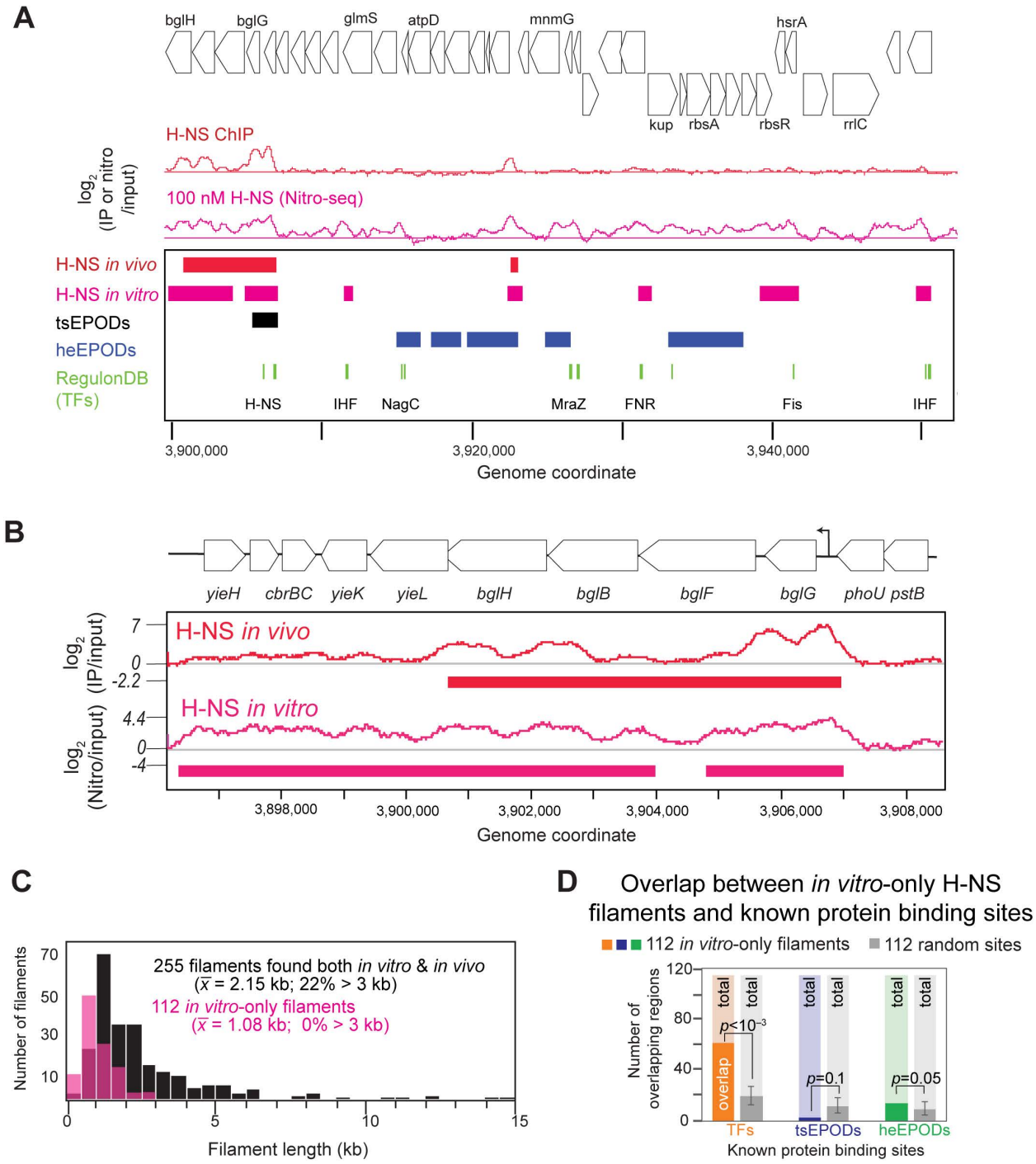

Figure S3–2. H-NS competes with other DBPs at some genomic loci *in vivo*.
(A) H-NS binding *in vivo* (ChIP-seq, red) and *in vitro* (Nitro-seq, pink) is similar, but some H-NS binding sites were only present *in vitro* as illustrated by the read coverage and MOSAICs regions identified in this genomic region. Locations of extended protein occupancy domains (EPODs) that are transcriptionally silent (tsEPODs) or highly expressed (heEPODs) are indicated (black and blue respectively (Vora et al., 2009). TF binding sites as annotated in RegulonDB are also shown (green; Santos-Zavaleta et al., 2019). (B) View of H-NS ChIP-seq and H-NS Nitro-seq normalized read coverage at the *bgl* operon. MOSAiCS regions indicated by bars. Similar H-NS binding patterns were observed at the *bgl* operon *in vivo* (ChIP-seq, red) and

1269 *in vitro* (Nitro-seq, pink). (C) Comparison of Nitro-seq-specific (Class 2) and overlapping (Class
1270 1) H-NS binding region length distributions. (D) Number of Nitro-seq-specific (Class 2)
1271 filaments that overlap with three types of known protein binding sites: transcription factor
1272 binding sites found in RegulonDB (TFs; dark orange), transcriptionally silent extended protein
1273 occupancy domains (tsEPODs; dark blue), or highly expressed EPODS (heEPODs; dark green).
1274 The total filaments in class 2 (112) is shown in light colors for each comparison. Statistical
1275 significance of this overlap was determined by comparing it to the overlap of 112 random sites
1276 generated 1000 times and these known protein binding sites (gray bars and p-values). Error bars
1277 indicate the 97.5% quantile of the random overlap values at the top and the 2.5% quantile of the
1278 random overlap values at the bottom.

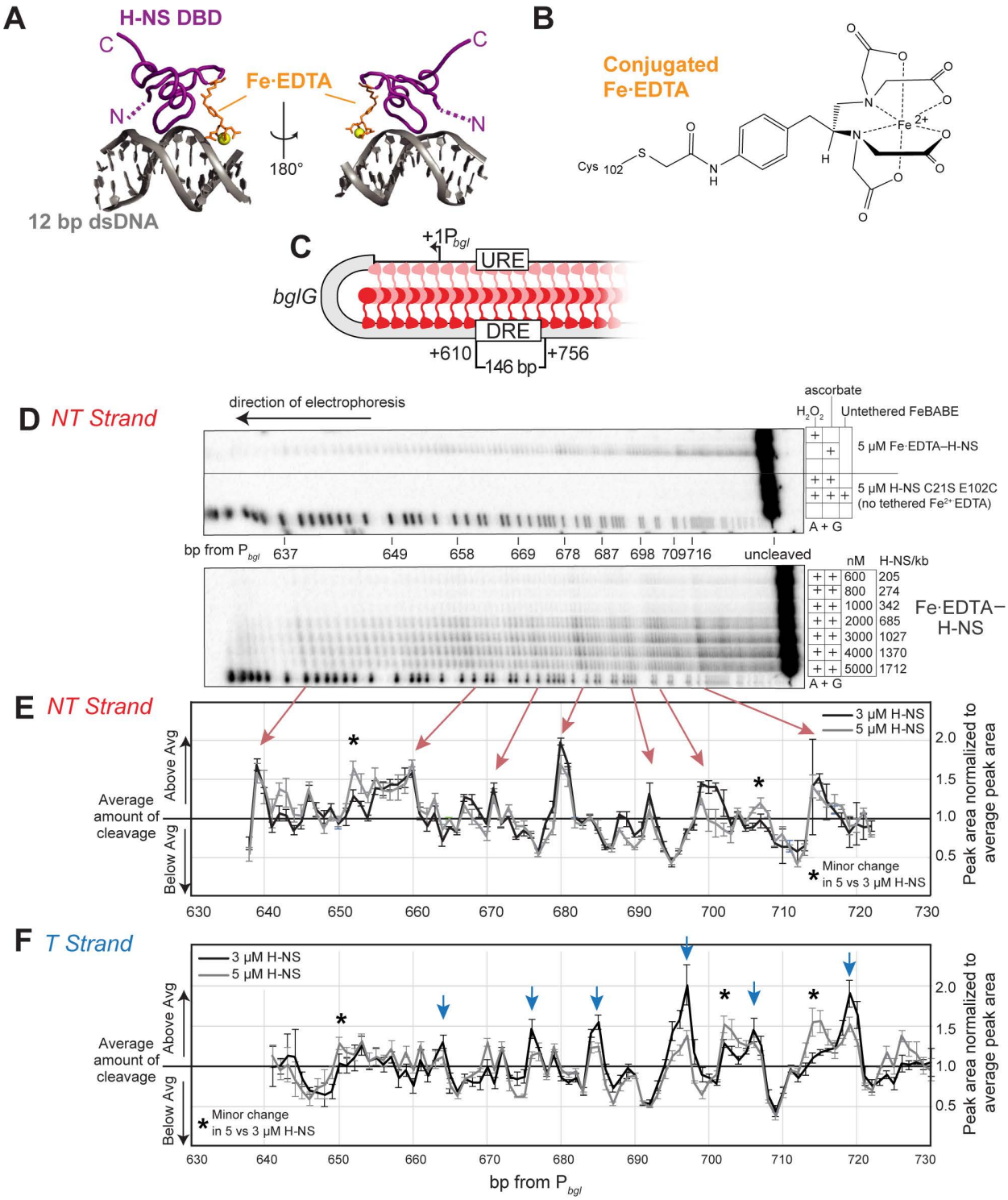

Figure 4. TEN-map cleavage of *bgl* DRE DNA.
(A) Model of the H-NS DBD (purple; PDB 2L93) bound to 12 bp duplex DNA (gray; (Riccardi et al., 2019) with Fe·EDTA (orange) added at position 102. The linker connecting the DBD to the N-terminal oligomerization domain is shown by the dashed line. (B) Structure of Fe·EDTA conjugated to Cys102. (C) The 146-bp DRE DNA fragment used in the TEN-map assay from the region of the *bgl* operon 610 to 756 bp downstream of the promoter (P_{bgl}), which encodes a

1286 known high-affinity binding region (DRE; downstream regulatory element; (Dole et al., 2004).
1287 H-NS (pink and red monomers as in Figure 1) bound at both the DRE and upstream regulatory
1288 element, URE, may form a bridged filament. (D) Denaturing 7% PAG showing Fe·EDTA–H-NS
1289 cleavage pattern of the 146-bp DRE DNA labeled on the NT strand. Increasing concentrations of
1290 Fe·EDTA–H-NS were added to ~20 nM DNA to form filaments. Cleavage was initiated with
1291 addition of both 2 mM H_2O_2 and 2 mM ascorbic acid (bottom panel). Little to no cleavage was
1292 observed in the presence 5 μM Fe·EDTA–H-NS with addition of either 2 mM H_2O_2, 2 mM
1293 ascorbic acid, or water (top). Tethered Fe·EDTA was also required for cleavage as addition of
1294 free FeBABE to filaments formed with 5 μM H-NS C21S E102C did not result in cleavage of
1295 the DNA (middle). A+G indicates Maxam–Gilbert sequencing ladder. (E & F) Quantification of
1296 peak areas using semi-automated footprinting analysis (SAFA) analysis at 3 and 5 μM
1297 Fe·EDTA–H-NS on the NT (E) or T (F) strands. Peak areas normalized to amount loaded in each
1298 lane and then the average peak area in each lane. Peaks areas above 1 indicate cleavage hot spots
1299 (arrows) and peak areas less than 1 indicate areas of lesser cleavage. Asterisks indicate areas that
1300 showed a slight increase in cleavage in 5 μM Fe·EDTA–H-NS compared to 3 μM Fe·EDTA–H-
1301 NS. Error bars show standard deviation of three replicates. Associated data: ***Figure S4–1***, ***Figure***
1302 ***S4–2***, ***Figure S4–3***, ***Figure S4–4***, ***Figure S4–5***, ***Figure S4–6***, and ***Figure S2–7***.

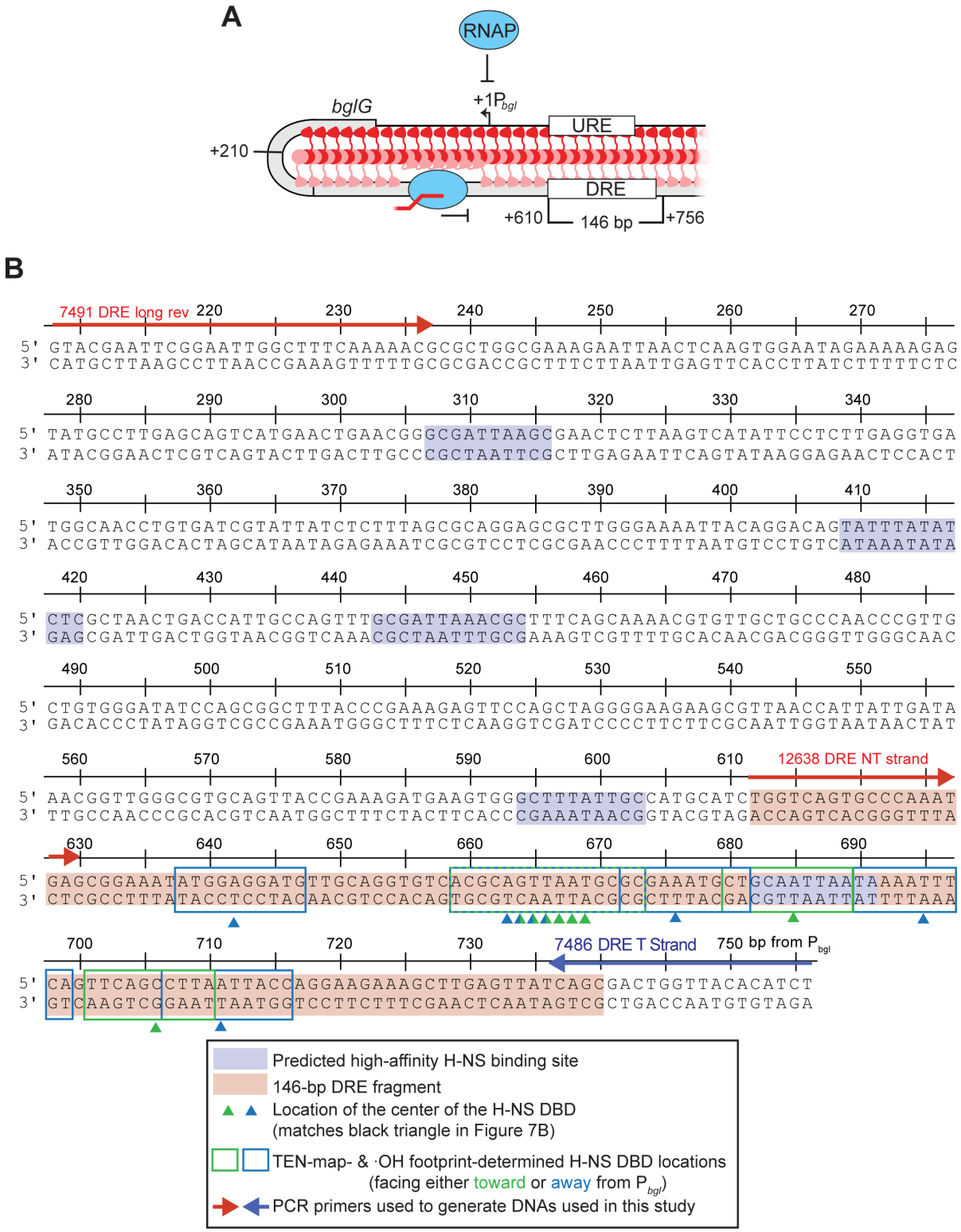

Figure S4-1. DNA sequence of the *bgl* operon region used for TEN-map experiments.

(A) At the *bgl* operon, an H-NS filament nucleates from both the downstream and upstream regulatory elements (DRE and URE; (Dole et al., 2004; Nagarajavel et al., 2007)), enabling formation of a bridged filament. A bridged filament occludes RNAP binding from the promoter

1308 and also can stimulate pausing by an elongating RNAP (Kotlajich et al., 2015; Rangarajan and
1309 Schnetz, 2018). Both mechanisms contribute to silencing of the *bgl* operon. (B) The 146-bp
1310 DNA fragment was generated by PCR using 5′ ^{32}P-end-labeled primers to label either the non-
1311 template (NT) strand (red, primer #12638) or the template (T) strand (blue, primer #7486).
1312 Longer fragments (549 bp) were amplified with primers #486 and #7491 and labeled on the T
1313 strand. The location of the DRE as identified by (Dole et al., 2004) is highlighted in light pink.
1314 High-affinity H-NS binding sites identified by Virtual Footprint
1315 (http://www.prodoric.de/vfp/vfp_regulon.php) are indicated by blue filled boxes. The sequence
1316 is numbered by distance from the TSS of P_{bgl}. Light blue and green open boxes highlight
1317 locations of H-NS DNA binding domains in ***Figure 7D***. Triangles indicate where the center of
1318 the H-NS DBD (see black arrow in ***Figure 7B***) was placed at that sequence either toward (green)
1319 or away (blue) from the *bgl* promoter (see ***Figure 8A***).

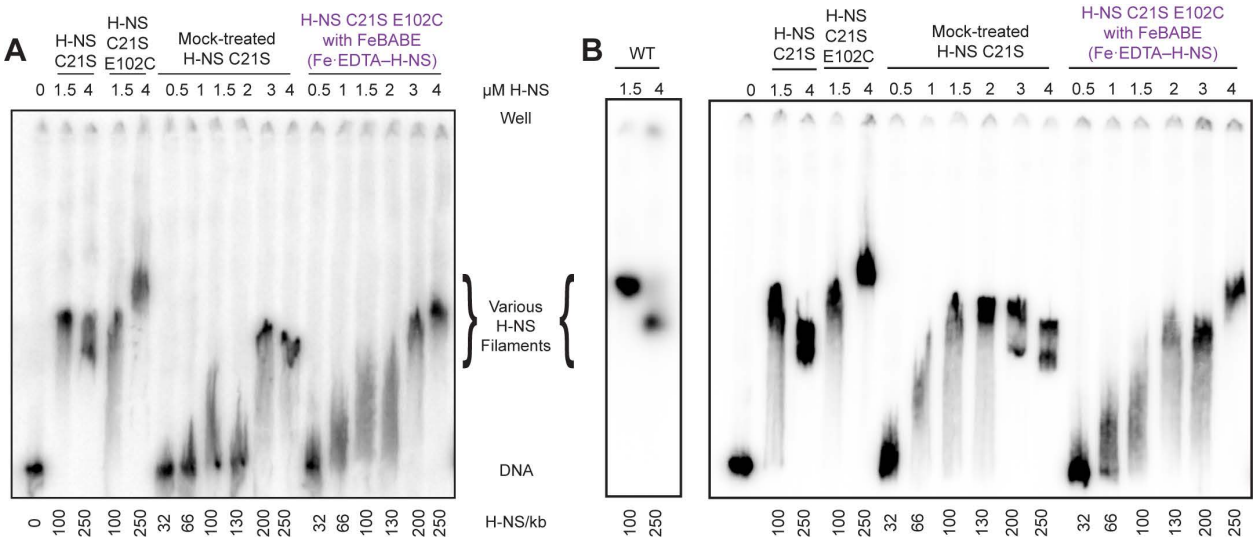

Figure S4-2. Fe·EDTA–H-NS forms filaments on *bgl* DRE DNA.

Electrophoretic mobility shift assay showing filament formation on 10 nM 1.5 kb DNA from the *bgl* operon (Boudreau et al., 2018; Kotlajich et al., 2015) by H-NS C21S or H-NS C21S E102C with or without FeBABE treatment. H-NS C21S (unable to conjugate) was treated with FeBABE to account for loss of activity during conjugation process. Fe·EDTA–H-NS contains FeBABE conjugated to ~50% of the E102C thiols in H-NS C21S E102C (see Methods). Panels A and B depict filament formation by two independent preparations of H-NS-FeBABE. Filaments formed were similar between preps, but the activity of H-NS varied between preparations. Panel (A) shows filament formation by sample one of conjugated H-NS and panel (B) shows filament formation by sample two of conjugated H-NS. All filaments were run on the same gel in (B), but rearranged for clarity.

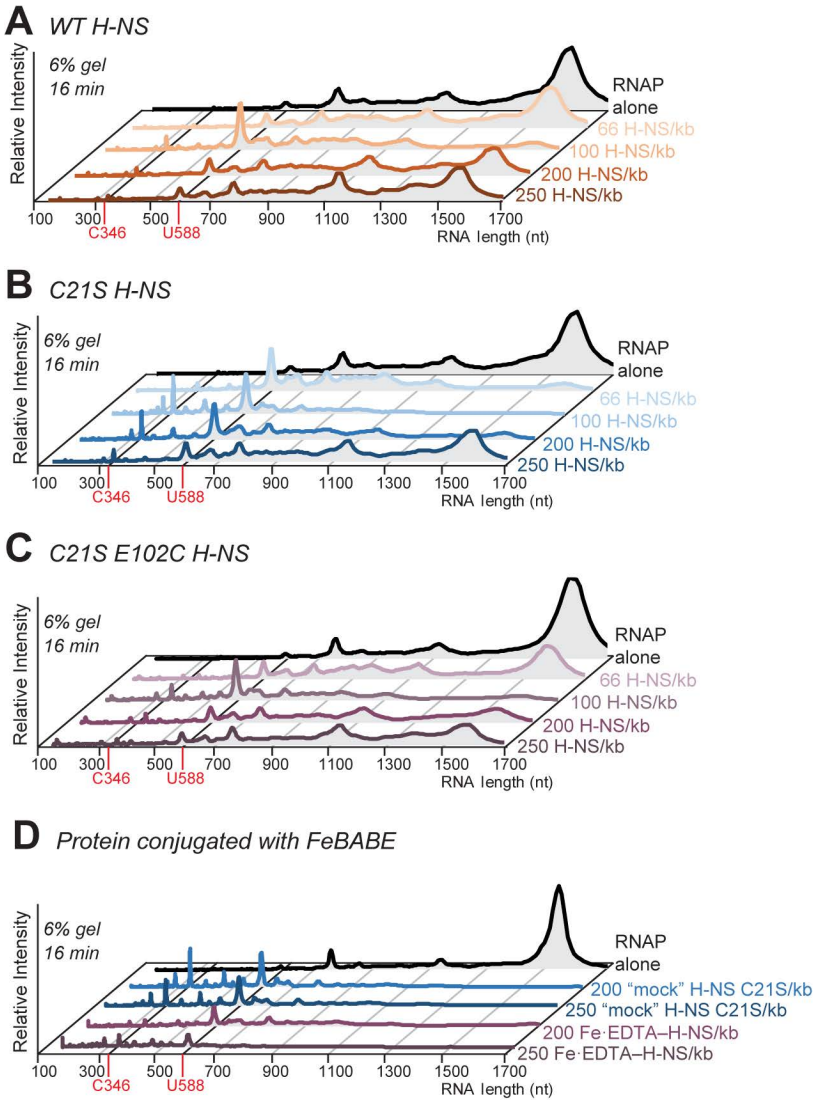

Figure S4-3. Effect of H-NS variants and FeBABE conjugation to H-NS on elongating RNAP.

Pseudo-densitometry traces show transcripts formed on a 1.5 kb bgl DNA by RNAP 16 min after transcription through various H-NS filaments is begun with 30 μM NTPs: (A) WT H-NS filaments, (B) C21S H-NS filaments, (C) C21S E102C H-NS filaments, (D) either C21S (blue; "mock"-treated) or C21S E102C (purple; Fe·EDTA–H-NS) H-NS that were treated with FeBABE. Concentrations of protein that formed filaments were used for transcription assays (see Figure S4-2).

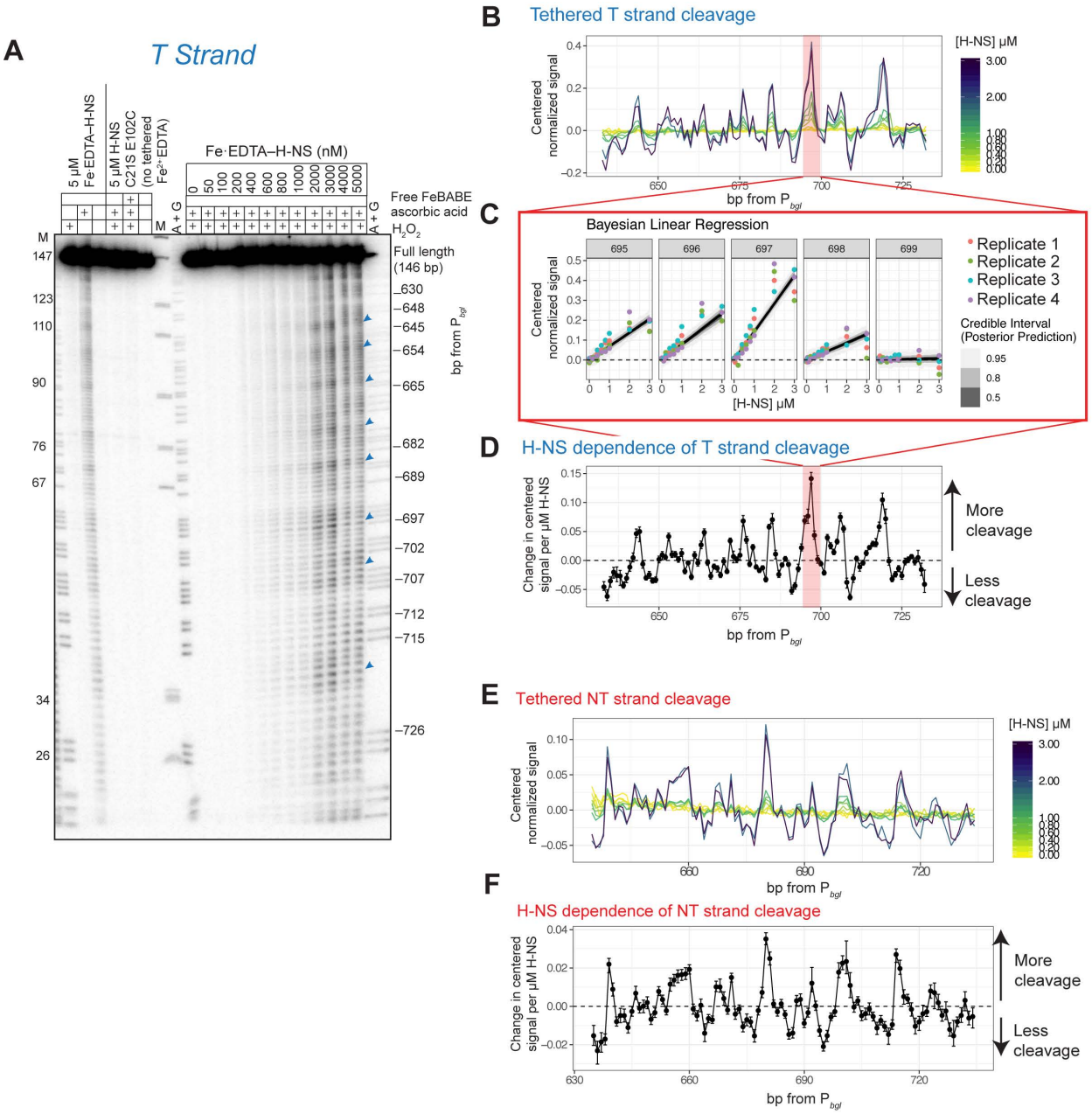

Figure S4-4. TEN-map analysis by linear regression of the Fe·EDTA–H-NS concentration-dependence of cleavage.
(A) Denaturing 7% PAG showing Fe·EDTA–H-NS cleavage pattern of 146-bp DRE DNA labeled on the T strand. Increasing concentrations of Fe·EDTA–H-NS were added to ~20 nM DNA. Cleavage was initiated with addition of 2 mM H_2O_2 and 2 mM ascorbic acid. Controls we performed with only 2 mM H_2O_2, 2 mM ascorbic acid, water in the presence of 5 μM Fe·EDTA–H-NS (far left lanes). Addition of free FeBABE to filaments formed with 5 μM H-NS C21S E102 that does not contain Fe·EDTA did not result in cleavage of the DNA (middle lanes). A+G indicates Maxam–Gilbert sequencing ladder. Blue arrows indicate hot spots of cleavage induced by Fe·EDTA–H-NS. SAFA peak area quantification from this gel are shown in ***Figure 4F***. (B) Cleavage of DRE DNA fragment T strand as a function of Fe·EDTA–H-NS concentration (yellow-to-purple gradient). Cleavage data were corrected for total signal in each lane and then normalized to the average peak area and centered on the mean. (C) The relationship between

1355 mean-centered normalized peak areas and the Fe·EDTA–H-NS concentration (from 0 to 3 μM)
1356 on the T strand was determined for each base pair by using a Bayesian linear regression model.
1357 The example shows linear regression model fits for positions 695-699 on the T strand. (D) H-NS
1358 dependence of cleavage of the T strand as determined from Bayesian linear regression model.
1359 Error bars indicate credible intervals on the slope estimates. (E) Same as B, but for the NT
1360 strand. (F) Same as D, but for the NT strand.
1361

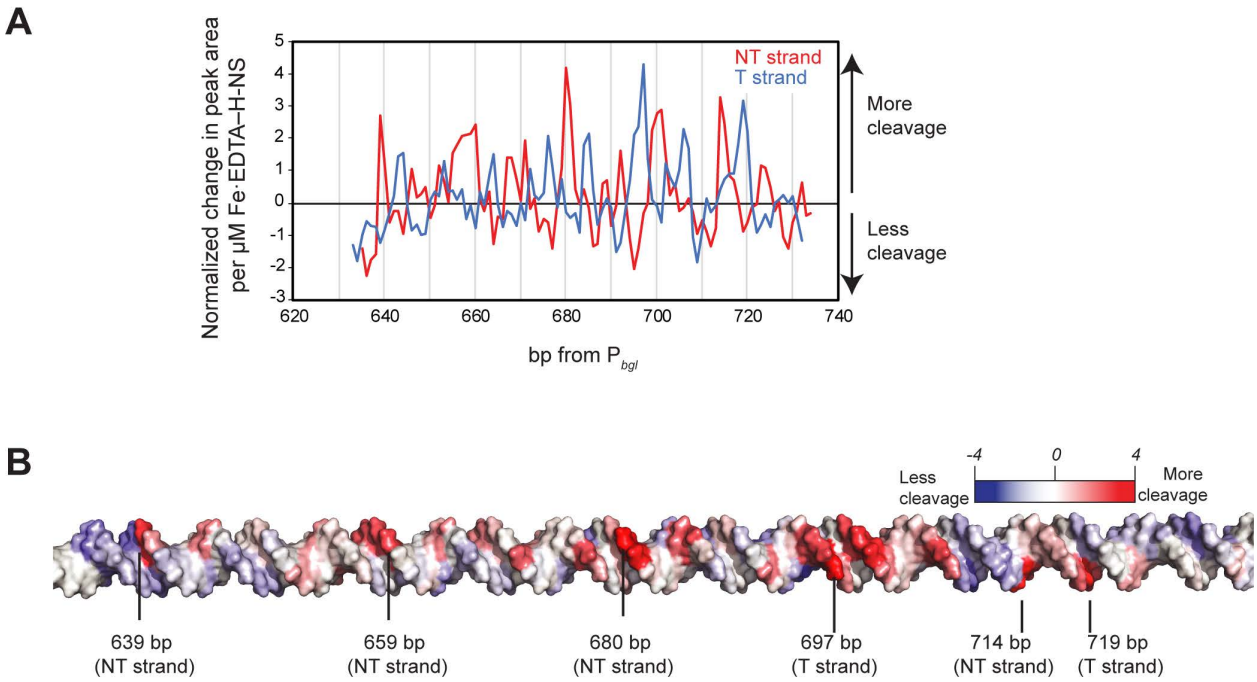

Figure S4–5. Use of linear regression-determined slopes to determine H-NS DBD locations. (A) Slope point-estimates (***Figure S4–4C*** *and* ***F***) were Robust-Z normalized within each strand for direct comparison between the strands (see Methods). More positive slopes indicate more H-NS dependent cleavage at that bp, indicating robust H-NS binding at the location. This Robust-Z normalized data was used to compare the TEN-map results and the Fe·EDTA–H-NS cleavage pattern predicted by MD simulation (***Figure 7***). (B) Data in (A) displayed on B-form DNA where red indicates the most-cut bases and blue are the least-cut bases.

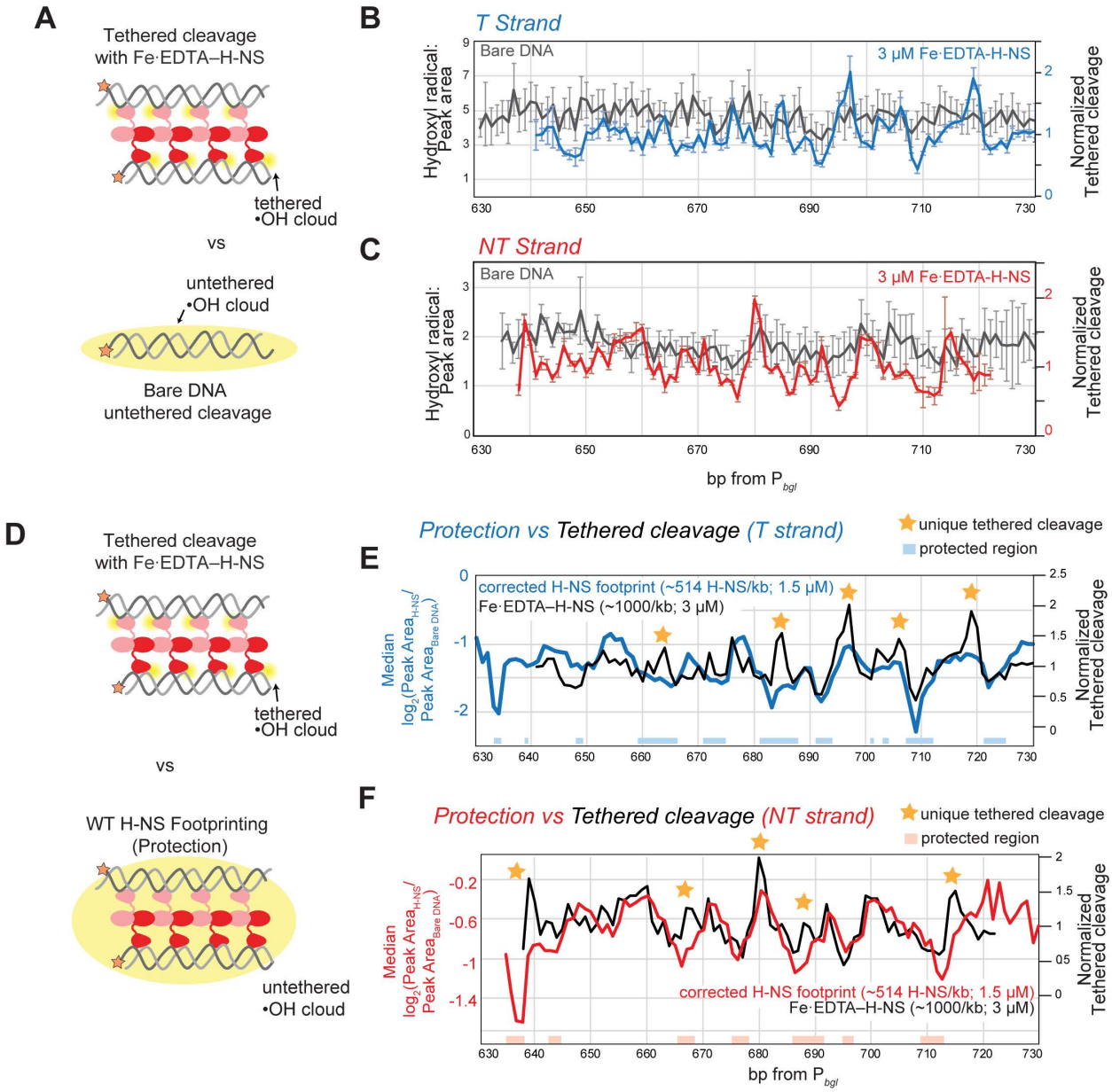

Figure S4–6. TEN-map cleavage patterns differ from freely diffusible ·OH cleavage of bare DNA and of DNA in the presence of wild-type H-NS.
(A) To verify that TEN-map cleavage reveals H-NS binding sites, the tethered cleavage pattern (top) was compared to ·OH cleavage of bare *bgl* DRE DNA (bottom). Yellow ovals represent the possible reach of ·OH cleavage in the assay. Peak area of ·OH cleavage of 146-bp *bgl* DRE DNA T (B) or NT (C) strand in the absence of H-NS (gray) shows intrinsic cleavage propensity of the sequence used to form H-NS filaments. The intrinsic cleavage pattern of bare DNA (gray) differed from the tethered cleavage pattern generated by 3 μM Fe·EDTA–H-NS on the T (blue) or NT (red) strand. The difference indicates specific cleavage by Fe·EDTA–H-NS. Error bars indicate standard deviation of three replicates. (D) Comparison of the TEN-map pattern (top) and the ·OH footprint (protection) pattern (bottom). Yellow ovals represent the possible reach of ·OH cleavage in the assay. (E) Blue line shows the ·OH footprints of wild-type H-NS on the T strand corrected by subtracting the bare DNA cleavage pattern from the pattern of ·OH cleavage of the T strand in the presence of wild-type H-NS (1.5 μM; Same trace as in ***Figure 6C***). Protected

1385 regions (valleys in protection pattern) calculated from concentration-dependent slope estimates
1386 are indicated by shaded boxes (see ***Figure S6–2***). Black line shows TEN-map cleavage by
1387 Fe·EDTA–H-NS (3 μM; 1027 H-NS/kb) demonstrating its distinct pattern, including cuts within
1388 H-NS footprints. The most notable cuts attributable to tethered Fe·EDTA are indicated by yellow
1389 stars. (F) Same as (E) but for the NT strand.
1390

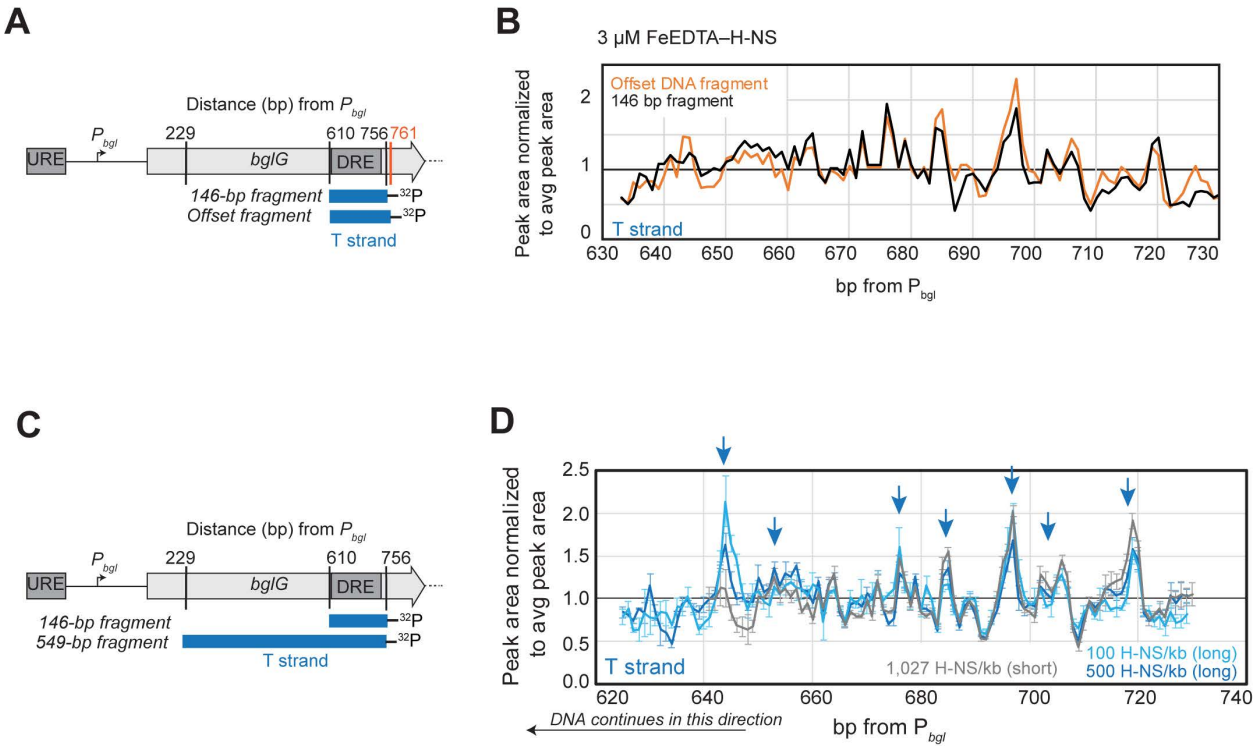

Figure S4-7. TEN-map cleavage is unaffected by flanking DNA context.
(A) Schematic of the DNA templates used to test if H-NS binding is sequence-specific or initiates from the end of the DNA. The 146-bp *bgl* DRE fragment (black arrow) was used in experiments shown in ***Figure 4***. An alternative PCR primer (orange line) was used to shift the DNA end by 5 bp relative to the standard 146-bp fragment. (B) TEN-map cleavage peak areas for the 146-bp fragment (black) and the 151-bp offset DNA fragment (orange). Cleavage and quantification were performed as described in Methods (averages from two experiments). (C) Comparison of the standard (146 bp) and long (549 bp) DNA fragments generated from the *bgl* operon to test effects of DNA length on arrangement of H-NS DBD within a filament. Both fragments were labeled on the T strand. (D) TEN-map cleavage patterns for standard (gray) or long (blue) DNAs. Gray line matches data in ***Figure 4F***. To form filaments on long DNA, H-NS a mixture of 60% wild-type H-NS and 40% Fe·EDTA–H-NS was used because the concentration of Fe·EDTA–H-NS alone was too low to form pure Fe·EDTA–H-NS filaments. Error bars show standard deviation of three replicates. Arrows indicate peaks of cleavage.

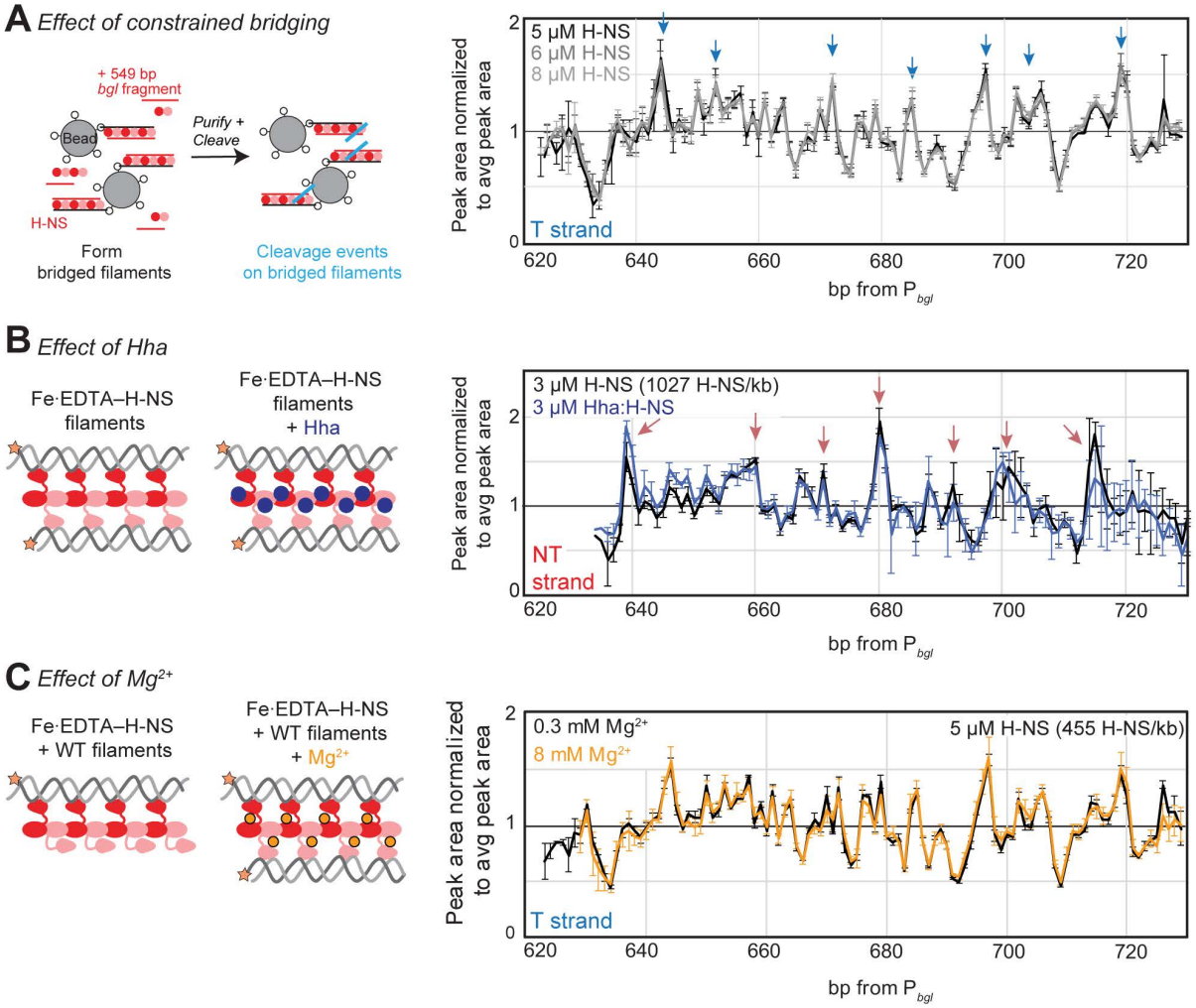

Figure 5. TEN-map cleavage of *bgl* DRE is unaffected by obligate bridging, Hha, or Mg^{2+} concentration.
(A) TEN-map cleavage of *bgl* DRE is unaffected by obligate bridging. Bridged filaments were formed by mixing unlabeled 685-bp DNA fragment bound to paramagnetic beads (see Methods), 549-bp *bgl* DNA labeled on the T strand, and H-NS (60% wild-type H-NS + 40% Fe·EDTA–H-NS) at the indicated concentrations. Bridged filaments were recovered by magnetic separation and resuspended in cleavage buffer to initiate cleavage of DNA (***Figure S5–2***; see Methods). TEN-map cleavage of a portion of the obligately bridged T strand is shown. (B) TEN-map cleavage of *bgl* DRE is unaffected by Hha. Formation of pure H-NS filament or an H-NS filament mixed with equimolar Hha (blue circle) was confirmed by EMSA and *in vitro* transcription assay (***Figure S5–3***). TEN-map cleavage of the *bgl* DRE NT in the presence (blue) or absence (black) of equimolar Hha. Red arrows indicate hotspots of cleavage, which are at the same locations for both H-NS and Hha:H-NS filaments. (C) TEN-map cleavage of *bgl* DRE is unaffected by Mg^{2+} concentration. TEN-map cleavage of T strand at 5 μM (455 H-NS/kb) in the presence 8 mM Mg^{2+} (orange) or 0.3 mM Mg^{2+} (black). Filaments were formed on 549 bp fragment from the *bgl* operon. H-NS was added at a 60-40 mixture of wild-type and Fe·EDTA–H-NS to match experiments done on beads in panel A. In all data panels, hotspots of TEN-map cleavage are indicated by arrows and error bars represent average of at least three replicates. Associated data: ***Figure S5–1***, ***Figure S5–2***, ***Figure S5–3***, and ***Figure S5–4.***

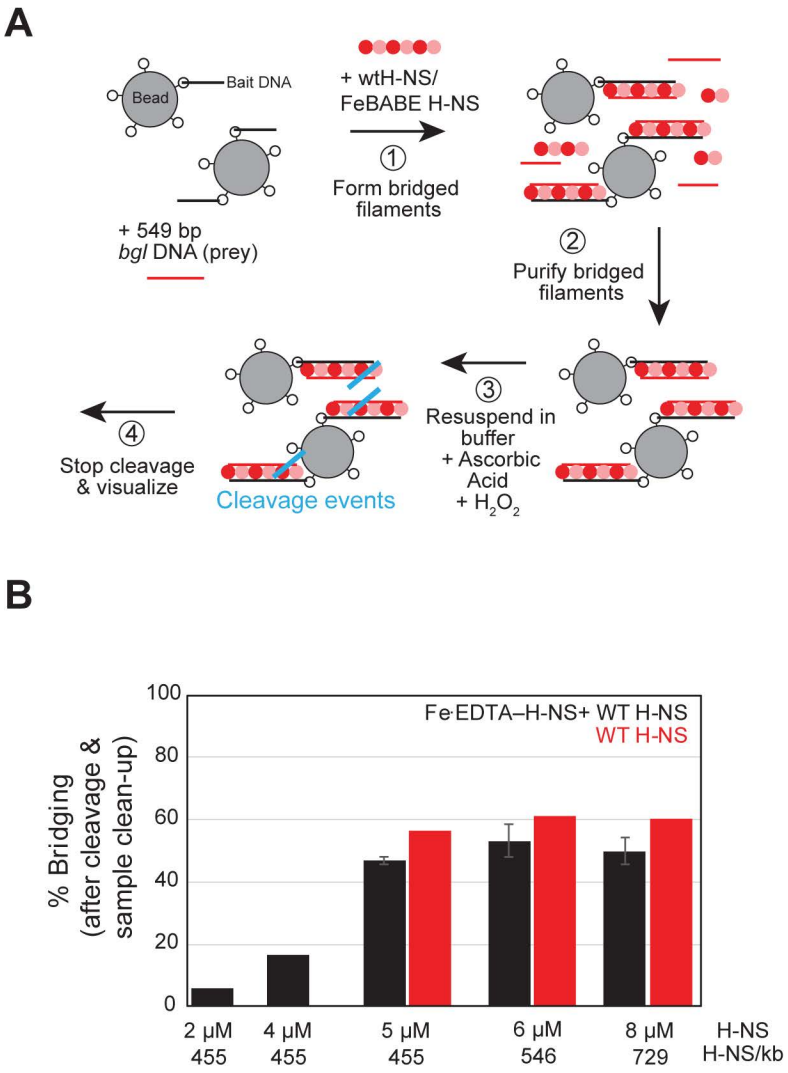

Figure S5–1. TEN-map cleavage of obligately bridged filaments formed on beads. (A) Set-up of bridged cleavage assay. Filaments were formed with a 60-40 mix of wild-type H-NS and Fe·EDTA–H-NS over a range of concentrations (5, 6 and 8 μM H-NS or 455, 546, and 729 H-NS/kb) in the presence of streptavidin paramagnetic beads containing immobilized 685-bp DNA (van der Valk et al., 2017). H-NS monomers (conjugated or wild-type) are shown as alternating pink and red spheres to indicate head–head, tail–tail dimerization. The 549-bp *bgl* DRE DNA (prey DNA) was not tethered to beads and was labeled on the T strand. Bridged filaments were recovered by magnetic separation and gently resuspended in 20 μL Filament Buffer (see Methods) followed by rapid addition of 1 μl 50 mM ascorbic acid and 4 μL 12.5 mM H_2O_2 to induce cleavage. Reactions were stopped with 22.4 mM thiourea, extracted with phenol, recovered by ethanol precipitation, and separated by denaturing 7% PAGE. (B) The percentage of prey DNA recovered by bridging in the presence of either wild-type H-NS (red) or a mixture of wild-type H-NS and Fe·EDTA–H-NS (black).

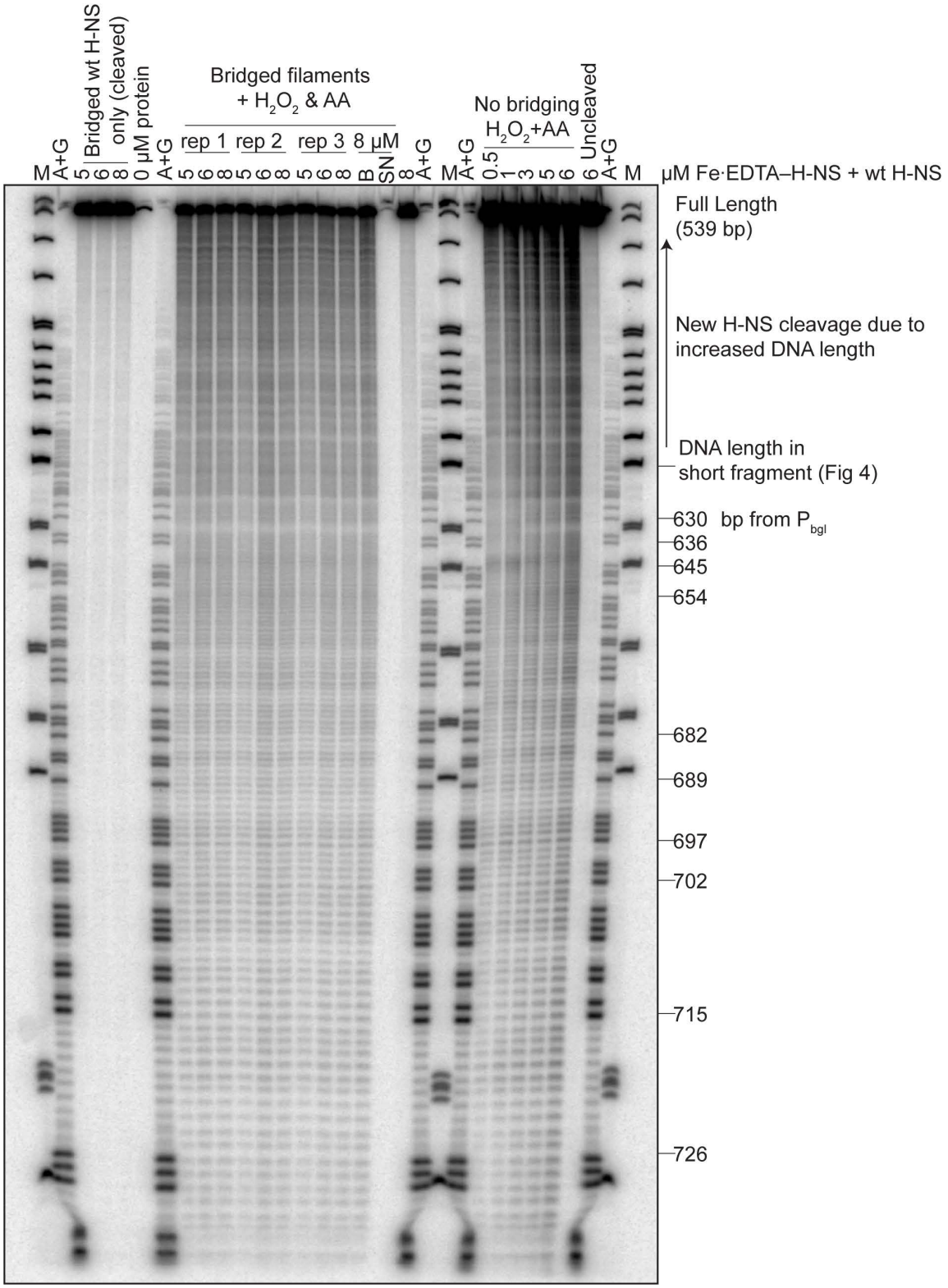

Figure S5–2. TEN-map cleavage of obligately bridged DNA versus in solution. Denaturing 7% PAG showing cleavage products generated by Fe·EDTA–H-NS in filaments formed on beads (obligately bridged filaments) or in solution (no obligate bridging). H-NS used to form filaments was 40% Fe·EDTA–H-NS and 60% wild-type H-NS at the indicated

1445 concentrations. 8 μM H-NS lanes marked “B” and “SN” indicate filaments formed with 8 μM H-
1446 NS, cleaved, and then magnetically separated into supernatant (SN), containing DNA that
1447 dissociated from the beads, and bound fractions (“B”, obligately bridged). Non-obligately
1448 bridging filaments were formed on the 545-bp *bgl* DNA without beads or bait DNA present at
1449 indicated concentrations of H-NS. A+G, Maxam–Gilbert A and G sequencing ladder. M, MspI
1450 digest pBR322.

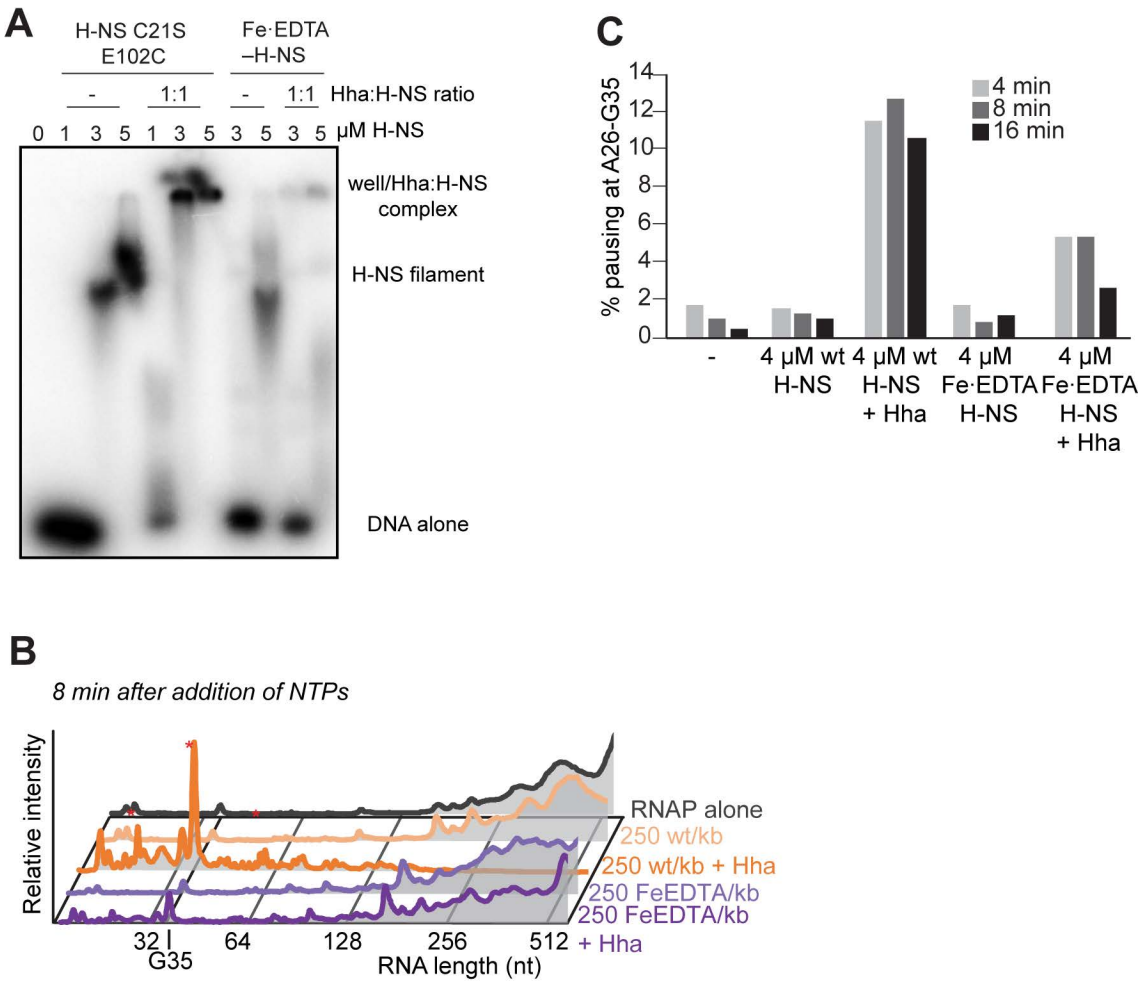

Figure S5–3. Properties of Hha:H-NS filaments formed with Fe·EDTA–H-NS.
(A) Native 3% PAG showing H-NS or Hha:H-NS filament formation on 146-bp DRE DNA. Amounts of H-NS C21S E102C or Fe·EDTA–H-NS were as indicated on the figure. Hha:H-NS filaments are retained in the well as previously observed (Boudreau et al., 2018). (B) Pseudo-densitometry plot showing transcripts produced by RNAP 8 min after addition of 30 μM NTPs in the presence of H-NS or Hha:H-NS filaments formed with wild-type or Fe·EDTA–H-NS. Pauses stimulated by Hha:H-NS are indicated with red asterisks. (C) Amount of pausing stimulated by H-NS and Hha:H-NS filaments. Hha added to both wild-type and Fe·EDTA–H-NS stimulated pausing at positions between A26 and G35 (Boudreau et al., 2018).

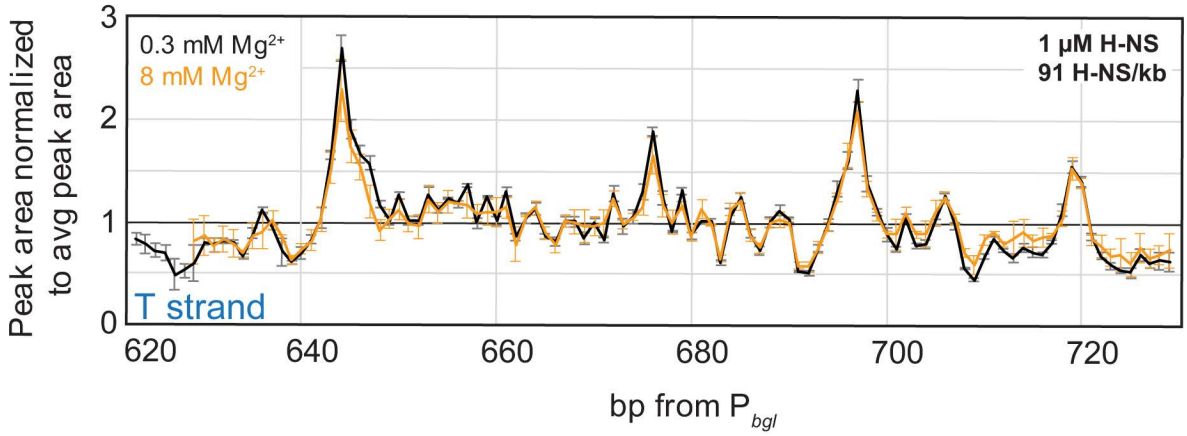

1461

1462 **Figure S5–4. H-NS DBDs bind DNA similarly at low and high Mg^{2+}.**
1463 TEN-map cleavage pattern of the *bgl* DRE 146-bp fragment (^{32}P-labeled T strand) at 1 μM H-NS
1464 (91 H-NS/kb) in the presence 8 mM Mg^{2+} (black) or 0.3 mM Mg^{2+} (orange). Filaments were
1465 formed on 549 bp fragment from the *bgl* operon labeled on the T strand. H-NS added was a 60-
1466 40 mixture of wild-type and Fe·EDTA–H-NS to match experiments done on beads (***Figure 5A***).
1467 Error bars represent the standard error of at least three replicates.

1468

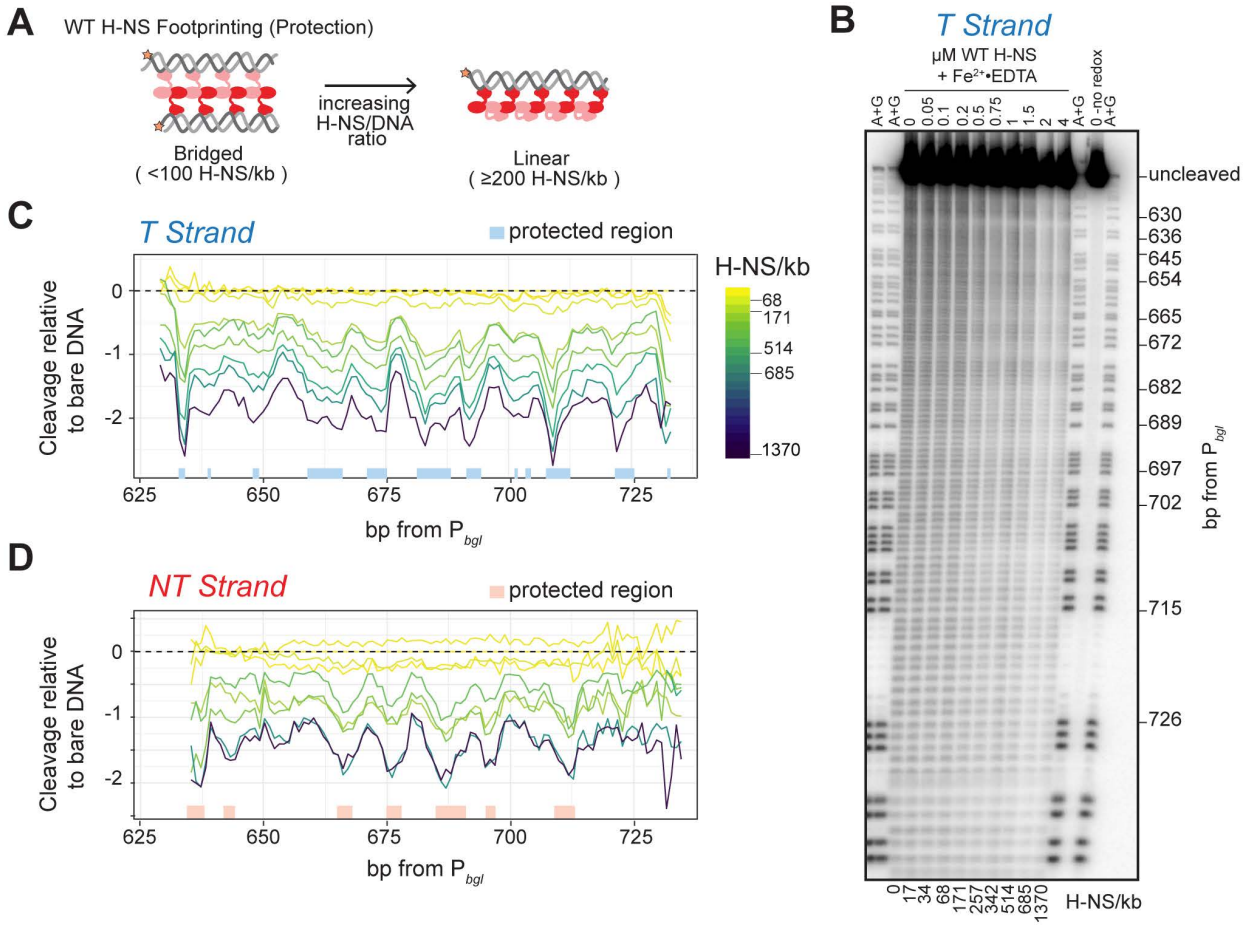

Figure 6. H-NS DBDs do not change locations during the switch of bridged-to-linear filaments as reported by ·OH footprinting.
(A) Schematic showing traditional ·OH footprinting with either bridged or linear H-NS filaments. In traditional footprinting, excess Fe^{2+}·EDTA is added in solution to create a pool of free radicals that diffuse freely so that any DNA not bound by wild-type H-NS will be cleaved (***Figure S4–6***). (B) Denaturing 7% PAG showing hydroxyl radical cleavage pattern of 146-bp *bgl* DRE DNA (^{32}P-labeled on the T strand) in the presence or absence of wild-type H-NS filaments formed at 0.05, 0.1, 0.2, 0.5, 0.75, 1, 1.5, 2, or 4 μM H-NS (17, 34, 68, 171, 251, 342, 514, 685, 1370 H-NS/kb). (C) The footprinting pattern on the T strand was quantified by normalizing the cleavage of DNA in the presence of H-NS to cleavage of bare DNA, and then log_2 transformed. Protected regions (shaded boxes) were assigned based on the positions exhibiting the greatest change in protection as a function of H-NS concentration (***Figure S6–1***). (D) Same as C, but for the NT strand. Lines represent the median of 4 experiments, but error bars are removed for clarity. Associated data: ***Figure S6–1*** and ***Figure S6–2***.

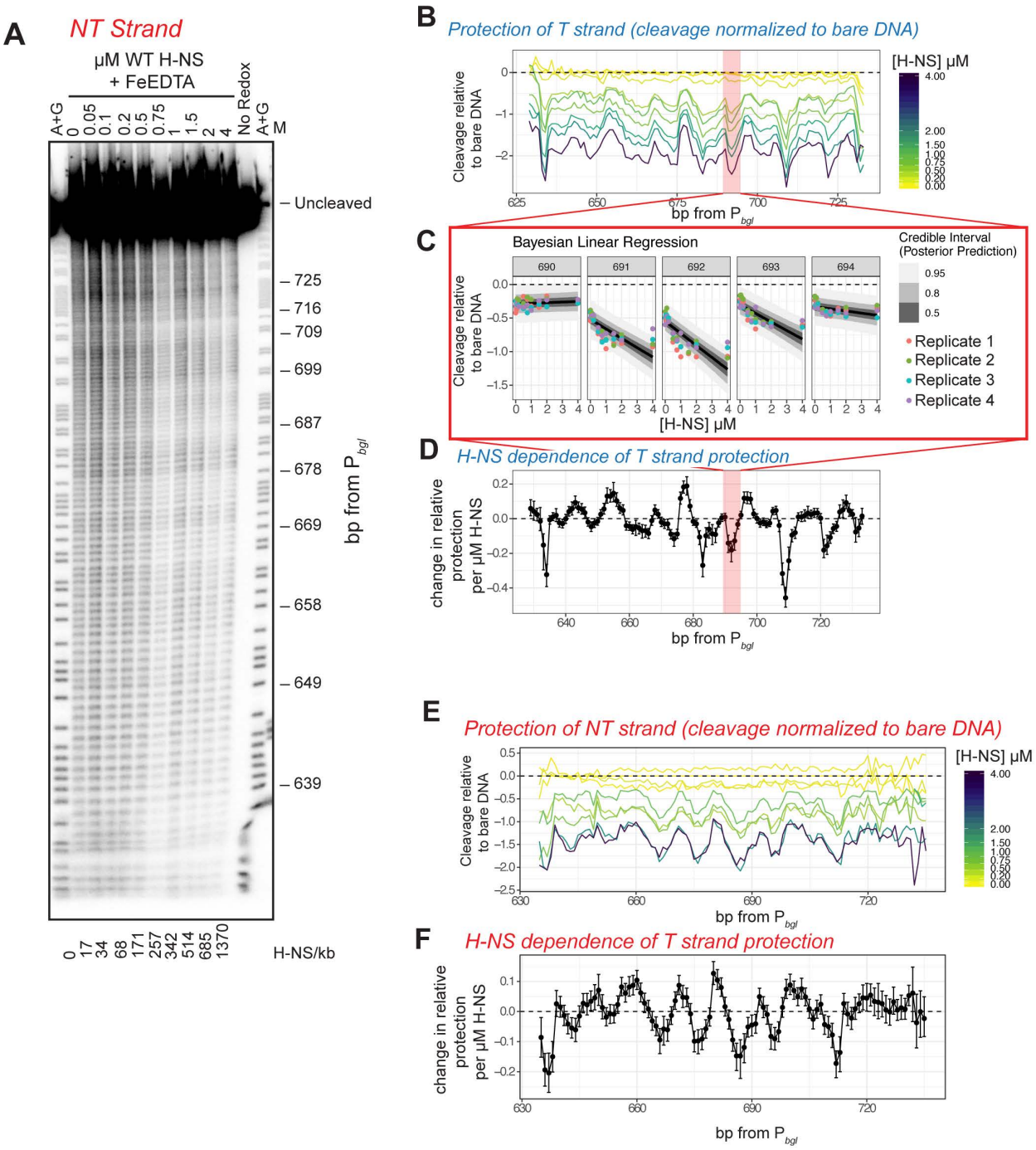

Figure S6-1. Analysis of ·OH footprinting of H-NS filaments using linear regression models.
(A) Denaturing 7% PAG showing hydroxyl radical cleavage pattern of 146-bp *bgl* DRE DNA (^{32}P-labeled on the NT strand) in the presence or absence of wild-type H-NS filaments formed at 0.05, 0.1, 0.2, 0.5, 0.75, 1, 1.5, 2, or 4 μM H-NS. The ratio of H-NS/kb is indicated below the gel. Wild-type H-NS plus untethered Fe·EDTA lanes were generated by sequential addition of H_2O_2, ascorbic acid, and Fe·EDTA. Gels are representative of at least 3 experiments. (B) Same as the data shown in ***Figure 6C***. The ·OH footprinting pattern for H-NS was quantified by calculating the change in cleavage of each position compared to cleavage of bare DNA and then $\log_2$ transformed. The median of 4 replicates was calculated, but error bars are removed for

1496 clarity. (C) For all positions, normalized peaks areas shown in (B) were plotted as a function of
1497 H-NS concentration. The change in peak area as a function of H-NS concentration (slope) was
1498 calculated using a Bayesian linear regression model. Example linear regression model fits shown
1499 for positions 690-694 on the T strand. (D) Change in protection relative to bare DNA as a
1500 function of H-NS concentration for the T strand. Error bars indicate 95% credible intervals on
1501 the slope estimates. (E) Same as B, but for the NT strand. Data also shown in Figure 6D. (F)
1502 Same as D, but for the NT strand.

1503

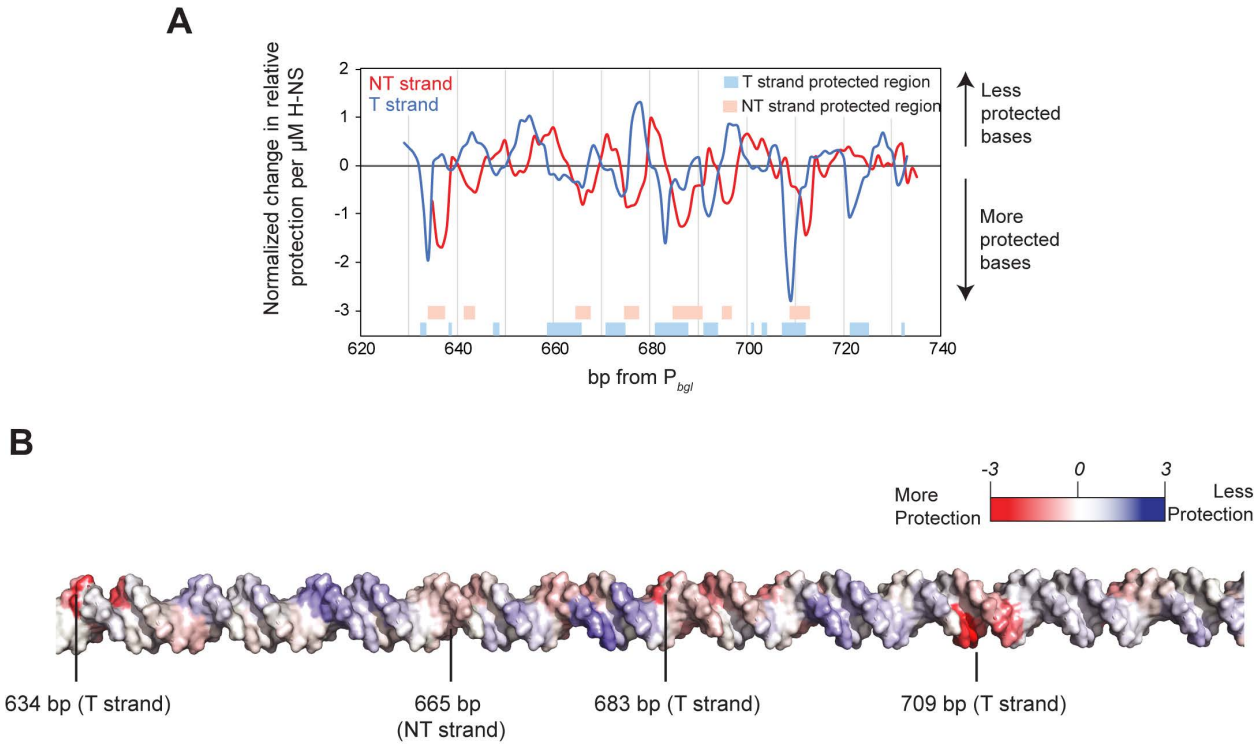

Figure S6–2. Sites of protection from ·OH cleavage by wild-type H-NS reveal DBD–DNA contacts in both bridged and linear filaments.
(A) Slope point-estimates (***Figure S6–1D*** *and* ***F***) were Robust-Z normalized within each strand for direct comparison between the strands (see Methods). More negative slopes indicate more H-NS dependent protection at that position and are interpreted to indicated stronger H-NS binding. The Robust-Z normalized data were used to compare the ·OH footprinting results and the modeled H-NS protection pattern (***Figure S7–2***). (B) Data in (A) displayed on B-form DNA where red indicates the most protected bases and blue are the least protected bases.

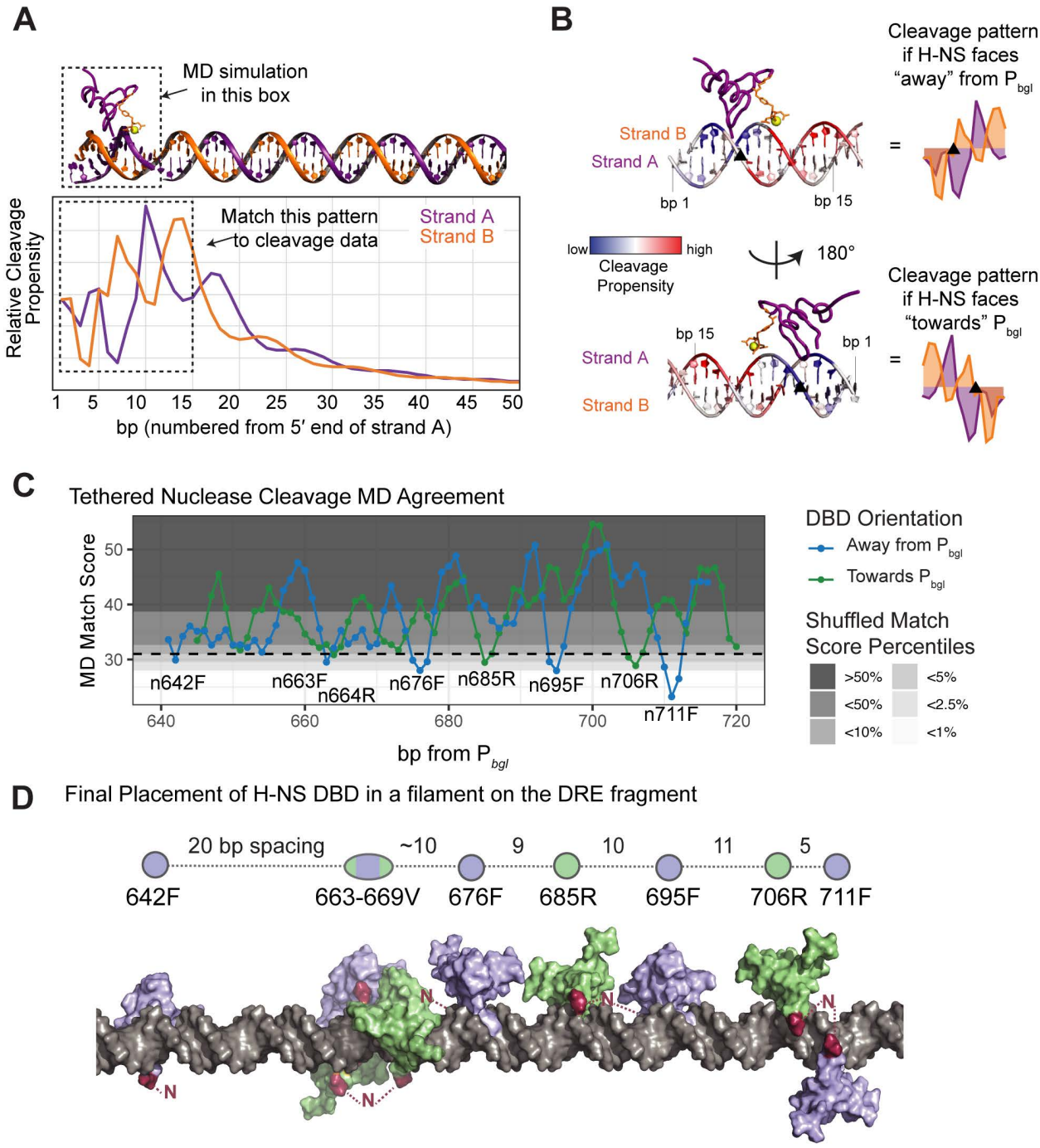

Figure 7. MD simulations of conjugated Fe·EDTA conformational dynamics
(A) MD simulation of Fe·EDTA (orange) conjugated to the H-NS DBD (purple) bound to a 12-bp DNA duplex (strand A, purple; strand B, orange). The distance between the Fe^{2+} and each bp during the simulation was used to estimate the cleavage propensity at each position. Additional DNA (bp 13-50) was included after the MD simulations to estimate cleavage propensities at bp further from the binding site. (B) Overlay of the cleavage propensity on B-form DNA with H-NS bound (PDB 2L93; (Riccardi et al., 2019). Cleavage propensity is on a blue-white-red spectrum where blue is low cleavage propensity and red is high cleavage propensity. Cleavage pattern of H-NS bound in the opposite orientation is also shown. (C) Concordance between expected and observed cleavage patterns as determined by the Manhattan distance (MD Match Score) between

1524 the pattern of predicted cleavage of the first 15 bp from the MD simulation and the tethered
1525 cleavage data of both strands (see Methods). Lower scores indicate greater concordance between
1526 the two patterns. The asymmetry of the MD simulation cleavage pattern enabled the
1527 determination of DBD orientation with respect to the P_{bgl} promoter as described in B. Statistical
1528 significance was determined by recalculating the Manhattan distance across 1000 shuffled
1529 tethered cleavage datasets for the MD cleavage pattern in each orientation. Shaded regions
1530 indicate values below the indicated percentiles of MD match scores across all shuffled datasets.
1531 The dotted line indicates a MD match score at <5% of all match scores determined in the
1532 shuffled datasets. The location (bp) and orientation (F or R for forward or reverse) of 8 H-NS
1533 binding sites predicted by TEN-map cleavage are indicated for each DBD. (D) A final model
1534 placing 7 H-NS DBDs on the DRE DNA was generated from TEN-map cleavage analysis and
1535 ·OH footprinting analysis (***Figure S7–2***; see Methods). DBDs were either in the forward (slate)
1536 or reverse (green). The spacing between each DBD is indicated on the 1D line graph above the
1537 3D model. The NTD (N) is not placed in our model but would be attached to the DBD at the
1538 dark red residues. Associated data: ***Figure S7–1*** and ***Figure S7–2***.

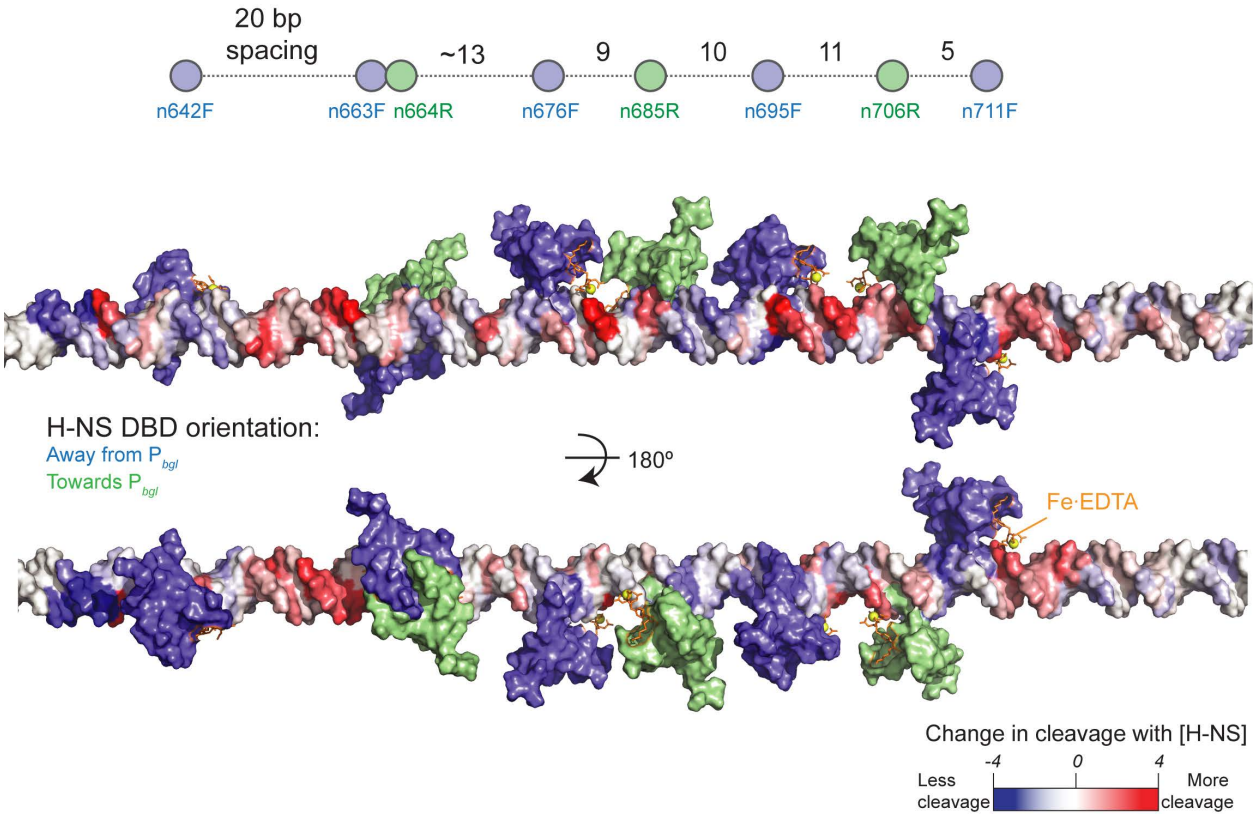

Figure S7–1. Modeling of H-NS DBD location based on match score between TEN-map cleavage pattern and MD simulation.
The center of the H-NS DBD (slate or green) with the Fe·EDTA tether (orange sticks and yellow sphere, Fe^{2+}) was placed on B-form DNA at the position with the best match score in ***Figure 7C***. The prediction method (n for TEN-map cleavage), position on the DNA (bp from P_{bgl}), and the orientation (F or R) are indicated for each DBD. DNA is colored as in ***Figure S4-5B***. Two views of DBD binding model are shown. Spacing between DBD indicated on 1D line plot at the top as in Figure 7.

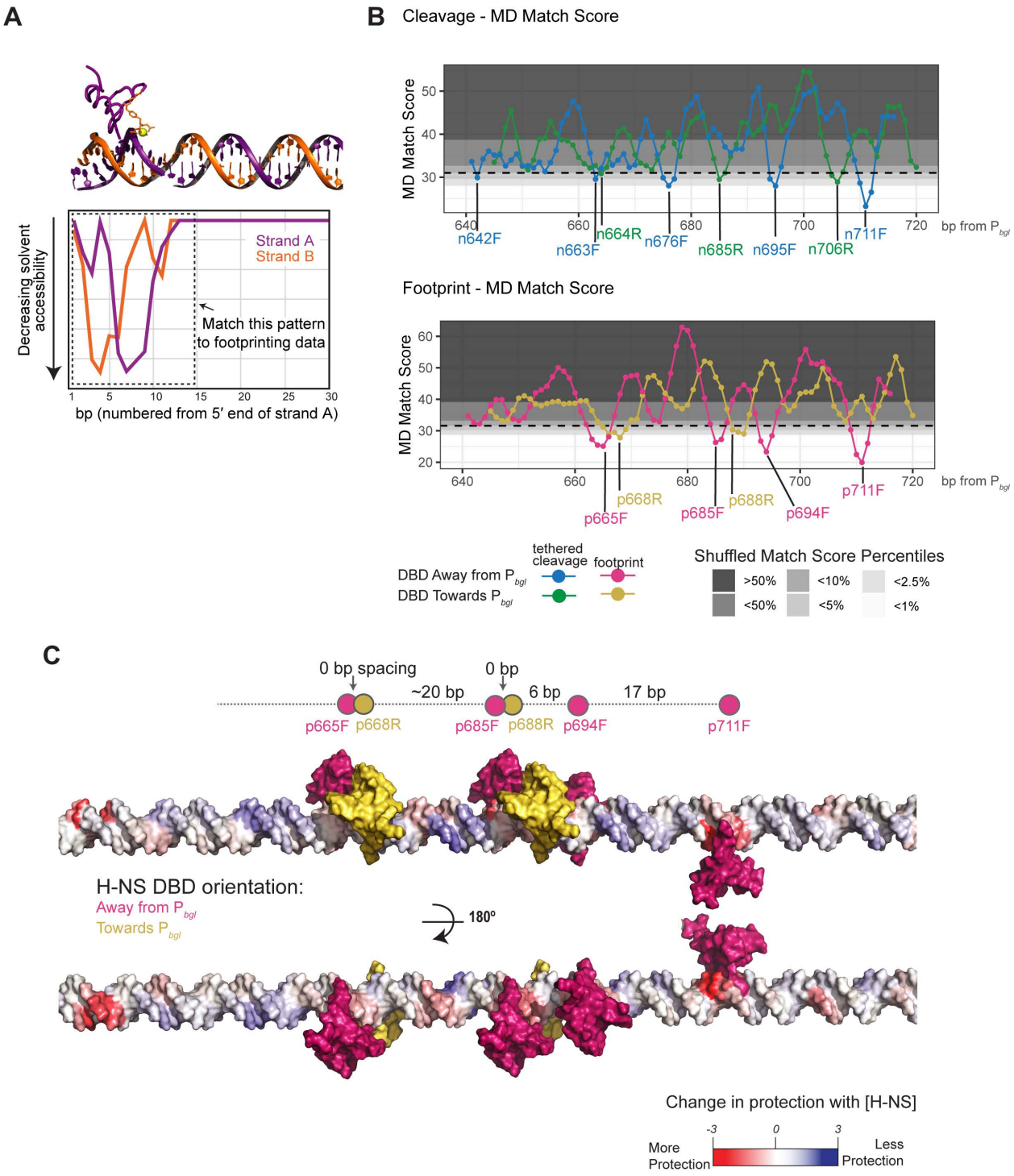

Figure S7–2. Modeling of H-NS DBD location based on ·OH footprinting and solvent accessibility patterns.
(A) Solvent accessibility of DNA bound by one H-ND DBD calculated from structure shown at the top. A 15-bp portion of this pattern was compared to the ·OH footprinting pattern (dashed box). (B) *Top:* repeat of data in ***Figure 7C*** so match scores from ·OH footprinting pattern can be compared to the TEN-map match scores. *Bottom:* Concordance between expected and observed protection patterns as determined by the Manhattan distance (MD Match Score) between the

1556 pattern of predicted protection of the first 15 bp from the MD simulation (A) and the ·OH radical
1557 footprinting data of both strands (***Figure 6***; see Methods). Lower scores indicate greater
1558 concordance between the two patterns. The asymmetry of the MD simulation cleavage pattern
1559 enabled the determination of DBD orientation with respect to the P_{bgl} promoter with the forward
1560 binding cleavage pattern indicating "Away from P_{bgl}" (pink trace) and the reverse binding
1561 cleavage indicating "Towards P_{bgl}" (golden trace). Statistical significance was determined by
1562 recalculating the Manhattan distance across 1000 shuffled ·OH footprinting datasets for the MD
1563 protection pattern in each orientation. Shaded regions indicate values below the indicated
1564 percentiles of MD match scores across all shuffled datasets. The dotted line indicates a MD
1565 match score at <5% of all match scores determined in the shuffled datasets. (C) The center of the
1566 H-NS DBD (gold or pink) was placed on B-form DNA at the position with the best match score
1567 in (B). The prediction method (p for footprint), position on the DNA (bp from P_{bgl}), and the
1568 orientation (F or R) are indicated for each DBD. Spacing between DBD indicated on 1D line plot
1569 at the top as in Figure 7. Note that there is overlap between the two DBDs at 665 and 668 and the
1570 two DBDs at 685 and 688, suggesting that only one H-NS is bound in either of those 3 bp
1571 regions. DNA is colored as in ***Figure S6-2***.

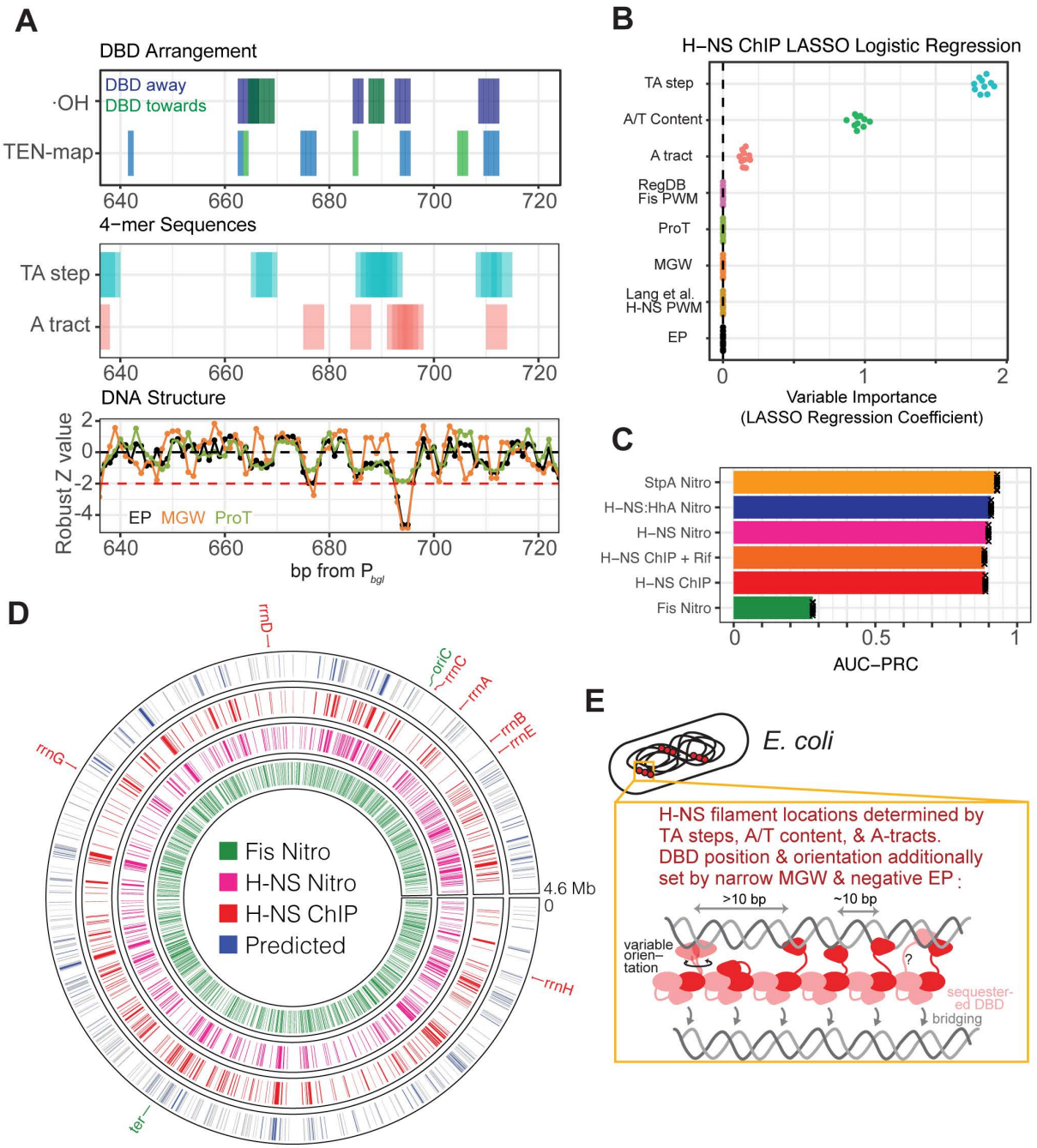

Figure 8. DNA sequence dictates H-NS DBD arrangement within filaments and H-NS filament location genome-wide.
(A) Summary of *in vitro* analysis of a single H-NS filament and association with DNA sequence and sequence-based structural features. (Top) Regions of high confidence DBD binding and orientation determined from concordance between predicted and observed TEN-map patterns (see ***Figure 7***) as well as predicted and observed DNA protection under ·OH radical footprinting (see ***Figure S7–2***). Each bar indicates regions where match scores between expected and observed patterns are below 95% of match scores obtained with 1000 shuffled datasets with each

1581 orientation of the DBD (see Methods). Blue bars indicate a DBD orientation away from P_{bgl}
1582 whereas green bars indicate a DBD orientation towards P_{bgl}. (Middle) Location of 4mers
1583 consistent with a TA step or an A-tract (see Methods for definitions) within the DRE sequence.
1584 (Bottom) Overlay of predicted minor groove width (MGW, orange), propeller twist (ProT,
1585 green), and electrostatic potential in the minor groove (EP, black) across the DRE sequence. The
1586 values were Robust-Z scaled and centered using the genome-wide median and MAD (see
1587 Methods). The black dotted line indicates the genome-wide median whereas the red dotted line
1588 indicates the –2 cutoff used to determine regions with substantially lower values for that feature.
1589 (B) Determination of a minimal set of features to predict regions of H-NS binding across the
1590 genome. Final coefficients from a LASSO logistic regression model trained on the H-NS ChIP
1591 data using the bound status of 1000 bp windows tiled every 250 bp across the genome are
1592 displayed with each point representing values determined from one of ten trained models using
1593 10-fold cross validation with stratified sampling (see Methods). (C) Performance of models
1594 trained on predicting bound regions for each genome-wide dataset (from panel B). Each bar
1595 displays the average area under a precision recall curve (AUC-PRC) from the 10 replicates of
1596 models trained on stratified subsampled data (x indicates each replicate). (D) Circular plot (Gu et
1597 al., 2014) displaying the predicted genome-wide H-NS binding sites as determined by a LASSO
1598 logistic regression model trained on the full H-NS ChIP-seq data set and only considering
1599 windows with a predicted probability > 0.95 (blue) or between 0.5 and 0.95 (black) of being
1600 bound by H-NS as bound regions. For comparison, MOSAiCS determined peaks are shown for
1601 H-NS ChIP (red), H-NS Nitro-seq (pink), and Fis Nitro-seq (green). (E) DNA sequence and
1602 structure determine global and local H-NS filament arrangement. In *E. coli*, H-NS filaments form
1603 genome-wide at sequences with TA steps, A-tracts, and are AT-rich. Within each filament, most
1604 DBDs adopt an arrangement with ~10 bp spacing between DBDs; however, some DBDs are
1605 more flexible and adopt different orientations or bind with small variations in the ~10 bp spacing
1606 along the DNA. The arrangement of H-NS coincides with DNA shape and sequence motif
1607 parameters. Our results indicate the same arrangement of the DBD in both bridged or linear
1608 filaments, which is best explained by the hemi-sequestration model in which one DBD in an H-
1609 NS dimer is sequestered by interactions with the NTD in a linear filament but is able to bind
1610 DNA with ~10 bp spacing in a bridged filament (see Discussion). Associated data: ***Figure S8–1***.

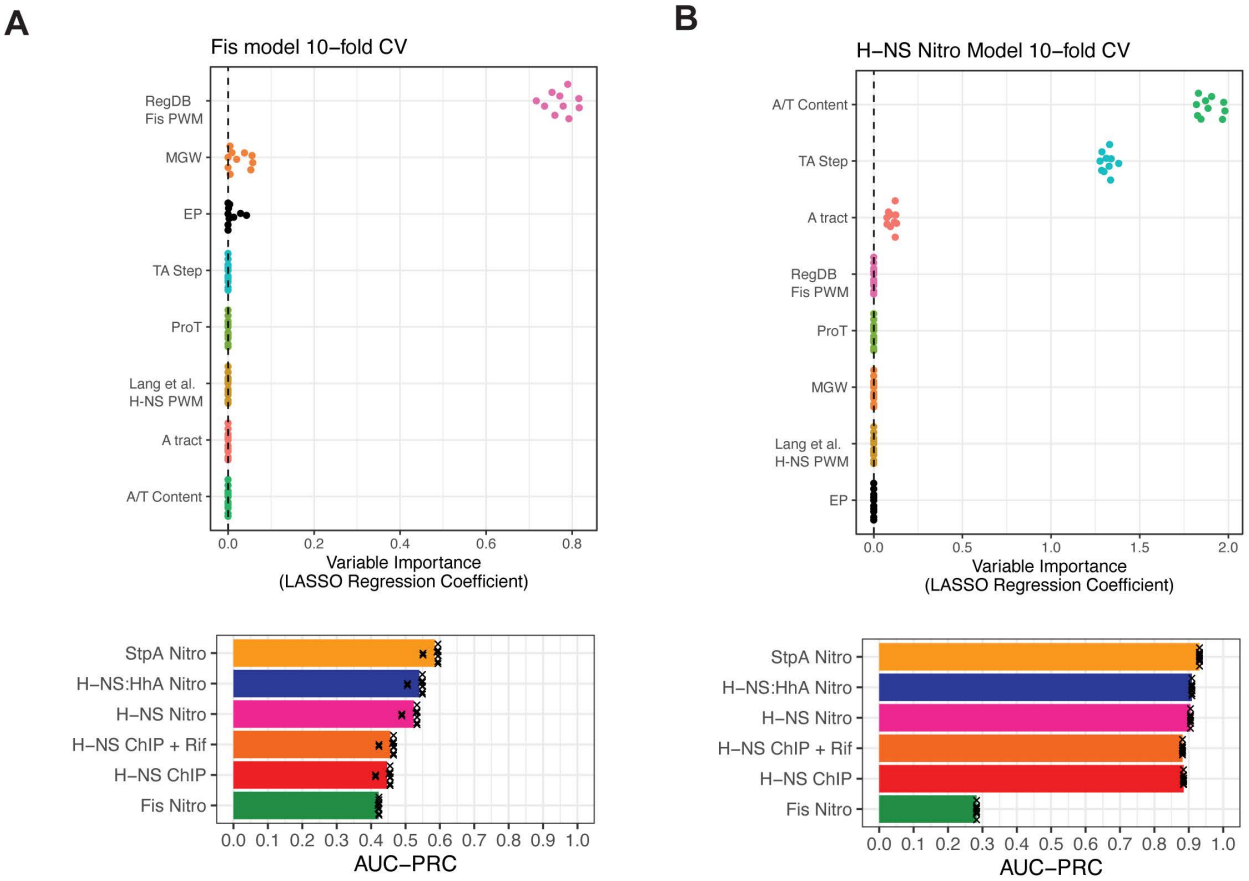

Figure S8–1. LASSO analysis based on H-NS Nitro-seq data also predicts *in vivo* H-NS binding pattern, but Fis does not.
(A) Determination of a minimal set of features to predict regions of H-NS binding across the genome using LASSO model trained on the Fis Nitro-seq data (see Methods). Performance of model on predicting bound regions in various genome-wide data sets. Each bar displays the average area under a precision recall curve (AUC-PRC) from the 10 replicates of models trained on stratified subsampled data (x indicates each replicate). (B) As in A, but LASSO model trained on H-NS Nitro-seq data used to predict binding throughout the genome.

1621 **REFERENCES**

1622 Ali, S.S., Whitney, J.C., Stevenson, J., Robinson, H., Howell, P.L., and Navarre, W.W. 2013.
1623 Structural insights into the regulation of foreign genes in Salmonella by the Hha/H-NS
1624 complex. *J Biol Chem* **288**: 13356-13369. doi: 10.1074/jbc.M113.455378.

1625 Amit, R., Oppenheim, A.B., and Stavans, J. 2003. Increased bending rigidity of single DNA
1626 molecules by H-NS, a temperature and osmolarity sensor. *Biophys. J.* **84**: 2467-2473. doi:
1627 10.1016/S0006-3495(03)75051-6.

1628 Andrews, S. (2010). FastQC: a quality control tool for high throughput sequence data. .
1629 (http://www.bioinformatics.babraham.ac.uk/projects/fastqc, Babraham Bioinformatics)

1630 Arold, S.T., Leonard, P.G., Parkinson, G.N., and Ladbury, J.E. 2010. H-NS forms a superhelical
1631 protein scaffold for DNA condensation. *PNAS* **107**: 15728-15732. doi:
1632 10.1073/pnas.1006966107.

1633 Baba, T., Ara, T., Hasegawa, M., Takai, Y., Okumura, Y., Baba, M., Datsenko, K.A., Tomita, M.,
1634 Wanner, B.L., and Mori, H. 2006. Construction of Escherichia coli K-12 in-frame, single-gene
1635 knockout mutants: the Keio collection. *Mol Syst Biol* **2**: 2006 0008. doi: 10.1038/msb4100050.

1636 Badaut, C., Williams, R., Arluison, V., Bouffartigues, E., Robert, B., Buc, H., and Rimsky, S.
1637 2002. The Degree of Oligomerization of the H-NS Nucleoid Structuring Protein Is Related to
1638 Specific Binding to DNA. *J. Biol. Chem.* **277**: 41657-41666. doi: 10.1074/jbc.M206037200.

1639 Balasubramanian, B., Pogozelski, W.K., and Tullis, T.D. 1998. DNA strand breaking by the
1640 hydroxyl radical is governed by the accessible surface area of the hydrogen atoms of the DNA
1641 backbone. *Proc. Natl. Acad. Sci. USA* **95**: 9738-9743. doi: 10.1073/pnas.95.17.9738.

1642 Banos, R.C., Vivero, A., Aznar, S., Garcia, J., Pons, M., Madrid, C., and Juarez, A. 2009.
1643 Differential regulation of horizontally acquired and core genome genes by the bacterial
1644 modulator H-NS. *PLoS Genet.* **5**: e1000513. doi: 10.1371/journal.pgen.1000513.

1645 Best, R.B., Zhu, X., Shim, J., Lopes, P.E.M., Mittal, J., Feig, M., and MacKerell, A.D. 2012.
1646 Optimization of the Additive CHARMM All-Atom Protein Force Field Targeting Improved
1647 Sampling of the Backbone phi, psi and Side-Chain chi(1) and chi(2) Dihedral Angles. *Journal*
1648 *of Chemical Theory and Computation* **8**: 3257-3273. doi: 10.1021/ct300400x.

1649 Bolger, A.M., Lohse, M., and Usadel, B. 2014. Trimmomatic: a flexible trimmer for Illumina
1650 sequence data. *Bioinformatics* **30**: 2114-2120. doi: 10.1093/bioinformatics/btu170 %J
1651 Bioinformatics.

1652 Boudreau, B.A., Hron, D.R., Qin, L., van der Valk, R.A., Kotlajich, M.V., Dame, R.T., and
1653 Landick, R. 2018. StpA and Hha stimulate pausing by RNA polymerase by promoting DNA-
1654 DNA bridging of H-NS filaments. *Nucleic acids research* **46**: 5525-5546. doi:
1655 10.1093/nar/gky265.

1656 Bouffartigues, E., Buckle, M., Badaut, C., Travers, A., and Rimsky, S. 2007. H-NS cooperative
1657 binding to high-affinity sites in a regulatory element results in transcriptional silencing. *Nat.*
1658 *Struct. Mol. Biol.* **14**: 441-448. doi: 10.1038/nsmb1233.

1659 Brooks, B.R., Brooks, C.L., Mackerell, A.D., Nilsson, L., Petrella, R.J., Roux, B., Won, Y.,
1660 Archontis, G., Bartels, C., Boresch, S.*, et al.* 2009. CHARMM: The Biomolecular Simulation
1661 Program. *J. Comput. Chem.* **30**: 1545-1614. doi: 10.1002/Jcc.21287.

1662 Burkhoff, A.M., and Tullis, T.D. 1988. Structural details of an adenine tract that does not cause
1663 DNA to bend. *Nature* **331**: 455-457. doi: 10.1038/331455a0.

1664 Bürkner, P.-C. 2017. brms: An R Package for Bayesian Multilevel Models Using Stan. *Journal of*
1665 *Statistical Software* **80** doi: 10.18637/jss.v080.i01.

1666 Campbell, E.A., Korzheva, N., Mustaev, A., Murakami, K., Nair, S., Goldfarb, A., and Darst, S.A.
1667 2001. Structural mechanism for rifampicin inhibition of bacterial RNA polymerase. *Cell* **104**:
1668 901-912. doi: 10.1016/s0092-8674(01)00286-0.

1669 Chandraprakash, D., and Seshasayee, A.S.N. 2014. Inhibition of factor-dependent transcription
1670 termination in Escherichia coli might relieve xenogene silencing by abrogating H-NS-DNA
1671 interactions in vivo. *J. Biosci. (Bangalore)* **39**: 53-61. doi: 10.1007/s12038-014-9413-4.

1672 Cheal, S.M., Ng, M., Barrios, B., Miao, Z., Kalani, A.K., and Meares, C.F. 2009. Mapping
1673 protein-protein interactions by localized oxidation: consequences of the reach of hydroxyl
1674 radical. *Biochemistry* **48**: 4577-4586. doi: 10.1021/bi900273j.

1675 Chiu, T.-P., Rao, S., Mann, R.S., Honig, B., and Rohs, R. 2017. Genome-wide prediction of
1676 minor-groove electrostatic potential enables biophysical modeling of protein–DNA binding.
1677 *Nucleic Acids Res.* **45**: 12565-12576. doi: 10.1093/nar/gkx915.

1678 Chiu, T.P., Comoglio, F., Zhou, T., Yang, L., Paro, R., and Rohs, R. 2016. DNAshapeR: an
1679 R/Bioconductor package for DNA shape prediction and feature encoding. *Bioinformatics* **32**:
1680 1211-1213. doi: 10.1093/bioinformatics/btv735.

1681 Cho, B.K., Knight, E.M., Barrett, C.L., and Palsson, B.O. 2008. Genome-wide analysis of Fis
1682 binding in Escherichia coli indicates a causative role for A-/AT-tracts. *Genome Res.* **18**: 900-
1683 910. doi: 10.1101/gr.070276.107.

1684 Chung, D., Zhang, Q., and Keles, S. (2014). MOSAiCS-HMM: A model-based approach for
1685 detecting regions of histone modifications from ChIP-seq data. In Statistical Analysis of Next
1686 Generation Sequencing Data, S. Data, and D. Nettleton, eds. (Springer).

1687 Cook, P.R., and Marenduzzo, D. 2018. Transcription-driven genome organization: a model for
1688 chromosome structure and the regulation of gene expression tested through simulations.
1689 *Nucleic Acids Res.* **46**: 9895-9906. doi: 10.1093/nar/gky763.

1690 Dame, R.T., Noom, M.C., and Wuite, G.J. 2006. Bacterial chromatin organization by H-NS
1691 protein unravelled using dual DNA manipulation. *Nature* **444**: 387-390. doi:
1692 10.1038/nature05283.

1693 Dame, R.T., Rashid, F.M., and Grainger, D.C. 2020. Chromosome organization in bacteria:
1694 mechanistic insights into genome structure and function. *Nat. Rev. Genet.* doi:
1695 10.1038/s41576-019-0185-4.

1696 Das, R., Laederach, A., Pearlman, S.M., Herschlag, D., and Altman, R.B. 2005. SAFA: semi-
1697 automated footprinting analysis software for high-throughput quantification of nucleic acid
1698 footprinting experiments. *RNA* **11**: 344-354. doi: 10.1261/rna.7214405.

1699 Davis, J., and Goadrich, M. (2006). The relationship between Precision-Recall and ROC curves.
1700 In Proceedings of the 23rd international conference on Machine learning (Pittsburgh,
1701 Pennsylvania, USA, Association for Computing Machinery), pp. 233–
1702 240^10.1145/1143844.1143874.

1703 Dole, S., Nagarajavel, V., and Schnetz, K. 2004. The histone-like nucleoid structuring protein H-
1704 NS represses the Escherichia coli bgl operon downstream of the promoter. *Mol Microbiol* **52**:
1705 589-600. doi: 10.1111/j.1365-2958.2004.04001.x.

1706 Eastman, P., Swails, J., Chodera, J.D., McGibbon, R.T., Zhao, Y.T., Beauchamp, K.A., Wang,
1707 L.P., Simmonett, A.C., Harrigan, M.P., Stern, C.D.*, et al.* 2017. OpenMM 7: Rapid
1708 development of high performance algorithms for molecular dynamics. *PLoS Comp. Biol.* **13**:
1709 17. doi: 10.1371/journal.pcbi.1005659.

1710 Favorov, A., Mularoni, L., Cope, L.M., Medvedeva, Y., Mironov, A.A., Makeev, V.J., and
1711 Wheelan, S.J. 2012. Exploring Massive, Genome Scale Datasets with the GenometriCorr
1712 Package. *PLoS Comp. Biol.* **8**: e1002529. doi: 10.1371/journal.pcbi.1002529.

1713 Friedman, J.H., Hastie, T., and Tibshirani, R. 2010. Regularization Paths for Generalized Linear
1714 Models via Coordinate Descent. *2010* **33**: 22 %J Journal of Statistical Software. doi:
1715 10.18637/jss.v033.i01.

1716 Fukui, N., Oshima, T., Ueda, T., Ogasawara, N., and Tobe, T. 2016. Gene Activation through the
1717 Modulation of Nucleoid Structures by a Horizontally Transferred Regulator, Pch, in
1718 Enterohemorrhagic Escherichia coli. *PLoS One* **11**: e0149718. doi:
1719 10.1371/journal.pone.0149718.

1720 Gao, Y., Foo, Y.H., Winardhi, R.S., Tang, Q., Yan, J., and Kenney, L.J. 2017. Charged residues
1721 in the H-NS linker drive DNA binding and gene silencing in single cells. *Proc Natl Acad Sci*
1722 *USA* **114**: 12560-12565. doi: 10.1073/pnas.1716721114.

1723 Gawade, P., Gunjal, G., Sharma, A., and Ghosh, P. 2020. Reconstruction of transcriptional
1724 regulatory networks of Fis and H-NS in Escherichia coli from genome-wide data analysis.
1725 *Genomics* **112**: 1264-1272. doi: https://doi.org/10.1016/j.ygeno.2019.07.013.

1726 Ghosh, I.N., and Landick, R. 2016. OptSSeq: High-Throughput Sequencing Readout of Growth
1727 Enrichment Defines Optimal Gene Expression Elements for Homoethanologenesis. *ACS Synth*
1728 *Biol* **5**: 1519-1534. doi: 10.1021/acssynbio.6b00121.

1729 Gordon, B.R., Li, Y., Cote, A., Weirauch, M.T., Ding, P., Hughes, T.R., Navarre, W.W., Xia, B.,
1730 and Liu, J. 2011. Structural basis for recognition of AT-rich DNA by unrelated xenogeneic
1731 silencing proteins. *Proc Natl Acad Sci USA* **108**: 10690-10695. doi: 10.1073/pnas.1102544108.

1732 Grainger, D.C. 2016. Structure and function of bacterial H-NS protein. *Biochem. Soc. Trans.* **44**:
1733 1561-1569. doi: 10.1042/BST20160190.

1734 Grainger, D.C., Goldberg, M.D., Lee, D.J., and Busby, S.J. 2008. Selective repression by Fis and
1735 H-NS at the Escherichia coli dps promoter. *Mol Microbiol* **68**: 1366-1377. doi: 10.1111/j.1365-
1736 2958.2008.06253.x.

1737 Grainger, D.C., Hurd, D., Goldberg, M.D., and Busby, S.J. 2006. Association of nucleoid proteins
1738 with coding and non-coding segments of the Escherichia coli genome. *Nucleic acids research*
1739 **34**: 4642-4652. doi: 10.1093/nar/gkl542.

1740 Grant, C.E., Bailey, T.L., and Noble, W.S. 2011. FIMO: scanning for occurrences of a given
1741 motif. *Bioinformatics* **27**: 1017-1018. doi: 10.1093/bioinformatics/btr064.

1742 Grau, J., Grosse, I., and Keilwagen, J. 2015. PRROC: computing and visualizing precision-recall
1743 and receiver operating characteristic curves in R. *Bioinformatics* **31**: 2595-2597. doi:
1744 10.1093/bioinformatics/btv153 %J Bioinformatics.

1745 Greiner, D.P., Miyake, R., Moran, J.K., Jones, A.D., Negishi, T., Ishihama, A., and Meares, C.F.
1746 1997. Synthesis of the protein cutting reagent Iron (*S*)-1-(*p*-
1747 Bromoacetamidobenzyl)ethylenediaminetetraacetate and conjugation to cysteine side chains.
1748 *Bioconj. Chem.* **8**: 44-48. doi: 10.1021/bc9600731.

1749 Gu, Z., Gu, L., Eils, R., Schlesner, M., and Brors, B. 2014. circlize implements and enhances
1750 circular visualization in R. *Bioinformatics* **30**: 2811-2812. doi: 10.1093/bioinformatics/btu393
1751 %J Bioinformatics.

1752 Gulvady, R., Gao, Y., Kenney, L.J., and Yan, J. 2018. A single molecule analysis of H-NS
1753 uncouples DNA binding affinity from DNA specificity. *Nucleic acids research* **46**: 10216-
1754 10224. doi: 10.1093/nar/gky826.

1755 Hampel, F.R. 1974. The Influence Curve and its Role in Robust Estimation. *Journal of the*
1756 *American Statistical Association* **69**: 383-393. doi: 10.1080/01621459.1974.10482962.

1757 Hart, K., Foloppe, N., Baker, C.M., Denning, E.J., Nilsson, L., and MacKerell, A.D. 2012.
1758 Optimization of the CHARMM Additive Force Field for DNA: Improved Treatment of the
1759 BI/BII Conformational Equilibrium. *Journal of Chemical Theory and Computation* **8**: 348-362.
1760 doi: 10.1021/ct200723y.

1761 Herring, C.D., Raffaelle, M., Allen, T.E., Kanin, E.I., Landick, R., Ansari, A.Z., and Palsson,
1762 B.O. 2005. Immobilization of Escherichia coli RNA polymerase and location of binding sites

1763 by use of chromatin immunoprecipitation and microarrays. *J Bacteriol* **187**: 6166-6174. doi:
1764 10.1128/JB.187.17.6166-6174.2005.

1765 Japaridze, A., Renevey, S., Sobetzko, P., Stoliar, L., Nasser, W., Dietler, G., and Muskhelishvili,
1766 G. 2017. Spatial organization of DNA sequences directs the assembly of bacterial chromatin by
1767 a nucleoid-associated protein. *J Biol Chem* **292**: 7607-7618. doi: 10.1074/jbc.M117.780239.

1768 Kahramanoglou, C., Seshasayee, A.S., Prieto, A.I., Ibberson, D., Schmidt, S., Zimmermann, J.,
1769 Benes, V., Fraser, G.M., and Luscombe, N.M. 2011. Direct and indirect effects of H-NS and
1770 Fis on global gene expression control in Escherichia coli. *Nucleic Acids Res* **39**: 2073-2091.
1771 doi: 10.1093/nar/gkq934.

1772 Kim, D., Hong, J.S., Qiu, Y., Nagarajan, H., Seo, J.H., Cho, B.K., Tsai, S.F., and Palsson, B.O.
1773 2012. Comparative analysis of regulatory elements between Escherichia coli and Klebsiella
1774 pneumoniae by genome-wide transcription start site profiling. *PLoS Genet.* **8**: e1002867. doi:
1775 10.1371/journal.pgen.1002867.

1776 Kotlajich, M.V., Hron, D.R., Boudreau, B.A., Sun, Z., Lyubchenko, Y.L., and Landick, R. 2015.
1777 Bridged filaments of histone-like nucleoid structuring protein pause RNA polymerase and aid
1778 termination in bacteria. *Elife* **4** doi: 10.7554/eLife.04970.

1779 Krietenstein, N., Wal, M., Watanabe, S., Park, B., Peterson, C.L., Pugh, B.F., and Korber, P.
1780 2016. Genomic Nucleosome Organization Reconstituted with Pure Proteins. *Cell* **167**: 709-721
1781 e712. doi: 10.1016/j.cell.2016.09.045.

1782 Kuan, P.F., Chung, D., Pan, G., Thomson, J.A., Stewart, R., and Keles, S. 2011. A Statistical
1783 Framework for the Analysis of ChIP-Seq Data. *J Am Stat Assoc* **106**: 891-903. doi:
1784 10.1198/jasa.2011.ap09706.

1785 Lang, B., Blot, N., Bouffartigues, E., Buckle, M., Geertz, M., Gualerzi, C.O., Mavathur, R.,
1786 Muskhelishvili, G., Pon, C.L., Rimsky, S.*, et al.* 2007. High-affinity DNA binding sites for H-

1787 NS provide a molecular basis for selective silencing within proteobacterial genomes. *Nucleic*
1788 *Acids Res* **35**: 6330-6337. doi: 10.1093/nar/gkm712.

1789 Langmead, B., and Salzberg, S.L. 2012. Fast gapped-read alignment with Bowtie 2. *Nat. Methods*
1790 **9**: 357-359. doi: 10.1038/nmeth.1923.

1791 Leonard, P.G., Ono, S., Gor, J., Perkins, S.J., and Ladbury, J.E. 2009. Investigation of the self-
1792 association and hetero-association interactions of H-NS and StpA from Enterobacteria. *Mol*
1793 *Microbiol* **73**: 165-179. doi: 10.1111/j.1365-2958.2009.06754.x.

1794 Li, H., Handsaker, B., Wysoker, A., Fennell, T., Ruan, J., Homer, N., Marth, G., Abecasis, G.,
1795 Durbin, R., and Subgroup, G.P.D.P. 2009. The Sequence Alignment/Map format and
1796 SAMtools. *Bioinformatics* **25**: 2078-2079. doi: 10.1093/bioinformatics/btp352 %J
1797 Bioinformatics.

1798 Liao, Q.H., Pabis, A., Strodel, B., and Kamerlin, S.C.L. 2017. Extending the Nonbonded Cationic
1799 Dummy Model to Account for Ion-Induced Dipole Interactions. *Journal of Physical Chemistry*
1800 *Letters* **8**: 5408-5414. doi: 10.1021/acs.jpclett.7b02358.

1801 Lim, C.J., Lee, S.Y., Kenney, L.J., and Yan, J. 2012. Nucleoprotein filament formation is the
1802 structural basis for bacterial protein H-NS gene silencing. *Sci Rep* **2**: 509. doi:
1803 10.1038/srep00509.

1804 Liu, Y., Chen, H., Kenney, L.J., and Yan, J. 2010. A divalent switch drives H-NS/DNA-binding
1805 conformations between stiffening and bridging modes. *Genes Dev* **24**: 339-344. doi:
1806 10.1101/gad.1883510.

1807 Lucchini, S., McDermott, P., Thompson, A., and Hinton, J.C. 2009. The H-NS-like protein StpA
1808 represses the RpoS (sigma 38) regulon during exponential growth of Salmonella Typhimurium.
1809 *Mol Microbiol* **74**: 1169-1186. doi: 10.1111/j.1365-2958.2009.06929.x.

1810 Lucchini, S., Rowley, G., Goldberg, M.D., Hurd, D., Harrison, M., and Hinton, J.C. 2006. H-NS
1811 mediates the silencing of laterally acquired genes in bacteria. *PLoS Pathog* **2**: e81. doi:
1812 10.1371/journal.ppat.0020081.

1813 Luger, K., Mader, A.W., Richmond, R.K., Sargent, D.F., and Richmond, T.J. 1997. Crystal
1814 structure of the nucleosome core particle at 2.8 Å resolution. *Nature* **389**: 251-260. doi:
1815 10.1038/38444.

1816 Maxam, A.M., and Gilbert, W. 1977. A new method for sequencing DNA. *Proc. Natl. Acad. Sci.*
1817 *USA* **74**: 560-564. doi: 10.1073/pnas.74.2.560.

1818 Mooney, R.A., Davis, S.E., Peters, J.M., Rowland, J.L., Ansari, A.Z., and Landick, R. 2009.
1819 Regulator trafficking on bacterial transcription units in vivo. *Mol Cell* **33**: 97-108. doi:
1820 10.1016/j.molcel.2008.12.021.

1821 Muller, C.M., Dobrindt, U., Nagy, G., Emody, L., Uhlin, B.E., and Hacker, J. 2006. Role of
1822 histone-like proteins H-NS and StpA in expression of virulence determinants of uropathogenic
1823 Escherichia coli. *J Bacteriol* **188**: 5428-5438. doi: 10.1128/JB.01956-05.

1824 Myers, K.S., Yan, H., Ong, I.M., Chung, D., Liang, K., Tran, F., Keles, S., Landick, R., and
1825 Kiley, P.J. 2013. Genome-scale analysis of escherichia coli FNR reveals complex features of
1826 transcription factor binding. *PLoS Genet.* **9**: e1003565. doi: 10.1371/journal.pgen.1003565.

1827 Nagarajavel, V., Madhusudan, S., Dole, S., Rahmouni, A.R., and Schnetz, K. 2007. Repression by
1828 binding of H-NS within the transcription unit. *J Biol Chem* **282**: 23622-23630. doi:
1829 10.1074/jbc.M702753200.

1830 Navarre, W.W., Porwollik, S., Wang, Y., McClelland, M., Rosen, H., Libby, S.J., and Fang, F.C.
1831 2006. Selective silencing of foreign DNA with low GC content by the H-NS protein in
1832 Salmonella. *Science* **313**: 236-238. doi: 10.1126/science.1128794.

1833 Neidhardt, F.C., Bloch, P.L., and Smith, D.F. 1974. Culture Medium for Enterobacteria. **119**:
1834 736-747. doi:

1835 Nieto, J.M., Madrid, C., Prenafeta, A., Miquelay, E., Balsalobre, C., Carrascal, M., and Juarez, A.
1836 2000. Expression of the hemolysin operon in *Escherichia coli* is modulated by a nucleoid-
1837 protein complex that includes the proteins Hha and H-NS. *Mol. Genet. Genomics* **263**: 349-
1838 358. doi: 10.1007/s004380051178.

1839 Noom, M.C., Navarre, W.W., Oshima, T., Wuite, G.J., and Dame, R.T. 2007. H-NS promotes
1840 looped domain formation in the bacterial chromosome. *Current biology : CB* **17**: R913-914.
1841 doi: 10.1016/j.cub.2007.09.005.

1842 Owen-Hughes, T., Pavitt, G., Santos, D., Sidebotham, J., Hulton, C., Hinton, J., and Higgins, C.
1843 1992. The chromatin-associated protein H-NS interacts with curved DNA to influence DNA
1844 topology and gene expression. . *Cell* **71**: 255-265. doi: 10.1002/j.1460-2075.1994.tb06256.x.

1845 Papoulas, O. 1996. Rapid Separation of Protein-Bound DNA from Free DNA Using
1846 Nitrocellulose Filters. *Curr Protoc Mol Biol*: 12.18.11-12.18.19. doi:
1847 10.1002/0471142727.mb1208s36.

1848 Peters, J.M., Mooney, R.A., Grass, J.A., Jessen, E.D., Tran, F., and Landick, R. 2012. Rho and
1849 NusG suppress pervasive antisense transcription in Escherichia coli. *Genes Dev* **26**: 2621-2633.
1850 doi: 10.1101/gad.196741.112.

1851 Quinlan, A.R., and Hall, I.M. 2010. BEDTools: a flexible suite of utilities for comparing genomic
1852 features. *Bioinformatics* **26**: 841-842. doi: 10.1093/bioinformatics/btq033.

1853 Rangarajan, A.A., and Schnetz, K. 2018. Interference of transcription across H-NS binding sites
1854 and repression by H-NS. *Mol Microbiol* **108**: 226-239. doi: 10.1111/mmi.13926.

1855 Riccardi, E., van Mastbergen, E.C., Navarre, W.W., and Vreede, J. 2019. Predicting the
1856 mechanism and rate of H-NS binding to AT-rich DNA. *PLoS Comput Biol* **15**: e1006845. doi:
1857 10.1371/journal.pcbi.1006845.

1858 Rousseeuw, P.J., and Croux, C. 1993. Alternatives to the Median Absolute Deviation. *Journal of*
1859 *the American Statistical Association* **88**: 1273-1283. doi: 10.1080/01621459.1993.10476408.

1860 Sankar, T.S., Neelakanta, G., Sangal, V., Plum, G., Achtman, M., and Schnetz, K. 2009. Fate of
1861 the H-NS-repressed bgl operon in evolution of Escherichia coli. *PLoS Genet.* **5**: e1000405. doi:
1862 10.1371/journal.pgen.1000405.

1863 Santos-Zavaleta, A., Salgado, H., Gama-Castro, S., Sanchez-Perez, M., Gomez-Romero, L.,
1864 Ledezma-Tejeida, D., Garcia-Sotelo, J.S., Alquicira-Hernandez, K., Muniz-Rascado, L.J.,
1865 Pena-Loredo, P.*, et al.* 2019. RegulonDB v 10.5: tackling challenges to unify classic and high
1866 throughput knowledge of gene regulation in E. coli K-12. *Nucleic Acids Res* **47**: D212-D220.
1867 doi: 10.1093/nar/gky1077.

1868 Saxena, S., and Gowrishankar, J. 2011. Modulation of Rho-Dependent Transcription Termination
1869 in *Escherichia coli* by the H-NS Family of Proteins. *J. Bacteriol.* **193**: 3832. doi:
1870 10.1128/JB.00220-11.

1871 Schnetz, K. 1995. Silencing of the *Escherichia coli bgl* promoter by flanking sequence elements.
1872 *EMBO J.* **14**: 2545-2550. doi: 10.1002/j.1460-2075.1995tb07252.x.

1873 Shahul Hameed, U.F., Liao, C., Radhakrishnan, A.K., Huser, F., Aljedani, S.S., Zhao, X., Momin,
1874 A.A., Melo, F.A., Guo, X., Brooks, C.*, et al.* 2019. H-NS uses an autoinhibitory
1875 conformational switch for environment-controlled gene silencing. *Nucleic Acids Res* **47**: 2666-
1876 2680. doi: 10.1093/nar/gky1299.

1877 Shen, B.A., and Landick, R. 2019. Transcription of Bacterial Chromatin. *J. Mol. Biol.* doi:
1878 10.1016/j.jmb.2019.05.041.

1879 Singh, S.S., Singh, N., Bonocora, R.P., Fitzgerald, D.M., Wade, J.T., and Grainger, D.C. 2014.
1880 Widespread suppression of intragenic transcription initiation by H-NS. *Genes Dev* **28**: 214-
1881 219. doi: 10.1101/gad.234336.113.

1882 Sonnenfield, J.M., Burns, C.M., Higgins, C.F., and Hinton, J.C. 2001. The nucleoid-associated
1883 protein StpA binds curved DNA, has a greater DNA binding affinity than H-NS and is present
1884 in significant levels in hns mutants. *Biochimie* **83**: 243-249. doi: 10.1016/s0300-
1885 9084(01)01232-9.

1886 Srinivasan, R., Chandraprakash, D., Krishnamurthi, R., Singh, P., Scolari, V.F., Krishna, S., and
1887 Seshasayee, A.S. 2013. Genomic analysis reveals epistatic silencing of "expensive" genes in
1888 Escherichia coli K-12. *Mol Biosyst* **9**: 2021-2033. doi: 10.1039/c3mb70035f.

1889 Stoebel, D.M., Free, A., and Dorman, C.J. 2008. Anti-silencing: overcoming H-NS-mediated
1890 repression of transcription in Gram-negative enteric bacteria. **154**: 2533-2545. doi:
1891 https://doi.org/10.1099/mic.0.2008/020693-0.

1892 Talbert, P.B., Meers, M.P., and Henikoff, S. 2019. Old cogs, new tricks: the evolution of gene
1893 expression in a chromatin context. *Nat. Rev. Genet.* **20**: 283-297. doi: 10.1038/s41576-019-
1894 0105-7.

1895 Thomason, M.K., Bischler, T., Eisenbart, S.K., Forstner, K.U., Zhang, A., Herbig, A., Nieselt, K.,
1896 Sharma, C.M., and Storz, G. 2015. Global transcriptional start site mapping using differential
1897 RNA sequencing reveals novel antisense RNAs in Escherichia coli. *J Bacteriol* **197**: 18-28.
1898 doi: 10.1128/JB.02096-14.

1899 Tupper, A.E., Owen-Hughes, T.A., Ussery, D.W., Santos, D.S., Ferguson, D.J.P., Sidebotham,
1900 J.M., Hinton, J.C., and Higgins, C.F. 1994. The chromatin-associated protein H-NS alters DNA
1901 topology *in vitro*. *EMBO J* **13**: 258-268. doi: 10.1002/j.1460-2075.1994.tb06256.xs.

1902 Ueda, T., Takahashi, H., Uyar, E., Ishikawa, S., Ogasawara, N., and Oshima, T. 2013. Functions
1903 of the Hha and YdgT proteins in transcriptional silencing by the nucleoid proteins, H-NS and
1904 StpA, in Escherichia coli. *DNA Res.* **20**: 263-271. doi: 10.1093/dnares/dst008.

1905 Ulissi, U., Fabbretti, A., Sette, M., Giuliodori, A.M., and Spurio, R. 2014. Time-resolved
1906 assembly of a nucleoprotein complex between Shigella flexneri virF promoter and its
1907 transcriptional repressor H-NS. *Nucleic Acids Res* **42**: 13039-13050. doi: 10.1093/nar/gku1052.

1908 Uyar, E., Kurokawa, K., Yoshimura, M., Ishikawa, S., Ogasawara, N., and Oshima, T. 2009.
1909 Differential binding profiles of StpA in wild-type and h-ns mutant cells: a comparative analysis
1910 of cooperative partners by chromatin immunoprecipitation-microarray analysis. *J Bacteriol*
1911 **191**: 2388-2391. doi: 10.1128/JB.01594-08.

1912 van der Valk, R.A., Qin, L., Moolenaar, G.F., and Dame, R.T. (2018). Quantitative Determination
1913 of DNA Bridging Efficiency of Chromatin Proteins. In Bacterial Chromatin: Methods in
1914 Molecular Biology, R.T. Dame, ed. (New York, NY: Humana Press).

1915 van der Valk, R.A., Vreede, J., Qin, L., Moolenaar, G.F., Hofmann, A., Goosen, N., and Dame,
1916 R.T. 2017. Mechanism of environmentally driven conformational changes that modulate H-NS
1917 DNA-bridging activity. *eLife* **6**: e27369. doi: 10.7554/eLife.27369.

1918 Vora, T., Hottes, A.K., and Tavazoie, S. 2009. Protein occupancy landscape of a bacterial
1919 genome. *Mol Cell* **35**: 247-253. doi: 10.1016/j.molcel.2009.06.035.

1920 Wang, H., Yehoshua, S., Ali, S.S., Navarre, W.W., and Milstein, J.N. 2014. A biomechanical
1921 mechanism for initiating DNA packaging. *Nucleic Acids Res* **42**: 11921-11927. doi:
1922 10.1093/nar/gku896.

1923 Will, W.R., Bale, D.H., Reid, P.J., Libby, S.J., and Fang, F.C. 2015. Evolutionary expansion of a
1924 regulatory network by counter-silencing. *Nat Commun* **5**: 5270. doi: 10.1038/ncomms6270.

1925 Will, W.R., Whitham, P.J., Reid, P.J., and Fang, F.C. 2018. Modulation of H-NS transcriptional
1926 silencing by magnesium. *Nucleic Acids Res* **46**: 5717-5725. doi: 10.1093/nar/gky387.

1927 Wilson, K. 2001. Preparation of Genomic DNA from Bacteria. *Curr Protoc Mol Biol* **56**: 2.4.1-
1928 2.4.5. doi: 10.1002/0471142727.mb0204s56.

1929 Yamada, H., Yoshida, T., Tanaka, K., Sasakawa, C., and Mizuno, T. 1991. Molecular analysis of
1930 the Escherichia coli has gene encoding a DNA-binding protein, which preferentially recognizes
1931 curved DNA sequences. . *Mol. Gen. Genet.* **230**: 332-336. doi: 10.1007/BF00290685.

1932 Zhou, T., Yang, L., Lu, Y., Dror, I., Dantas Machado, A.C., Ghane, T., Di Felice, R., and Rohs, R.
1933 2013. DNAshape: a method for the high-throughput prediction of DNA structural features on a
1934 genomic scale. *Nucleic Acids Res* **41**: W56-62. doi: 10.1093/nar/gkt437.

1935